An aerodynamic analysis of Hyperloop breach using a scaled physical test setup and background oriented schlieren

by

Mark Miedema

to obtain the degree of Master of Science
in Aerospace Engineering
at the Delft University of Technology,
to be defended publicly on Thursday August 26, 2021 at 13:30 PM.

Student number: 4162862

Thesis committee:

Dr. ir. B. W. van Oudheusden,	TU Delft, chairman
Dr. ir. F. F. J. Schrijer,	TU Delft, supervisor
Dr. ir. M. F. M. Hoogreef,	TU Delft, external examiner
ir. B. M. Neelis,	Tata Steel, external

TU Delft

Summary

Hyperloop, an innovative transport concept in which transport pods move through evacuated tubes, has had extensive research done to further its feasibility. Hyperloop breach, a failure scenario in which the tube integrity is compromised and air flows into the tube, is however a subject with very little research. This research aims to provide an understanding of the Hyperloop tube breach failure scenario. The method of doing this is analysing the aerodynamic responses of Hyperloop tube breach, including a stationary Hyperloop transport pod, by using a scaled physical test setup and background oriented schlieren.

A test setup is designed and constructed to perform scaled physical tests that emulate Hyperloop breach conditions. A transparent tube material is used to allow the use of background oriented schlieren measurement technique. Measurements are taken using a high speed camera focused on a background pattern placed in the test setup. Several tests are performed. The first test is a low frames per second test in which the whole pressure range a closed tube, to an opened breach hole tube, to ambient pressure is registered. The second test is a high frames per second test to visualise initial breach hole shockwave effects. The third test is a Hyperloop pod test in which a scaled Hyperloop pod is placed inside the tube during the experiment. Each test is performed for two different breach hole sizes to determine what effects the breach hole size has on Hyperloop breach.

The test results were documented, stored and processed by having all measurements adjusted to the same timeline of the experiment. The test results were analysed using a Snell's law ray tracing model, in which the path of light rays from a background pattern, through the tube and to the camera lens were simulated. By running this model for different pressure inside the tube, thereby simulating the changing pressures and changing refractive indices during the tests, data is obtained that correlates light ray displacements to pressure values inside the tube.

The first test showed many pressure jumps across the test time. This is most likely attributed to error sources. Error sources cause a pixel displacement that can be higher than the smallest displacement measured in the test, thus the conversion from pixel displacement to its associated pressure is affected by these error sources. Furthermore, several images did not have the lowest displacement position in the center, which is the position where it is expected. Since the Snell's law model expects displacements to increase the further the position is away from the center of the image, any images that do not adhere to this condition will correspond to pressure values that are different compared to images that do adhere to the condition. The larger breach hole reaches ambient pressure faster than the smaller breach hole due to a higher mass flow rate of air entering the tube. By using a second degree fit of the converted pressure data a graph can be made that corresponds well to pressure readings from the pressure meters of the performed test.

From the second test the presence of shockwaves could not be confirmed from the test results. A correlation operation was performed between subsequent image frames in an attempt to find pixel displacements indicating shockwave effects, however no clear pixel displacement indicating such effects were obtained from this correlation.

For the third test the presence of shockwaves could not be confirmed from the test results. While displacements around the Hyperloop pod could be investigated by applying a masking function, no

shockwaves were detected. Since the presence of a shockwave could not be confirmed, the interactions between Hyperloop pod and shockwave could not be investigated from image correlation.

From the experiments performed the use of background oriented schlieren for Hyperloop breach research seems feasible, however the results are sensitive to error sources. Furthermore, converted pressure values require a second degree fit while also applying a correction, shifting the graph downward to account for the minimal measurable displacement. While error sources in the measurement data prevent conclusions being drawn for full scale Hyperloop development and shockwave development as a result of Hyperloop breach, this research forms basis for future Hyperloop breach research.

Acknowledgements

I would like to acknowledge everyone that has helped me in completing my academic journey. I would like to thank Ferdinand for his guidance and help during this thesis. Ferdinand has helped me with academic knowledge while also being a source of trust and feedback, especially in a society restricted by COVID-19. The tools and ideas provided by him for the test setup were of great use.

I would like to thank the High Speed Lab staff for helping me during the experiments and the support given during the construction of the test setup. Frits provided great support in preparing the parts of the test setup. Peter provided guidance and support during the construction of the test setup. I would also like to thank Nico for ensuring the software and hardware used in this project was working properly.

I would also like to thank Yorrick for providing feedback during this project. The countless calls and discussions to ensure the Hyperloop breach project proved successful have greatly helped my drive and motivation.

My thanks go to Bas Neelis and the entire Hyperloop development team at Tata Steel. Without the opportunity provided to me by Tata Steel to experience the Hyperloop development, this project would not have been possible. Bas provided guidance not only for a student and an engineer, but also as a person, for which I thank him greatly.

Finally I would like to thank my friends and family for being there for me during a society restricted by COVID-19. Their encouragement and support for me to keep going has not gone unnoticed and I thank them for always believing in me.
Mark Miedema,
Beverwijk, August 2021

Nomenclature

Latin

A	Cross section area
a	Speed of sound
C_d	Coefficient of discharge
C_p	Specific heat for constant pressure
c_s	Shockwave speed
C_v	Specific heat for constant volume
D	Tube diameter
d	Orifice diameter
d_t	Total displacement
d_x	Displacement in x-direction
d_y	Displacement in y-direction
dF	Force difference for shockwave calculations
f	Focal length of the lens
h	Enthalpy
K	Gladstone Dale constant
Kn	Knudsen number
L	Characteristic length
L_i	Leak rate at step i
M	Mach number
m	Mass
n	Refractive index
p	Pressure
p_t	Total pressure
R	Gas constant
r	Tube radius
R_i	Specific refraction of air component i

Re	Reynolds number
T	Temperature
t	Time
u	Flow speed in longitudinal direction
V	Flow speed through the channel
V_c	Chamber volume
x	Position of station point on the tube
x_{CO_2}	CO_2 volume percentage
Z_a	Distance between lens and tube medium
Z_d	Distance between background plane and tube medium

Greek

α	Emperical coefficient fort Weibull's equation
Δy	Distance on the image plane
ϵ	Expansibility factor of the medium
ϵ_y	Angle after passing through tube medium
γ	Specific heat ratio
λ	Wavelength
λ_{fp}	Mean free path
μ	Dynamic viscosity
ρ	Density
σ	Standard deviation
θ_1	Incidence angle with the normal in medium 1
θ_2	Refraction angle with the normal in medium 2
μ_m	Mean of the data points
σ^2	Variance

Abbreviations

BOS	Background Oriented Schlieren
CFD	Computational Fluid Dynamics

fps Frames per Second

HSL High Speed Lab

HTFD Hypersonic Test Facility Delft

ITER International Thermonuclear Experimental Reactor

PLA Polyactic Acid

PMMA Polymethyl Methacrylate

PTU Programmable Timing Unit

sCMOS Scientific Complementary Metal–Oxide–Semiconductor

STL Stereolithography

Contents

List of Figures

List of Tables

1 Introduction to Hyperloop Breach

1.1 What is Hyperloop?

In a world where mobility and connectivity between people is ever increasing, meeting demands for transportation is proving to be a burden on the infrastructure, the economy and the environment. With natural resources dwindling an answer has to be found to a future proof transportation solution. One such proposed solution is the Hyperloop: in the Hyperloop transportation pods are launched through a vacuum tube at high rates of speed towards the requested destination, of which a concept drawing is shown in figure 1[17].

Figure 1: Concept drawing of the Hyperloop system [17]

This solution, sometimes viewed by critics as overambitious and even crazy, aims to be the CO_2-neutral answer to transport passengers and cargo at cruise speeds of over 700 km/h, rivaling aircraft as a transportation source.

The Hyperloop concept in itself is not a complete novelty: the use of vacuum and air pressure for propulsion dates back to the 19^{th} century. Proposed by G. Medhurst[1] was a brick tunnel in which rails would be installed. A vehicle able to carry passengers would ride on the rails. A piston is mounted at the end of this vehicle with a size that nearly fits the tunnel. From this the vehicle would be propelled while a vacuum remained in front of the vehicle, while atmospheric air was blown behind it, leading to very high speeds. The concept was never successfully realised due to the fact that engine technology used for the blowing machine was not very advanced. Another issue was that in order to keep the vacuum in front of the vehicle, the rear side of the vehicle had to very tightly fit the tube, which proved difficult. Furthermore, the idea of traveling through closed of tubes was unpleasant to people back in 1810 [1]. Modern day innovations such as screens and climate control can however make the trips more pleasant. Even though improvements were made to engineering throughout the years and test installations were made, the plan never truly came into fruition. Nevertheless, the

concept has peaked interest of engineers throughout history.

The Hyperloop concept was brought back to life by Elon Musk in 2013, when he published the "Hyperloop Alpha" paper[22]. In the paper a solution is suggested that rivals flying or driving as a transporting medium. Elon Musk deems current high speed rail solutions too expensive per mile and too slow to compete with current transporting solutions, thus a new solution should be found. He sets the following requirements [22]:

- Safer
- Faster
- Lower cost
- More convenient
- Immune to weather
- Sustainably self-powering
- Resistant to earthquakes
- Not disruptive to those along the route

Elon Musk suggests the solution to this is the Hyperloop: inspired by pneumatic tube systems used for physical mail as employed in the 19^{th} and 20^{th} century, Hyperloop is a tube systems in which pods are used to transport cargo or people at high speeds in a near-vacuum. This tube has to contain a very low pressure however due to the incredible drag a tube filled with atmospheric pressure air would create. Furthermore Elon Musk deems the Kantrowitz limit a critical factor: the maximum speed limit as a function of blockage ratio of pod to tube area. Musk describes it as the capsule behaving like a syringe if the bypass ratio is to low [22]. In this paper Musk envisions that the capsule will travel at 1220 km/h, which equates to a Mach number of 0.91 [22]. The capsule would feature a compressor near the front which bypasses flow to the back of the capsule and makes sure the flow is not choked.

Big obstacles for the Hyperloop are the amount of steel required and the construction cost of the vacuum tube. For a purely steel tube with an inside diameter of 3.6 meters and a wall thickness of 20 millimeters a cost of 1.38 million euro per kilometer using Chinese prices of common steel is estimated(using the Chinese Yuan to EURO exchange rate of 24-05-19). This is for a simple cylindrical tube and without taking into account joining techniques. Furthermore, if the full scale Hyperloop would be realized the amount of steel required would be enormous[3]. This would not only take up a significant portion of the total steel production, it would also create a great amount of CO_2 emission. Another option is using both concrete and steel, where a 1-2 millimeters steel layer mainly serves as an air proof layer. This would increase the tube thickness but decrease costs due to the use of concrete [35].

Ever since the Hyperloop Alpha paper was published, Hyperloop development expanded rapidly. Several competitions were held at SpaceX for student and non-student teams to demonstrate the feasibility of their Hyperloop transportation pod design. The main goal of the competition was to reach the maximum possible speed in the test track on the SpaceX site, however teams were also judged

for their business plan, pod design, safety, efficiency, scalability of the design and levitational ability. Delft Hyperloop won the overall first place in the first competition in January 2017[18]. Members of that team would later create Hardt Hyperloop, which aims at making Hyperloop a reality in Europe.

In 2017 Tata Steel Europe joined the European Hyperloop Program by partnering with Hardt Hyperloop and started with several projects to contribute to a more feasible tube design for the Hyperloop. The focus of Tata Steel Europe lies in creating smart tube concepts to reduce the amount of material required for the tube. A reason for this is that it would reduce the load on the total steel production while also reducing CO_2 emissions. One of these smart tube projects was the first Hypertube Student Team, which took place from August to December 2018. Two concepts, a polyhedral and a segmented tube-in-tube design, were investigated using finite element modelling, joining method analysis and scaled physical testing[3]. With Hardt moving forward and planning on building a scaled test track(an estimated diameter of around 1.5 meter and 3 kilometer in length), Tata Steel wants to supply a segment of the tube using one of the developed smart concepts. To do this, a second team will investigate selected tube concepts further by means of finite element modelling and physical testing, after which a final tube concept is selected.

One of the biggest obstacles of Hyperloop might not be the structural or aerodynamic analysis of the pod, but the safety of the Hyperloop system. Currently there is a huge gap in safety requirements and standardization. A reason for this is that current legislation is applicable to either (high-speed)trains or aircraft, however Hyperloop has not been clearly defined as either[16]. Furthermore, safety testing of the Hyperloop has not been performed extensively. Safety regulation predictions are mostly based on theories, ideas and theoretical calculations: it is viewed as something either out of scope or something to be done in the future[16]. Safety regulations however also play a big part in the design process of both the Hyperloop tube and the Hyperloop transport pod. In order to define boundary conditions on structural requirements, failure scenarios have to be analyzed. One such failure scenario is breach: a situation in which air will rush into the tube due to the overpressure caused by a hole in the tube. How the Hyperloop breach scenario is best investigated is a problem that must tackled in this research and is therefor the main goal. Furthermore, this research aims to improve knowledge of the safety framework of the Hyperloop system using a scaled physical test setup that emulates a Hyperloop breach.

Hyperloop breach itself is a very broad topic, which can be investigated using numerical models, aerodynamic analysis tests, structural analysis tests and Hyperloop pod analysis on both the full scale as well as small tests scales. For this research the scope will be limited to a scaled physical test setup, investigating the aerodynamic analysis including the Hyperloop pod, supported by numerical models and correlation software. Limiting the size by performing a scaled physical test setup allows for a controlled testing environment at university facilities. This introduces scaling factors that have to be accounted for with respect to drawing conclusions towards full scale Hyperloop operations, which will be addressed in chapter 2.

By using a measurement technique that allows for analyzing the aerodynamic response inside the tube, the flow conditions Hyperloop pods will encounter can be investigated. Background oriented schlieren, a measurement technique that uses correlation of images to determine displacement in a test section, will be used in this research and this choice will be explained in detail in chapter 4.

1.2 Research objective

With the purpose of the research outlined in the previous section, the research objective can be defined. As was described, the subject of Hyperloop breach itself is broad, thus the limitations of the research are outlined as well.

The research objective is to analyse the aerodynamic responses of Hyperloop tube breach, including a stationary Hyperloop pod, by using a scaled physical test setup and background oriented schlieren.

This research also aims to determine how well scaled physical test results relate to the full scale Hyperloop and how effective background oriented schlieren is for Hyperloop breach testing. This way recommendations can be given on future research on the subject of Hyperloop breach.

1.3 Research questions

To properly define the research that is to be carried out, a division is made into several main research question which are subdivided into sub-questions. The following research questions are identified, in which main questions and sub-questions are identified:

1. What theory is required for analysing a Hyperloop tube breach?
    - Which models are available or can be created, such that predictions can be made for a physical test and test results can be analyzed?
    - Which aerodynamic phenomena should be investigated that could occur during Hyperloop tube breach?
    - How feasible is the use of background oriented schlieren for Hyperloop breach testing?
2. What are the requirements for performing a Hyperloop tube breach test?
    - What kind of equipment is required to perform and measure a Hyperloop tube breach test?
    - What flow conditions are tests performed at?
    - What tube and pod geometry is used during a Hyperloop tube breach test?
3. What conclusions can be drawn from the physical test with respect to the Hyperloop breach failure scenario?
    - Do the results from the physical test support the need for further research into the Hyperloop breach failure scenario?
    - What conclusions can be drawn for the full scale Hyperloop tube from the small scale test?

1.4 Overview

In chapter 2 the literature review of Hyperloop breach is provided. The expected flow topology in Hyperloop breach is explained using Hyperloop pod shape and breach hole analysis. Furthermore assumptions for quasi-1D flow are made and its relevance to Hyperloop breach research is explained.

Important considerations for Hyperloop breach such as the Kantrowitz limit, low density considerations and shockwave effects are discussed in this chapter as well. The testing equipment used during experiments is described in chapter 3. For this research, a physical experiment is performed to provide answers to the research questions. A physical experiment is chosen to study the effects of Hyperloop breach in a test facility while providing a validation for numerical model results. Background on the testing method can be found in chapter 4. The working principle of background oriented schlieren is explained as well as the physical and digital requirement of performing an experiment using this measurement technique. The model used to analyse test results is discussed in chapter 5. The model is based on Snell's law and all relevant parameters used in the model are described. The choices and assumptions made are described such that its applicability to the performed physical test is clarified. Furthermore, shockwave and mass flow rate predictions for the physical test are made in this chapter. In chapter 6 the test setups are described, including the relevance and the difference between each test setup. First the background oriented schlieren feasibility test is described, in which the measurement method is tested to confirm its feasibility. Afterwards, the three different tests are described in detail as well as why the choice was made to perform these specific tests. The results of the tests are discussed in chapter 7. The physical test results are analyzed using the Snell's law model, observations and tests predictions. The results are plotted and error values and measurement data operations are described. Lastly the conclusions are present in chapter 8 and the discussion and recommendations are discussed in chapter 9.

2 Aerodynamic Concepts of Hyperloop

Many factors determine the flow behaviour in Hyperloop, such as: tube diameter, tube design, inside pressure and ambient conditions. When the airflow through a tube is started due to Hyperloop breach, more factors become involved, such as: breach hole size, hole surface smoothness and breach hole location. When a pod travelling through the tube is also considered, another set of factors is involved, such as: pod shape, pod blockage ratio and pod position in the tube. In this chapter a review of knowledge on Hyperloop and Hyperloop breach will be presented.

2.1 Airflow through a Hyperloop tube

Before going into further detail, it is important to define what this research views as Hyperloop breach with respect to methods to analyze it. Hyperloop itself is viewed as an enclosed tube in which a Hyperloop transport tube is present. In Hyperloop, a pressure of approximately 1 *mbar* exists inside the Hyperloop tube. If a breach of the Hyperloop tube occurs in which the tube integrity is compromised, outside ambient air will start flowing into the tube. Since many failure scenarios of the tube exist, for this research it is viewed as a hole in the wall of the tube. The air flowing into the tube has several effects. Firstly, the pressure inside the tube will gradually rise. Secondly, the air flowing into the tube will propagate throughout the tube and interact with Hyperloop transport pods. While in a low pressure environment, the Hyperloop pod will still have drag. Drag is be composed of viscous drag and pressure drag. Viscous drag is influenced by the shape and length of the Hyperloop pod, thus an efficient Hyperloop pod design is required for minimal drag. During a Hyperloop breach air flows into the tube and the pressure increases, which also causes the pressure drag to increase. While for traditional long transport vehicles the pressure drag is the dominant factor, for Hyperloop pods this is different: since the Hyperloop pod is inside of a tube, the area the Hyperloop pod takes up inside the tube disrupts the flow of air, which is called the blockage ratio. Due to this effect, the pressure drag will be the dominant factor for Hyperloop pods. This effect will be explained in more detail in section 2.3 by introducing the Kantrowitz limit.

If a sufficient pressure difference exists at the breach hole shockwaves can occur. Shockwave can propagate through the tube and eventually interact with the Hyperloop pod. The shockwaves can destabilize the pod from its position in the tube. Furthermore, for non lifting surfaces such as the Hyperloop pod, shockwaves are undesired due to the increase in wave drag it causes[5].

To obtain a better understanding of the interaction of air flowing through the Hyperloop tube and the Hyperloop pod, the aerodynamic analysis of a Hyperloop pod by of the MIT Hyperloop team will be presented. The designed MIT Hyperloop pod is 2.4 m long and the Mach number distribution over the pod for upstream Mach number of 0.675, corresponding to a Reynolds number of $3.16e^5$ and made using a $\kappa - \omega$ SST turbulence model, is shown in figure 2[25].

It can be observed that the flow accelerates over the pod up to 25% of the length of the pod, at which point the Mach number reaches a value greater than 1. A small shockwave develops at that location as well, while the stagnation point is at the leading edge of the pod as expected. The flow development is however determined by the pod shape, thus while figure 2 shows typical behaviour of flow development of a Hyperloop pod, the exact shape and size is different for the Hyperloop pod used in this research, as will be explained in further detail in section 3.2.

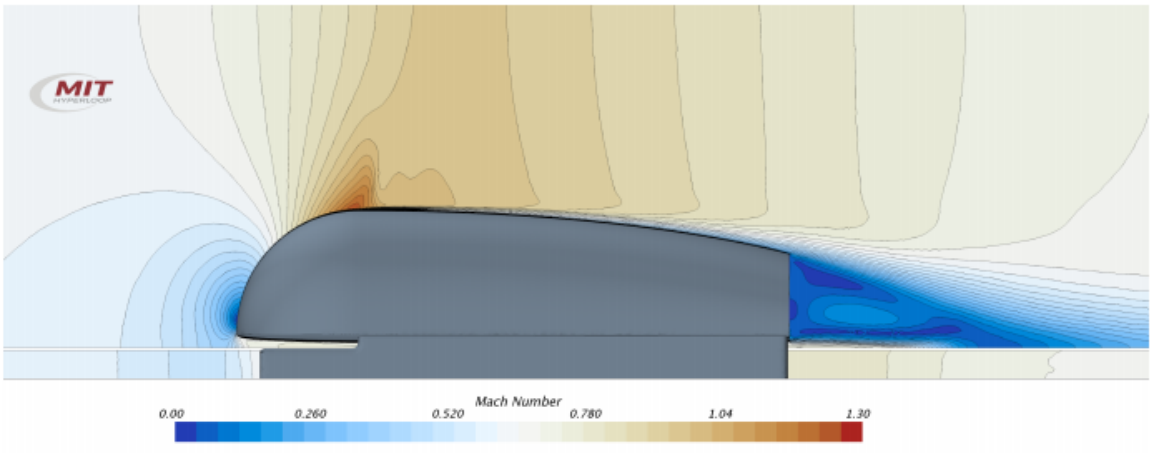

Figure 2: Mach number distribution over the MIT Hyperloop pod for a freestream Mach number of 0.675, corresponding to a Reynolds number of $3.04e^5$ [25]

When comparing figure 2 to the principles of flow through a channel, many similarities can be identified. The air flows through the tube at a speed determined by the pressure levels and stays at that speed until either the pressure changes or a change in area occurs. Furthermore, the flow accelerates untill the smallest area in the channel, the throat, is reached, possibly supersonic if the pressure levels allow for this. When flow parameters are assumed to be only dependent on the longitudinal direction and area changes in the section are gradual, the flow can be assumed as quasi-one-dimensional[5].

To obtain a better insight of flow through a Hyperloop tube in which a Hyperloop pod is present, the fundamentals of flow through a channel will be stated and investigated. For flow through a channel the mass flow rate remains constant throughout due to conservation of mass and this equation is called the continuity equation:

$$\dot{m} = \rho A V = constant \tag{1}$$

In this equation $\dot{m}$ is the mass flow rate, ρ is the density, A is the cross section area and V is the speed. If an ideal compressible gas is considered, the mass flow rate, which is at a maximum for a Mach number of one at choked flow conditions, can be defined as :

$$\dot{m} = \frac{A p_t}{\sqrt{T_t}} \sqrt{\frac{\gamma}{R}} \left(\frac{\gamma + 1}{2}\right)^{-\frac{\gamma+1}{2(\gamma-1)}} \tag{2}$$

In this equation p_t is the total pressure, R the gas constant and T_t the total temperature [11]. When air flows through a converging duct at a Mach number of less than one, the velocity of air increases. For supersonic flow this reverses as shown in figure 3[5]. This is explained by compressibility effects: at Mach numbers higher than one, an increase in air velocity is accompanied by a greater decrease in density. To still achieve conservation of mass, when the area increases, the density decreases and the

velocity thus has to increase as well. [26]. To derive this relation between area and velocity, the mass equation for isentropic flow,

$$\frac{dp}{\rho} + \frac{1}{2}\frac{dV^2}{V^2} + \frac{dA}{A} = 0 \tag{3}$$

is combined with the momentum equation for isentropic flow,

$$\frac{dp}{\rho V 2} + \frac{1}{2}\frac{dV^2}{V^2} = 0 \tag{4}$$

and using that for isentropic conditions $\frac{\delta p}{\delta \rho} = a^2$, the following equation is obtained for compressible isentropic conditions [5]:

$$\frac{dA}{A} = (M^2 - 1)\frac{dV}{V} \tag{5}$$

When considering the situation in which a pod is placed inside the Hyperloop tube, a cross sectional area change will occur. These relations will therefor be applicable to Hyperloop breach research as well.

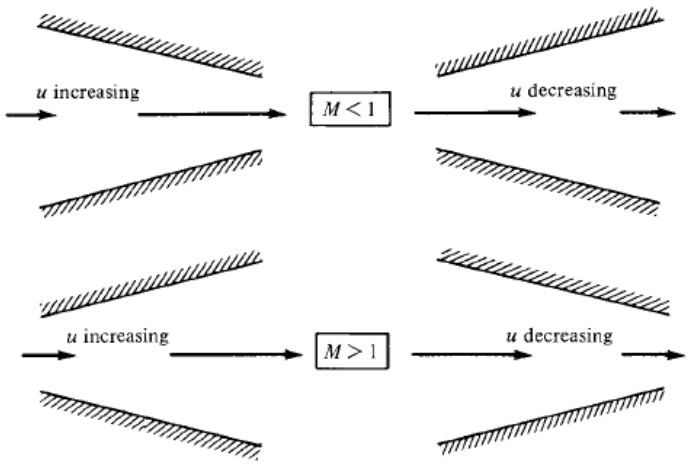

Figure 3: Area rule visualization for converging and diverging nozzles and subsonic and supersonic speeds. u is the flow speed in longitudinal direction [5]

In order to use this knowledge when investigating flow through a channel, the relations between throat area and Mach number have to be defined. Several equations will be stated that are required to finally derive the relation between throat area and Mach number in the channel. To start, the well known equation of state is shown in the following equation:

$$p = \rho R T \tag{6}$$

In equation 6, p is the pressure, R the gas constant and T the temperature. The energy equation, which states that no energy is added or lost for adiabatic conditions, is stated as:

$$C_pT + \frac{V^2}{2} = C_pT_t = constant \tag{7}$$

In equation 7, C_p is the specific heat for constant pressure and the t subscript denotes total conditions(flow at rest).

For flow in isentropic conditions, the following equation holds for each station along the length of the channel:

$$\frac{T}{p^{(\frac{\gamma-1}{\gamma})}} = constant \tag{8}$$

In equation 8 γ is the specific heat for constant pressure divided by the specific heat for constant volume (C_p/C_v).

From this the well know equation that relates temperature at each station is derived, based on the Mach number at that station [26]:

$$\frac{T_1}{T_2} = \frac{1 + \frac{\gamma-1}{2}{M_2}^2}{1 + \frac{\gamma-1}{2}{M_1}^2} \tag{9}$$

Finally, by using equation 1, a relation between area ratio and Mach number is found in the following equation [26]:

$$\frac{A_1}{A_2} = \frac{M_2}{M_1}\left(\frac{1 + \frac{\gamma-1}{2}{M_2}^2}{1 + \frac{\gamma-1}{2}{M_1}^2}\right)^{-\frac{\gamma+1}{2(\gamma-1)}} \tag{10}$$

When determining conditions at the throat area A^*, equation 10 can be rewritten to the following equation:

$$\frac{A}{A^*} = \frac{1}{M}\left(\frac{1 + \frac{\gamma-1}{2}M^2}{\frac{\gamma+1}{2}}\right)^{\frac{\gamma+1}{2(\gamma-1)}} \tag{11}$$

2.2 Pressure ratios and choked flow

In the previous section the similarities between flow through a channel and flow in a Hyperloop tube including a Hyperloop pod were described and this will be elaborated further in this section. The way air flows through a channel can be related to the pressure ratio across the channel and the geometric properties of the channel. First of all, flow will only start accelerating if the exit pressure p_e is smaller than the inlet pressure p_0, creating a positive pressure gradient. The exit pressure thus determines which speeds can be attained in the wind tunnel at each section. Furthermore, if flow continues accelerating beyond the Mach number of one after the throat of the channel, the location of a normal shock is affected by exit pressure. If the flow expands to a Mach number that is equal to the Mach number at exit M_e than the situation shown in figure 4 is present. Here M_{e6} is the Mach number of the expanded flow that is equal to M_e, with the notation consistent as defined by Anderson[5].

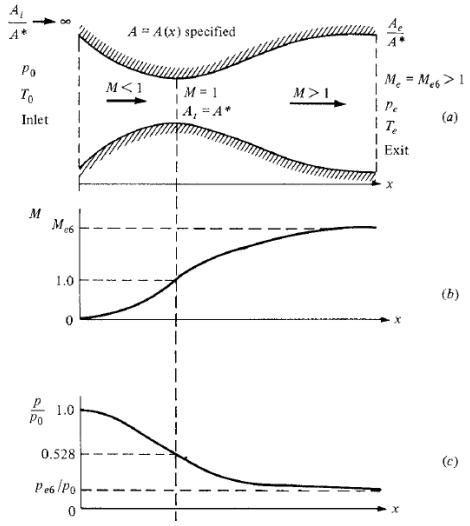

Figure 4: Pressure ratios(c) and Mach number(b) throughout the convergent divergent section for optimal isentropic conditions[5]

If the exit pressure were to increase however, the flow would not be able to expand to a Mach number equal to the exit Mach number. If the exit pressure were to be of such magnitude that a Mach number of one could only just be reached in the throat, the situation notated by 3 is present as shown in figure 5. If the magnitude of the exit pressure were to be even higher, a Mach number of one at the throat cannot be reached anymore.

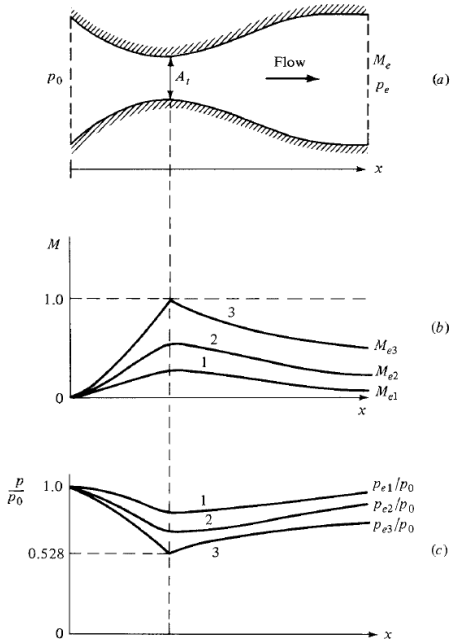

Figure 5: Pressure ratios(c) and Mach number(b) throughout the convergent divergent section for the cases in which the exit pressure is higher than p_{e6}[5]

The observation of pressure at which the flow in the throat has a Mach number of one leads to another conclusion for the mass flow ratio: since the Mach number in the throat cannot increase if the exit pressure is decreased, the mass flow ratio will remain constant for a pressure of p_{e3} and below, as is shown in the variation of exit pressure with mass flow rate in figure 6. If this were to happen, the flow is called choked.

Even though the flow speed upstream of the throat and at the throat itself remain constant when the exit pressure is decreased below p_{e3}, downstream of the throat there is a change in flow speed as shown in figure 7.

However, if the exit pressure p_{e4} is higher than p_{e5}, the flow will not fully expand through the end of the divergent section of the channel. Instead, a normal shock wave will occur inside the divergent section. Its location is determined by the exit pressure: the closer the value of the exit pressure is to p_{e5}, the more down stream the location of the normal shock wave will be.

2.3 Kantrowitz limit and blockage ratio

When a test setup that includes both a Hyperloop tube and a Hyperloop pod is introduced, a new problem arises: the blockage ratio. Since the pod itself will have a cross sectional area inside the tube, the air will have to flow around the pod. To show that this limit becomes relevant for Hyperloop,

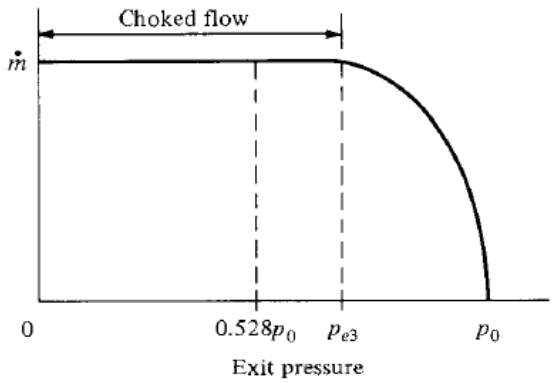

Figure 6: Mass flow as a function of exit pressure p_{e6}[5]

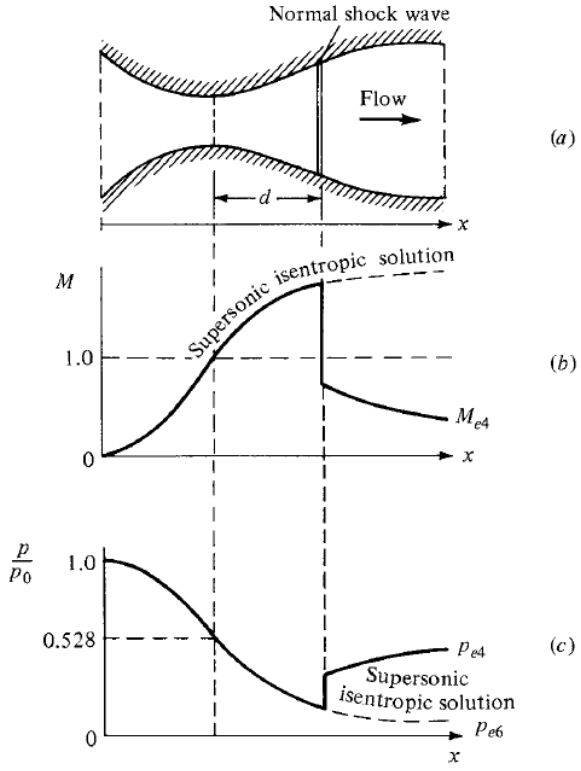

Figure 7: Normal shock wave formation downstream of the throat p_{e6}[5]

again the MIT Hyperloop pod research will be used by comparing Mach number development for different free stream Mach numbers in figures 8 and 9[25].

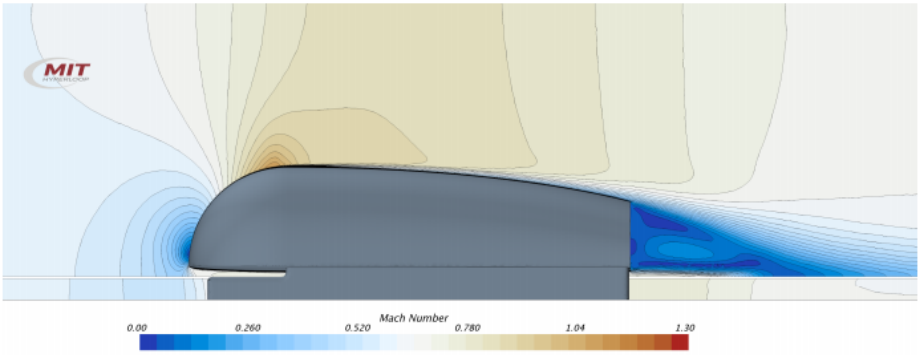

Figure 8: Mach number distribution over the MIT Hyperloop pod for a freestream Mach number of 0.65, corresponding to a Reynolds number of $2.93e^5$ [25]

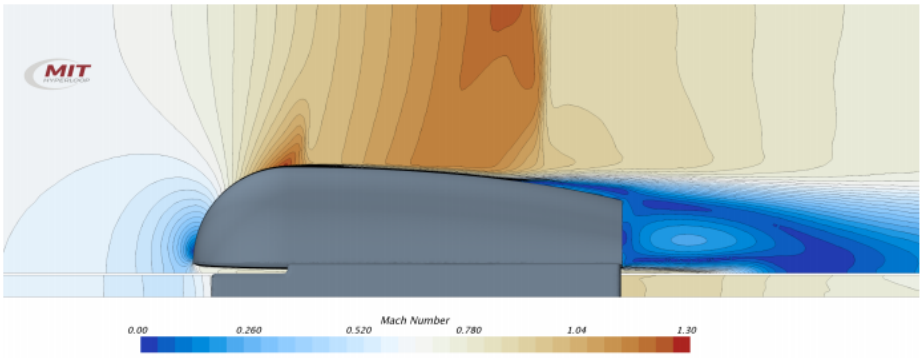

Figure 9: Mach number distribution over the MIT Hyperloop pod for a freestream Mach number of 0.70, corresponding to a Reynolds number of $3.16e^5$ [25]

The difference between both figures is a freestream Mach number of 0.65 for figure 8 and a freestream Mach number of 0.70 for figure 9, however the Mach number line distribution over the pods is very different. Figure 9 has supersonic speeds of the pod with the presence and development of a shockwave and boundary layer separation as a result of this. It appears the flow is choked at this freestream Mach number of 0.70 and the mass flow rate around the pod does not increase any further, instead a pressure build-up occurs in front of the pod shown by the pressure coefficient 1 m above the pod in figure 10[25].

To determine what an acceptable blockage ratio would be, Wong investigated this for drag as a result of blockage ratio shown in figure 11[34].

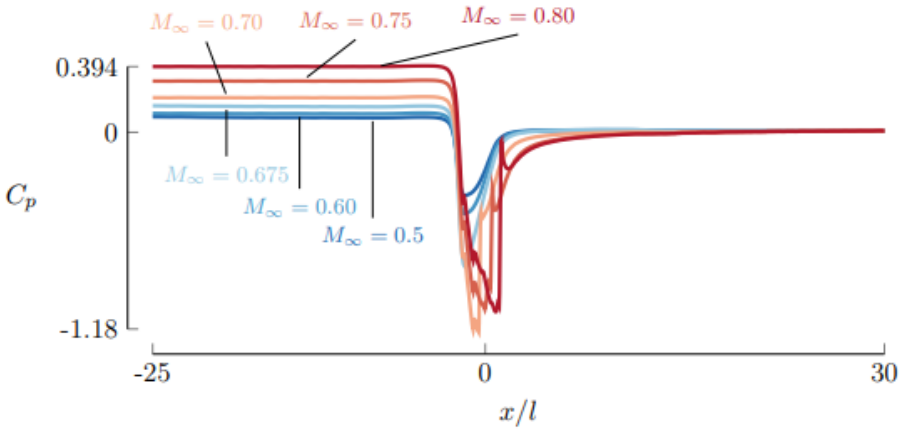

Figure 10: Pressure coefficient at 1 meter above the MIT Hyperloop pod for different freestream Mach numbers [25]

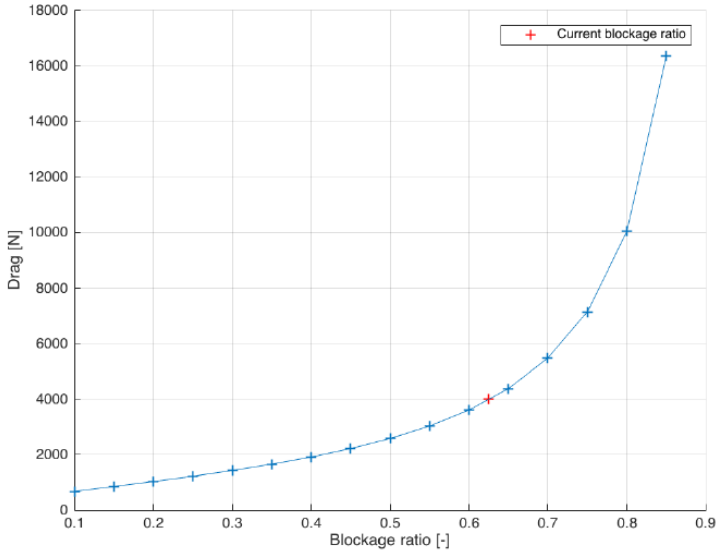

Figure 11: Drag as a result of blockage ratio[34]

The most important factors for the drag are the blockage ratio, pressure in the tube and velocity[34]. Figure 11 shows a quadratic relation between drag and blockage ratio, with 0.625 marked as the blockage ratio of Wong's pod design. Wong also states that a rapid increase in drag is observed when speeds exceed 99.5 $\frac{m}{s}$, which is only half the envisioned cruise speed of the Hyperloop[34].

In order to quantify an acceptable blockage ratio, the Kantrowitz limit is introduced. This relation

is derived as follows: Assuming flow through a channel, the conservation of mass implies the mass flow rate at each station is equal, as was established in section 2.1. Thus for each station,

$$\dot{m} = \frac{Ap_t}{\sqrt{T_t}}\sqrt{\frac{\gamma}{R}}M(1+\frac{\gamma-1}{2}M^2)^{-\frac{\gamma+1}{2(\gamma-1)}} \tag{12}$$

Assuming one of the stations is the throat in which flow has a Mach number of one the relation becomes:

$$\frac{A_1 p_t}{\sqrt{T_t}}\sqrt{\frac{\gamma}{R}}M_1(1+\frac{\gamma-1}{2}{M_1}^2)^{-\frac{\gamma+1}{2(\gamma-1)}} = \frac{A_2 p_t}{\sqrt{T_t}}\sqrt{\frac{\gamma}{R}}(\frac{\gamma+1}{2})^{-\frac{\gamma+1}{2(\gamma-1)}} \tag{13}$$

holds.
Assuming isentropic flow conditions, solving for the area ratio, thus attaining the ratio of bypass area and tube area, the following equation is obtained[20]:

$$\frac{A_{bypass}}{A_{tube}} = (\frac{\gamma-1}{\gamma+1})^{\frac{1}{2}}(\frac{2\gamma}{\gamma+1})^{\frac{1}{\gamma-1}}(1+\frac{2}{\gamma-1}\frac{1}{M^2})^{\frac{1}{2}}(1-\frac{\gamma-1}{2\gamma}\frac{1}{M^2})^{\frac{1}{\gamma-1}} \tag{14}$$

Since the Kantrowitz limit is also dependent on Mach number, local Mach number over the Hyperloop pod could become a limiting factor. Research done at the University of Seoul indicates strong shockwaves occur at 200 $\frac{m}{s}$ for a blockage ratio of 0.36 and at 225 $\frac{m}{s}$ for a blockage ratio of 0.25 [23], thus the combination of Mach number and blockage ratio is important when designing Hyperloop pods and tubes. Furthermore, since the physical test will be scaled down, if a decision is made to increase the Mach number to emulate full scale flow characteristics such as the Reynolds number, the Kantrowitz limit will also be affected.

The choice of blockage ratio thus becomes a trade off and a decision: if the increase in drag due to the Kantrowitz limit being reached is substantial and critical for efficient transport, then either the pod needs to be decreased in cross sectional area or the tube diameter needs to be increased. On the other hand, if the cost of increasing the diameter of the tube becomes significant in not only construction, but also maintaining a vacuum, then the increase in drag due to reaching the Kantrowitz limit is accepted. The same ideology would be applied if the Hyperloop pod cannot decrease in cross sectional area, due to for example passenger height or safety restrictions. Thus, while Wong's 0.625 blockage ratio is used as a reference in this research and experiment, this is not fixed and not a clear best value for Hyperloop transport[34].

2.4 Flow through an orifice

While in the previous section the mass flow rate considerations due to the Hyperloop pod were explained, in this section the focus is given on the breach hole itself. The breach hole in the tube resembles an orifice: a plate with a small hole in it. The mass flow rate through the hole can be measured based on the geometry of the hole. An overview of flow through an orifice is shown in figure 12[29]:

Due to the sudden change in area in the tube, the most narrow point of airflow, called the vena contracta, is expected behind the orifice itself. The reason for this is that the pressure is not equivalent across the physical cross section, and the pressure only becomes equivalent at the vena contracta. While this is influenced by factors such as orifice diameter to tube diameter and pressure

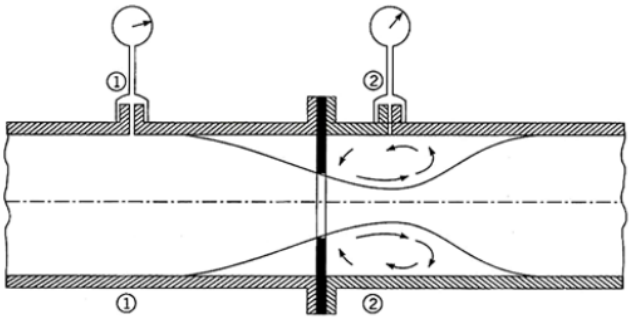

Figure 12: Air flow through an orifice[29]

ratios, this will need to be taken into account when constructing a Hyperloop breach test setup. The mass flow rate through an orifice is shown in the following equation [2]:

$$\dot{m} = \frac{C_d}{\sqrt{1-\beta^4}} \epsilon \frac{\pi}{4} d^2 \sqrt{2\rho\Delta p} \tag{15}$$

In this equation $\dot{m}$ is the mass flow rate through the orifice, C_d is the coefficient of discharge, β is the diameter ratio between orifice and upstream area, ϵ the expansibility factor of the medium, d the orifice diameter and Δp the pressure difference across the orifice. The coefficient of discharge is related to the roughness of the orifice and the Reynolds number through the orifice and is generally approximated by dividing it into a friction term and a contraction term. For Hyperloop breach the coefficient of discharge has a value between 0.6 and 1.0, with the fluctuation of the value caused by the current uncertainty of breach hole quality[2]. By inspecting the surface roughness of the breach hole and using the material properties, an estimate can be made of the coefficient of discharge for the experimental test setup. If the flow through the orifice is choked, equation 15 can be simplified to the following equation [33]:

$$\dot{m} = C_d A \sqrt{\gamma \rho_0 p_0 (\frac{2}{\gamma+1})^{\frac{\gamma+1}{\gamma-1}}} \tag{16}$$

For choked flow, the mass flow rate is dependent on values of the parameters in front of the orifice: since the flow is choked, lowering back pressure will not increase the mass flow rate. In equation 16, p_0 is the pressure in front of the orifice. The mass flow rate through the emulated breach hole is important, since it will determine the properties of the flow throughout the tube. Equation 15 also relates the flow conditions to the size of the breach hole and the pressures difference over the hole. Furthermore, since the shape and structure of the emulated breach hole will determine the coefficient of discharge, construction and quality of the variable hole device will impact the mass flow rate.

2.5 Scaling Factor Parameters

If Hyperloop breach tests are performed at different sizes compared to the full scale Hyperloop operations, scaling factor parameters have to be identified to provide useful conclusions. In this section the

viscous considerations are explained by using the Reynolds number in section 2.5.1, the low density consideration by introducing the Knudsen number in section 2.5.2 and shockwave and Mach number consideration in section 2.5.3.

2.5.1 Reynolds number

This Reynolds number represents the ratio of inertial to viscous forces[32]. The definition of the Reynolds number in the following equation:

$$Re = \frac{\rho V L}{\mu} \tag{17}$$

In equation 17, Re is the Reynolds number, ρ is the density, V is the velocity, L is the characteristic length and μ is the dynamic viscosity.

When flow passes through a circular tube, the characteristic length can be expressed as the diameter of the tube D, shown in the following equation:

$$Re = \frac{\rho V D}{\mu} \tag{18}$$

The Reynolds number determines whether flow in the test section is laminar, turbulent or in the transition phase. For this Hyperloop tube breach research a Reynolds number in the order of $O(10^4) - O(10^5)$ is estimated for 1 *mbar* conditions. While the flow is expected to remain laminar over a large section of the Hyperloop pod, turbulence effects are expected due to transition occurring[34].

Since the test cannot be performed at full scale due to limitations on the size of the testing facility, the test will have to be scaled down. In order to simulate the real conditions, the Reynolds number has to remain constant between both cases. However, since the pod in the test setup will most likely remain stationary, having a correct Reynolds number will be most important near the emulated breach hole, since turbulence effects are expected there due to the sudden abrupt non-gradual change in area. Since the characteristic length is reduced for a scaled down test setup, the Reynolds number will naturally also decrease. To counteract this, several steps can be taken.
The density of the medium can be changed to cope for the reduction in Reynolds number. This can be done by choosing a different medium, such as a high molecular weight gases like nitrogen and sulfur hexafluoride[4]. In transonic conditions, sulfur hexafluoride has shown to increase the Reynolds number by a factor of two for the same Mach number compared to air[4]. Care has to be taken however to safety precautions, since these gases have to stay within the wind tunnel system due to potential safety hazards. Furthermore, due to a change in gas medium, gas constants will change, thus affecting the ratio of the specific heat for constant pressure and the specific heat for constant volume γ. The result will also be a change in the speed of sound, thus when design a test setup all these factors have to be taken into account.

Another option is increasing the speed through the test setup. By increasing the speed, the Reynolds number will increase, thus allowing similar conditions between the scaled and real test setup. The speed in the channel is governed by the downstream pressure and the geometry of channel. The issue with increase in speed is that compressibility effects might become more prevalent.

The Reynolds number itself will determine air flow behaviour around a Hyperloop pod if placed in the tube. The scope of this research however is the shockwave effects and propagation through the Hyperloop tube. The tests with Hyperloop pods will mostly be focused on increase in drag on the pods and shockwave effects on the pods. For this reason, the effect of the Reynolds number due to the pod present is not of interest for this research.

2.5.2 Knudsen number and low-density considerations

Since the Hyperloop will operate under near vacuum conditions, the reduced density will have consequences for determining flow conditions. The proposed 1 *mbar* pressure inside the full scale Hyperloop tube would relate to an earthly altitude of about 48 *km*. When assuming air as a continuum and as a medium in which a transport vehicle is travelling, usual equations for flow conditions and velocity effects hold. However, when density lowers considerably, a medium cannot simply be considered as a continuum. Reason for this is that the average distance between molecules of the medium become significantly large at very low densities. When for-mentioned conditions apply, the applied regime of aerodynamics is low-density flow [7].
A big result of the low-density flow regime is that the no-slip condition near the surface of a body over which air flows no longer holds true. The no-slip conditions indicates that molecules near the surface have a velocity of zero due to friction. This is justified by the fact that the attractive forces between air flow molecules and the surface molecules are much greater than the attractive forces between air flow molecules themselves. In very low density conditions however this does not hold true anymore. Due to the low amount of molecules in the airflow friction is much lower and molecules will have a non-zero speed relative to the surface[7]. This is graphically shown in figure 13 [28].

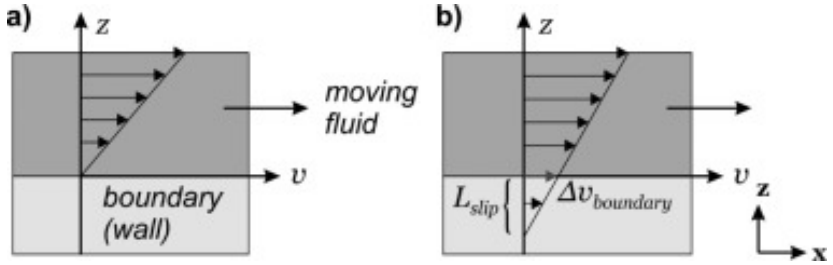

Figure 13: No-slip(a) and Slip(b) conditions graphically displayed [28]

To determine which flow regime is representative, the Knudsen number(Kn) is introduced. The Knudsen number is defined as

$$Kn = \frac{\lambda_{fp}}{L} = \frac{M}{Re}\sqrt{\frac{\gamma\pi}{2}} \tag{19}$$

In this equation λ_{fp} is defined as the mean free path and is related to the density [7]. It can be seen as the length a molecule can travel before it collides with another molecule[28]. For normal conditions at sea level for example, λ_{fp} has a value of $6.63e^{-8}$ m and this value increases when pressure decreases. Furthermore, L represents the characteristic length of the object, which in pipes where the length is much larger than the radius is estimated by the radius.

The Knudsen number provides a limit on which theory and assumptions are valid for the conditions and will determine when the low-density flow regime is reached. For $Kn < 0.001$ the no-slip condition is still valid. For $Kn < 0.2$ the continuum Navier-Stokes equations are still valid if slip conditions are taken into account. Above a value for Kn of 0.2 a continuum is not present anymore, an statistical methods should be used to evaluate flow conditions [28]. From $Kn > 1$ the flow regime starts becoming free molecular flow[28][7]. A schematic overview is given in figure 14[7].

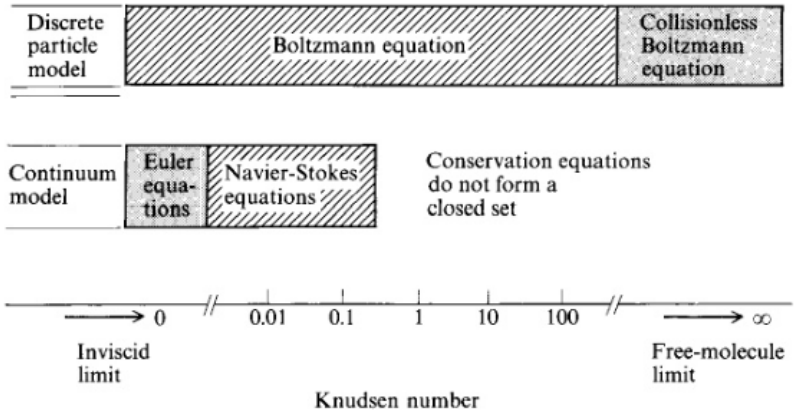

Figure 14: Knudsen number regimes for valid theory [7]

For the SpaceX Hyperloop competitions a Knudsen number in the order of $O(10^{-6})$ is estimated for the flow conditions of 860 Pa and speed of 112 $\frac{m}{s}$[25]. For this Hyperloop tube breach research a Knudsen number of $1.33 \cdot 10^{-4}$ is calculated with equation 19 using a radius of 0.05 m and at a pressure of 1000 Pa.

2.5.3 Shockwave effects through the channel

A pressure difference exists between the air inside the channel and the ambient outside the channel. If the breach hole is opened, this pressure difference will be instantaneous: the ambient air will flow into the channel, however the airflow is limited by the size of the breach hole. For a sufficient pressure difference, a shockwave at the breach hole will occur due to the instantaneous pressure difference and discontinuity: a compression wave moving into the channel and a expansion wave moving away from the channel[8].

The occurrence of shockwaves will be explained in further detail by introducing the Riemann problem. The Riemann's initial value problem can be formulated when two initial uniform states exist, separated by a discontinuity[8]: this situation can be related to Hyperloop breach by viewing the two initial uniform states as the inside and outside of the tube in which the speed of air is zero and the location of breach, which is the breach hole after the breach occurs, as the discontinuity. To simplify this the shock tube problem is shown, in which a shockwave initiates inside a constant area tube as a result of a discontinuity. A graphical overview of this situation is shown in figure 15[6].

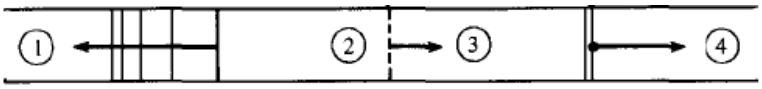

Figure 15: Overview of the shock tube for Riemann problem definitions[6]

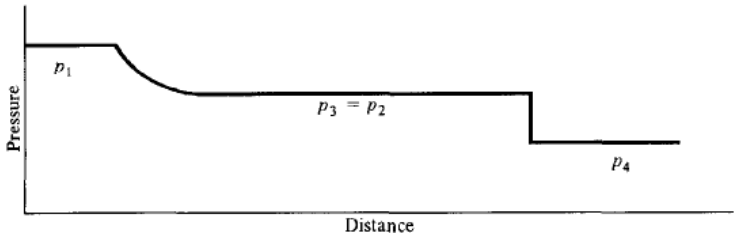

Figure 16: Pressure at different locations in the shock tube[6]

Four different states can be identified, in which zone 2 and 3 are separated by the discontinuity. Zone 4 is the zone in front of the shockwave moving through the tube, while zone 3 is the zone behind the shockwave. Zone 1 is the zone in front of the expansion waves moving through the tube in opposite direction, while zone 2 is the zone behind the expansion waves. To provide a better understanding, a drawing of the pressures at each location in the tube is shown in figure 16[6].
The process after the contact discontinuity is initiated can be visualized by using a $x - t$ diagram shown in figure 17[8].

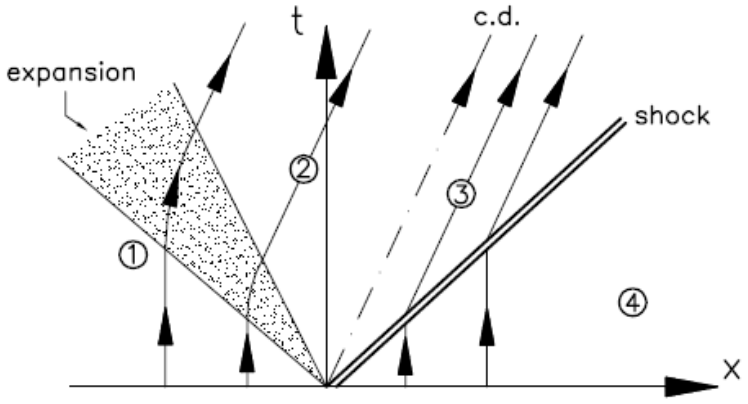

Figure 17: x-t diagram after the breach hole is opened[8]

The zones as indicated in figure 15 are present in the x-t diagram as well. With the zones indicated, a method has to be found to analyze the pressure difference over the shockwaves at each zone. Since the properties on different sides of a shockwave are investigated, the Rankine-Hugoniot conditions can be used and expressed as the continuity equation

$$\rho_3 u_3 = \rho_4 u_4 \tag{20}$$

the momentum equation

$$p_3 + \rho_3 {u_3}^2 = p_4 + \rho_4 {u_4}^2 \tag{21}$$

and the energy equation

$$h_3 + {u_3}^2/2 = h_4 + {u_4}^2/2 \tag{22}$$

By viewing u as the the velocity relative to the shockwave rather than the absolute velocity, the equations hold for both stationary and moving shock waves[6]. Furthermore, by using the velocity relative to the shockwave, the equations can be rearranged and solved for the properties over the shockwave when assuming a calorically perfect gas as

$$\frac{T_4}{T_3} = \frac{p_4}{p_3}\left(\frac{\frac{\gamma+1}{\gamma-1} + \frac{p_4}{p_3}}{1 + \frac{\gamma+1}{\gamma-1}\frac{p_4}{p_3}}\right) \tag{23}$$

Furthermore, by using the fact that the velocity of the shockwave is dependent on the pressure ratio over the shock and γ, as was determined from equation 9 and solved for the shockwave velocity $|c_s|$[6],

$$|c_s| = a_3\sqrt{\frac{\gamma+1}{2\gamma}\left(\frac{p_4}{p_3} - 1\right) + 1} \tag{24}$$

and by realizing the velocity behind the wave is dependent on the shockwave velocity $|c_s|$ and the density ratio[6],

$$u = |c_s|\left(1 - \frac{\rho_3}{\rho_4}\right) \tag{25}$$

the relation for the velocity at zone 3, as was defined in figure 17, as a function of the speed of sound a_3, γ and the pressure ratio over the shockwave is given by[6]:

$$u_3 = \frac{a_3}{\gamma}\left(\frac{p_4}{p_3} - 1\right)\sqrt{\frac{\frac{2\gamma}{\gamma+1}}{\frac{p_4}{p_3} + \frac{\gamma-1}{\gamma+1}}} \tag{26}$$

The next step is to determine the conditions across the expansion wave. To do this, first it is known that the Riemann invariants are constant through the expansion wave[6], thus

$$u + \frac{2a}{\gamma - 1} = constant \tag{27}$$

and for isentropic flow it therefor follows that[6]:

$$\frac{p_2}{p_1} = \left(1 - \frac{\gamma_1 - 1}{2}\frac{u}{a_1}\right)^{\frac{2\gamma_1}{\gamma_1 - 1}} \tag{28}$$

Solving this equation for the velocity u_2 gives

$$u_2 = \frac{2a_1}{\gamma_1 - 1}\left[1 - \left(\frac{p_2}{p_1}\right)^{\frac{\gamma_1 - 1}{2\gamma_1}}\right] \tag{29}$$

which provides the velocity at zone 2. It was determined using figure 16 that the zones after the shockwave and the expansion wave have passed have equal pressure and velocity. This thus means

that $u_2 = u_3$, and by equating equations 26 and 29 and solving for the pressure distribution across zones 1 and 4, the following relation is established[6]:

$$\frac{p_1}{p_4} = \frac{p_3}{p_4}[1 - \frac{(\gamma-1)(\frac{a_1}{a_4})(\frac{p_3}{p_4}-1)}{\sqrt{2\gamma(2\gamma+(\gamma+1)(\frac{p_3}{p_4}-1)}}]^{(}\frac{-2\gamma}{\gamma-1}) \tag{30}$$

This relation is useful for determining conditions for a constant area tube, which the Hyperloop tube is.

Shockwaves are a 3D phenomenon: the way in which the shockwaves propagates through the channel is not only determined by the initial pressure difference, but also the geometry in the channel itself. If the breach hole is in the wall of the tube, a shockwave moving into the tube interacts with wall on the opposite side of the tube. From there the shockwave propagates through the channel to both ends of the tube and these shockwaves become perpendicular to the tube wall after sufficient distance from the breach hole has passed[8]. For this reason results from quasi-1D analysis and from theoretical equations will not directly translate to physical test results, however they do provide insight on the expected results. The effect shockwaves have on the design and predictions of the Hyperloop breach tests will be discussed in section 3.1 and chapter 5.

2.6 Methodology

With important parameters, literature and potential phenomena relevant to Hyperloop breach established, in this section it will be discussed what requirements they impose on the experimental setup and measurement techniques used for Hyperloop breach research.

To determine the effects of Hyperloop breach on a Hyperloop pod, a scaled physical test will be performed. A scaled test setup is required since the proposed tube diameter of 4.5 m for future Hyperloop operations is too large for Hyperloop breach testing at this stage of development. Furthermore, a smaller test setup is controllable in terms of containing a vacuum, measurement techniques and testing space requirements. A scaled test setup is still required to provide a representative result, such that the results can be used to analyze full scale Hyperloop operations. For this reason, parameters as have been discussed in this section such as blockage ratio and Knudsen number need to be compatible with the scaled physical test setup.

To measure data from the scaled physical test setup measurement techniques are required that are possible at both the test location as well as compatible with a Hyperloop tube and pod. For this reason a non intrusive measurement technique is selected: a measurement technique that does not interfere with air flow and shockwave effects through the tube and does not increase any possible leak rates are preferred. Background oriented schlieren(BOS) is the chosen measurement technique for this research, since it fits the listed requirements, and this measurement technique is explained in detail in chapter 4. By using this measurement technique, extra requirements are necessary for the test setup: BOS uses optical images taken using a camera. A camera with sufficient resolution is required to take sharp images in which small disturbances in the medium can be captured in sequence. Furthermore, this camera needs to be mounted rigidly such that outside disturbances do not affect the images taken in a series. Any disturbances obtained from images needs to be strictly from changes in the medium inside the tube.

If the camera is placed outside of the tube, an extra set of requirements is imposed on the design of the tube. The tube material has to allow for light to pass through in order for the camera take images of the medium inside. It is therefor chosen to use Plexiglas(PMMA) as the material for the tube: it allows light to pass through, can be used to build custom made tubes and is a cheap but strong material. The material is prone to scratches and imperfections however, thus handling of the tube has to be done with care.

To attain a near vacuum state inside the tube, a source to provide a vacuum is required. The HTFD hypersonic windtunnel at the High Speed Lab(HSL) of the TU Delft has a vacuum vessel to which a tube can be mounted, which is a sufficient source to provide a vacuum environment. The Hyperloop tube thus has to be able to slot onto the vacuum vessel in an air tight seal, to prevent air leaking into the tube.

For the BOS measurement technique a background pattern needs to be visible on the images: this way, any disturbances in the medium can be correlated to changes in the background pattern as observed by the camera. The background pattern consist of a large number of speckles sufficiently close to each other. Movement in these speckles can be observed on the images taken by the camera. Loading these images in the correlation computer program Davis allows for calculating local displacements between images taken by the camera. The theory behind BOS and the method it is applied in this research is explained in more detail in chapter 4.

To ensure the scaled physical test setup provides sufficient results, it needs to be validated using numerical analysis and representative models. A ray tracing model allows for the calculation of light rays passing from the background image, through the tube and the medium and the camera lens. By using similar sizing and distances between measuring tools as used in the physical test setup, the displacements from the measurements can be compared to values expected from the ray tracing model to provide pressure values.

3 Test Equipment and Preparation

In the previous chapter the methodology for fulfilling the research objective was outlined, which includes using a physical test setup. In this chapter the requirements and implementation of the test setup equipment are explained. Each part of the test setup is explained, starting with the Hyperloop breach test tube and connection rings in section 3.1. This explanation includes the integration with other parts, material choice and sizing of the tube. Finally, in section 3.2 the Hyperloop pod design is discussed. The focus is on the sizing to match the pod blockage ratio based on drag estimations, its shape and design and the production method.

The scaled physical test setup is representative of the real full scale Hyperloop, such that results from the tests can be applied and used for full scale design of the Hyperloop Tube and Hyperloop Systems. Several conditions and limitations have to be accounted for, as will be explained in this section. For the breach testing at the High Speed Lab of the TU Delft several parts created and ordered. In this section decisions made for the construction of these parts will be explained as well as implementation into the test setup. To provide an impression of the test setup components before each component is described in detail, a 3D impression of the test setup components is shown in figure 18.

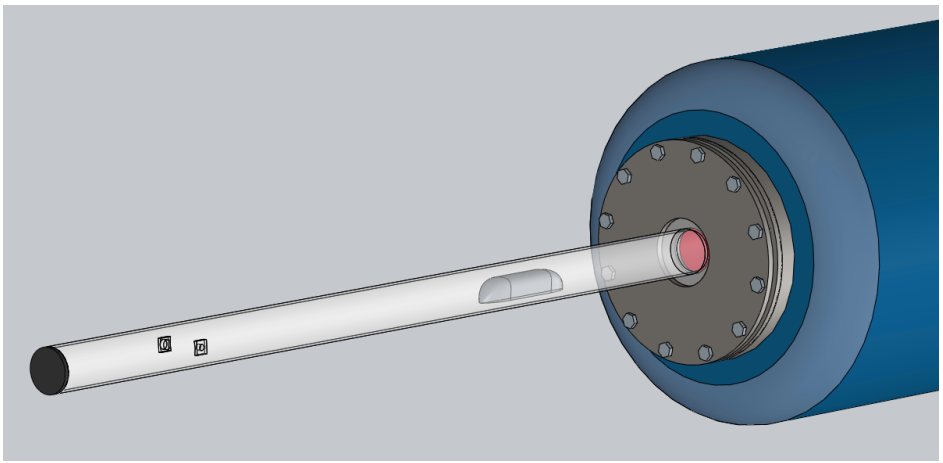

Figure 18: Test setup including main elements. Supports and measuring equipment are not present for visibility

3.1 Hyperloop Breach Test Components

Before going into detail on each individual component, the requirements of the test setup and its components will be explained. As was established in the methodology in the previous section, the test will be performed at the HTFD hypersonic windtunnel facility of the HSL. This means that any parts or components used in the test need to be compatible with existing architecture and equipment: the Hyperloop tube and connection rings have to match the sizing of the vacuum tank present at the HTFD. The diameter of the tube and connection rings are therefor directly determined from the

vacuum tank. The outer diameter of the tube is fixed to 100 *mm*. A greater diameter would increase the required wall thickness, increase vacuum losses, increase costs and require scaled pods greater than can be 3D printed in one piece, which will be explained in further detail in section 3.2. The inner diameter of the tube is 90 *mm*, thus a wall thickness of 5 *mm* is used.

The next requirement is that the test components allow for the use of background oriented schlieren. A camera setup has to be available and feasible such that constant stable images can be taken of the test section. To accommodate this, the tube has to allow for images being taken of the inside of the tube, which can be done by choosing a transparent tube material. The tube in which Hyperloop breach testing takes place is therefore made of Plexiglas(PMMA). The reason for this material choice is its light transmittance of 92% [19]. This allows for the use of background oriented schlieren measurements.

The length of the tube is based on shockwave requirements: a shockwave originating from the breach hole in the tube should have sufficient distance to the start of a Hyperloop pod. The reason for this is that the shockwave will form a wave that is perpendicular to the wall of the tube if sufficient distance has passed. An example of this is shown in figure 19, in which the shockwave development for two different explosion masses is shown[10]. From this analysis it requires a distance of approximately two tube diameter before a shockwave is formed that is perpendicular to the tube wall. Shockwave estimations for this research are discussed in more detail in section 5.4.2.

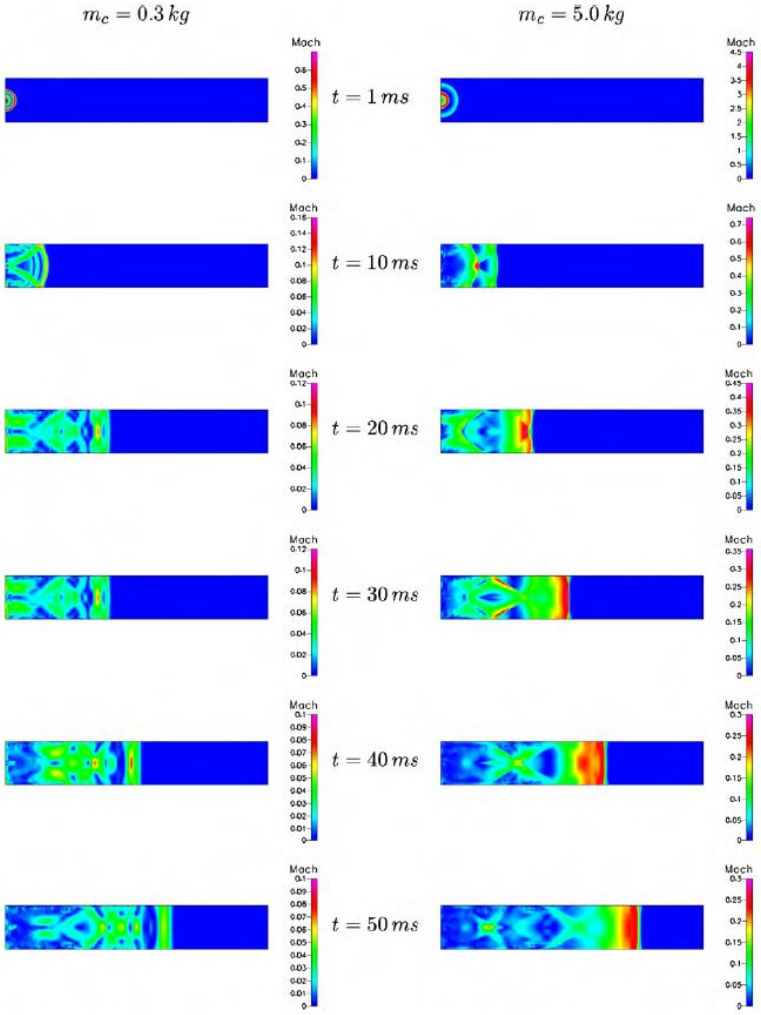

Figure 19: Shockwave development from a blastwave[10]

Another requirement is that the tube remains stiff and rigid during testing. The tube has to be able to withstand the pressure changes inside the tube. Furthermore, if the tube deforms due to the pressure change, the pictures taken by the camera could be influenced as well. A finite element analysis was therefor performed on this tube to ensure it can operate at 1 *bar* overpressure, with the results and details shown in Appendix A.

Two breach holes are created in the tube, supported by square strengthening elements as to counteract the loss of stiffness due to applying holes in the structure. The holes have different sizes to support testing of the sensitivity of breach hole size. The holes are applied on opposite sides of the tube with sizes of 13.16 *mm* diameter and 20.96 *mm* diameter, which are standard sizes for pneumatic

applications.

To finalize the design, a flange support is attached to the tube. This support is made of the same material to allow for using an adhesive to bond both pieces together. The flange support is used to attach the tube to the vacuum chamber. A Solidworks impression of the tube is shown in figure 20. A detailed drawing with all dimensions of the tube can be found in Appendix B.

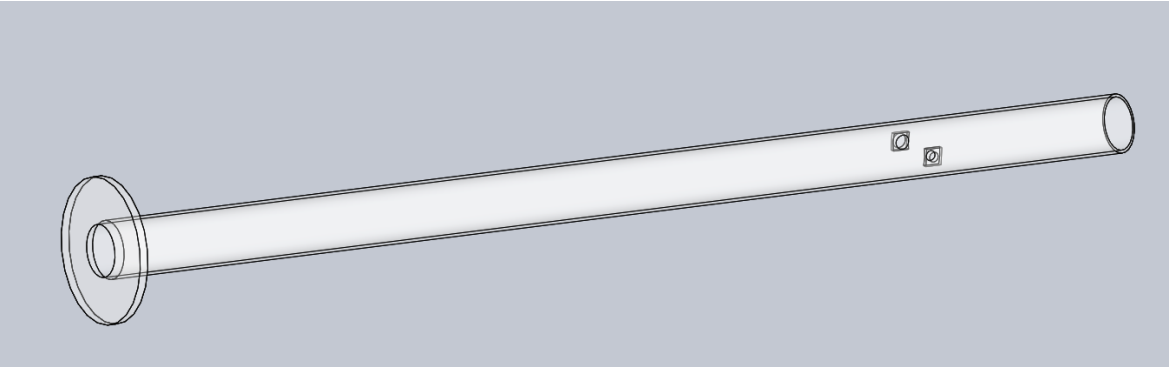

Figure 20: Solidworks image of the PMMA tube used for Hyperloop breach testing

Two custom rings were designed to fit over the PMMA flange of the tube. The rings are attached to the vacuum chamber using bolts, clamping the PMMA flange in between the rings. To determine the sizing of the rings, schematic drawings of the vacuum chamber and the supports of the HTFD were used, which are provided in appendix C.

The inner ring, with respect to the vacuum chamber, has a hole cut out in the center with a diameter of 100 *mm*. This aligns with the outer diameter of the tube of 100 *mm*, while the inner diameter of the tube is 90 *mm*. This allows for slight misalignment when connecting all the parts of the experimental test setup, making sure that air can flow undisturbed out of the tube and into the vacuum chamber.

The outer ring, with respect to the vacuum chamber, has a hole cut out in the center with a diameter of 150 *mm*. This diameter is larger than the diameter of the inner ring. The is because the outer ring is moved over the length of the tube to make the connection with vacuum chamber, as shown in figure 18. The base of the tube is clamped between both rings, with rubber rings ensuring air-tightness. These rubber rings are placed in the grooves of the metal rings with a diameter of 200 *mm*. The rings are connected to the vacuum chamber using bolts that fit through the outer holes in the rings. Detailed drawings of these rings can be found in figures 90 and 91 of Appendix C.

3.2 Hyperloop Pod

To investigate the effect of a breach on the Hyperloop pod, a scaled physical model is used in the tests. To ensure the results from the test are useful to not only the current setup scale, but also the full size Hyperloop, Hardt Hyperloop provided concept drawings of their Hyperloop pod design. These

drawings were designed for a high speed test facility in which Hyperloop design and safety procedures will be tested. For this reason the design is scaled to the Hyperloop breach setup dimensions.

3.2.1 Pod blockage ratio

To choose the correct dimensions, a blockage ratio has to be determined, which is the area taken up by the pod divided by the inner cross sectional area enclosed by the tube. Since the pod itself will have a cross sectional area while moving through the tube, the air will have to flow around the pod. The investigation by Wong described in section 2.3 uses the drag increase caused by the blockage ratio as a method to determine an acceptable blockage ratio. As was described and shown in figure 11, a blockage ratio of 0.625 was found satisfactory for Hyperloop. The estimation of the blockage ratio for this research will also be 0.625, however further contact with Hardt Hyperloop established that while they use this value, this also includes internal system such as the tracks. Hardt suggests using the value of 0.625, while including any guidance or support systems used when mounting the pod in the Hyperloop breach test setup[16].

3.2.2 3D Model

The pod drawings from Hardt had to be scaled down to fit the size of the test setup. For this reason a recreation of the pod was made using Solidworks by measuring the angles and length of each section of the pod. The pod geometry is shown in figures 21 and 22.

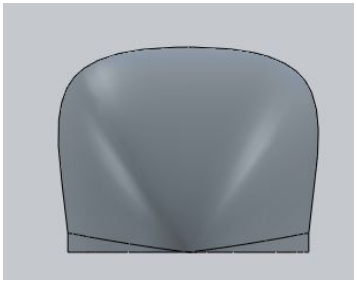

Figure 21: Front view of the pod model

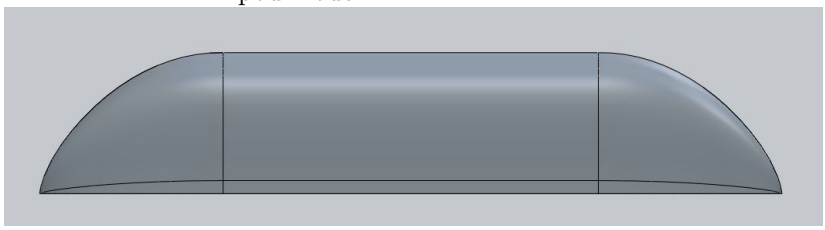

Figure 22: Side view of the pod model

The length of the pod was scaled as well such that 3D printing the model was possible with the 3D printers available at both Tata Steel and the High Speed Lab in Delft, the Ultimaker S3. The length of the pod is 255 *mm*. Furthermore, the model was made in Solidworks and saved as a stereo lithography(STL) file using the finest possible settings. Afterwards the file was exported to the software Ultimaker Cura, in which the file was prepared for the 3D printer.

3.2.3 3D Printer settings and decisions

The pod is printed in layers by the 3D printer using polyactic acid(PLA) as a material. A shell thickness of 1.2 *mm* is used for the Hyperloop pod to be sufficient in strength. With each layer being 0.1 *mm*, multiple passes of the 3D printer are required to create the shell. For 3D printing the inside of the pod is hollow and replaced by a supporting structure. Since the pod will be subjected to an outside vacuum, the supporting structure has to be chosen carefully. To alleviate pressure differences between the in- and outside of the pod during testing, a hole 3.8 *mm* in diameter is drilled into the pod. Furthermore the inside supporting structure is made up of thin layers running horizontally through the pod (perpendicular to the hole). This way, if the hole is drilled through each layer, all compartments in the pod are connected to the outside. This allows for air to escape from inside the pod, thus ensuring the same pressure on the inside and the outside of the pod.

Since the pod will be printed from front to end vertically, a support is printed as well. Without this, the pod would fall over after the first section is printed due to the curvature of the tail end of the pod. The support is printed to the pod with one pass from the machine, thus it can be removed from the actual pod without requiring a large force. This does mean some smoothing is required after the machine is done, however this can be done using sandpaper. Furthermore, the affected side of the pod will be used as the tail end of the pod in the test setup, allowing flow over the undisturbed smooth part first.

The decision was made to first 3D print a pod on a smaller scale: while the pod would have the same length, the blockage ratio would only be 16%. The reason for this is that it had to be determined if the 3D printed pod was suitable for the test in both smoothness and structural integrity. Furthermore, if a fault occured while printing the larger pod, a larger amount of material would have been wasted. The smaller pod can also be used during testing to determine the effect of blockage ratio on the consequences of breach. The resulting pod is shown in figure 23. After the results were found satisfactory, the intended 3D scale was created. That pod has a blockage ratio of 60%, with a 2.5% margin to account for connection methods to the tube.

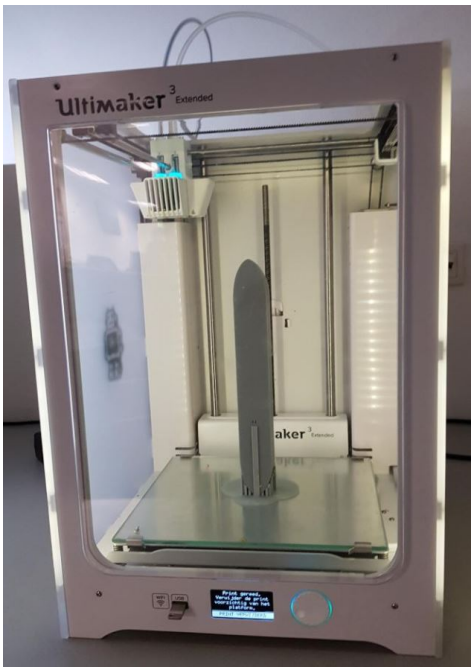

Figure 23: The 16 % blockage ratio pod after the 3D printing operation was finished

4 Measurement Techniques

In this chapter the measurement techniques for the research will be explained, starting with background oriented schlieren(BOS) in section 4.1. Once the working principle is established in section 4.1.1, the physical and digital requirements are stated in section 4.1.2. The importance of timing and synchronisation is explained in section 4.2. Finally the options and settings required for image correlations and data processing are explained in section 4.3.

4.1 Background Oriented Schlieren

4.1.1 Working principle

To determine the effects of a Hyperloop breach, a non-intrusive measurement technique was sought that does not interfere with the breach hole or the air propagation. Background oriented schlieren is such a non-intrusive measurement technique and equipment to perform the breach experiment using BOS was available at the HTFD facility of Aerospace Engineering faculty of the TU Delft. BOS is a visualisation technique that uses the density of a medium and its refractive indices to visualize flow properties. A schematic overview of the processes involved in attaining information from the BOS technique is shown in figure 24. The BOS method is explained in several steps. First of all, a reference image is taken using a camera focused on the test section. Generally, a background pattern is placed in the test section, such that images taken by the camera contain pixels easily identifiable by correlation software. After the experiment is started, images of the same test section are taken, such that the only difference between images is the change in medium in the test section as a result of the test itself. By correlating the images using correlation software, an optical flow field is established in which pixel movement between the reference and the distorted image are visualised. From this, a displacement field can be created in which the displacement for each pixel is stored by adding the distance per pixel. This can be done by taking an image with the camera in which a defined distance unit can be read off, such as using graph paper. An example of a BOS image and its software application is shown in figure 25. To attain a relation for this, the Gladstone Dale constant

$$n = 1 + K\rho \tag{31}$$

is introduced[14]. In this equation n is the index of refraction, ρ is the density and K is the Gladstone Dale constant, which relates the index of refraction to the density of the medium.

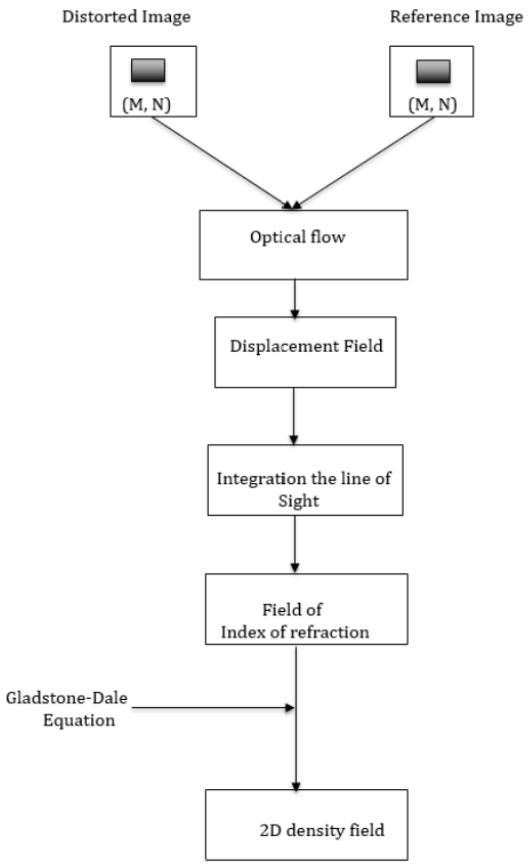

Figure 24: Schematic overview of BOS method[14]

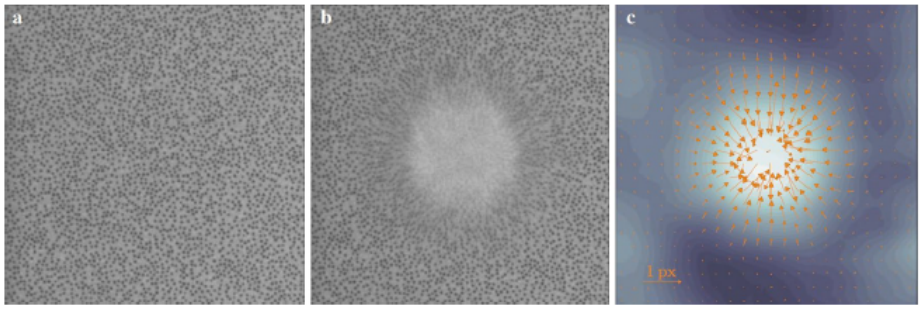

Figure 25: BOS image method: image a is the reference image, image b is the image with a distorted medium and image c is the measured displacement field[27]

To determine the effect of the density change in the medium, a relation is used that relates the viewed image by the camera to actual geometry and distance between each distinct pixel. To do this, the lengths and angles are defined as shown in figure 26.

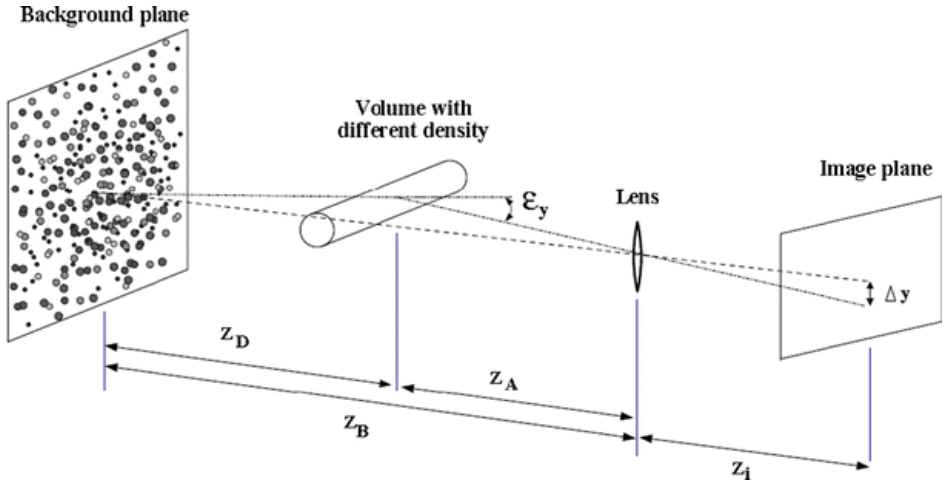

Figure 26: BOS method definitions[27]

The equations

$$\Delta y = Z_D M \epsilon_y \tag{32}$$

and

$$\epsilon_y = \frac{1}{n_0} \int \frac{\delta n}{\delta y} dz \tag{33}$$

provide the relation between image plane and angle ϵ_y[27]. Combining these equations results in

$$\Delta y = f \frac{Z_D}{Z_D + Z_A - f} \epsilon_y \tag{34}$$

which holds for small angles of ϵ_y, where the angle is assumed equal to its tangent function. This equation shows a great importance of the ability to provide clear, sharp images: in order to determine Δy from images taken in a BOS experiment, the focal length of the lens used must be compatible with its distance to the background pattern plane. In these equations n_0 is the reference index of refraction, f is the focal length of the lens and Z is the notation for distances between specific objects as shown in figure 26[27]. While these equations are true for simple setups, for airflow through an inhomogeneous density field the equations need to be expanded. The equation

$$\int n(x, y, z) ds = 0 \tag{35}$$

shows the effect of this on the refractive index, where s is the path the light takes through the medium[27]. The equation shows a 3D dependency of the refractive index, however to measure a 3D dependence multiple camera angles will be needed, since each camera itself can only take images of

one plane. In order to evaluate a 3D density field thus either a multiple camera setup is needed or the 2D plane images of the camera used in the test need to be analyzed further, such as by using a ray tracing model.

4.1.2 Camera, light and background pattern requirements

The BOS tests use a camera to determine the density changes in the medium. Because of this, the settings and properties of the used camera are of high importance. First of all the focal length settings need to be chosen such that the entire area of interest is captured on the camera image. This is done in combination with the distance the background patterns have to the medium[27]. Secondly the images taken by the camera need to have a brightly illuminated background pattern visible, such that changes in the medium are detected for the whole length and width of the image. This can be done by placing a strong light source from behind the speckle background pattern while making sure light can shine through this pattern. Alternatively light can be installed below or above the test setup, however this should be done consistently due to the refractive index of the tube material.

Since the background pattern is captured by a camera of a specified focal length, the amount of pixels each dot in the background pattern represents determines the usability of the image data. Furthermore, the area between each dot on the background pattern should be small, since the distorted dots are used in processing displacements in the medium.

4.2 Timing and Synchronisation

For experiments in which measurements are taken by different devices, it is important to ensure each measurement is stored at the same time. The time of each image itself is obtained from the camera itself, in which the capture frequency is set before the start of the experiment. To synchronize all devices, a tool was created using Labview in which a pressure meter installed in the tube, the pressure reading from the vacuum chamber and the camera are connected. This way, the exact timing of all components can be determined and stored. The Labview program receives inputs from all connected devices and the inputs correspond to a value based on signal strength. For camera activation this corresponds to a near zero value becoming a value 10^4 times higher. This way camera activation can be inferred from the labview data and a timeline of the experiment can be established after the experiment is concluded. To receive all the inputs without missing any, the physical device connected to the labview program has to have an input frequency that at least matches the frequency of the pressure meters. If the input frequency is to high, a received signal might be registered more than once depending on the signal length. The input frequency is therefor checked for each different experiment to confirm the input signals are detected correctly.

Even though each signal is linked together, input delays on the pressure meters and devices itself could be present: the pressure meter inside the tube requires a build up of air going from the tube inside the measurement area, thus the pressure as observed by the pressure meter might not correspond to the actual pressure in the tube itself at the time of measurement. While this is an error source and can be minimized by proper installation of the pressure meter, it will affect the synchronization of measurements.

4.3 Image Correlation and Data Processing

With the requirements on measurements and the working principle of BOS established, the method of image correlation for Hyperloop breach needs to be explained in further detail by breaking down each step of the process. Images taken by the camera are stored for each different experiment. In order for the images to be used in a correlation, they have to be sorted and imported into Davis, the software used for image correlation. In the correlation, two images are compared and any pixel displacements are registered.

For this research, the correlation between subsequent images taken in an experiment can be used to determine sensitivity, presence of shockwaves and error size. When taking the first image of a sequence of images as the baseline image, the pixel shift compared to other images in the sequence can be determined. By using a reference image taken before an experiment is started, pixel displacements as a results of pressure changes in the experiment can be obtained from image correlation. Davis software creates image sets by importing images or image folders.

In Davis operations are performed in sequence as defined in the operation list. In the first operation, image sets from an experiment are loaded in from a folder. A double frame is created from the image sets supplied. For an image correlation operation in which the pre-experiment image is compared to an image taken during the experiment, a double frame is created from the first frame of each image set and continued until all images from both sets are processed into double frames. This way, the data sets are merged to one multi frame set. To be able to perform this operation, beforehand the first pre-experiment image is duplicated an amount equal to the total number amount of images in that experiment using Matlab and imported into Davis as an image set.

The next operation applies scales to the frames. Scales are determined by providing a length scale to the images, thus defining the width of each pixel in millimeters. Before the experiment was performed, an image was taken using the same camera of the speckle background pattern overlayed with a centimeter paper sheet. From this image, the user is able to manually assign the width of each pixel based on the centimeter paper grid visible in the image. This operation is required for determining the size of pixel displacement determined from cross correlation.

With the scales applied, the next operation involves the settings, application and method of data correlation. The settings have to be conform the experimental setup, decisions and assumptions made. For this research, one camera is used, for which its pixel size is to be inputted in the settings. Furthermore, the time between frames or images can be deduced from the frequency in which images were taken using the camera. The correlation method is set at 2D cross correlation due to using one camera, however if more cameras were used other options would be feasible as well.

The cross correlation operation evaluates the double frame by dividing the frame into small windows, with the window size of each section supplied by the user. A shift in pixel displacements in the double frame is stored for each small divided section, shown in figure 27. The cross correlation itself is performed using a vector calculation, in which each window has a vector corresponding to the pixel displacements.

The size of each small window is of great importance: if the size is too large, local disturbances cannot be distinguished. If the size is too small, the density of the background pattern speckles could

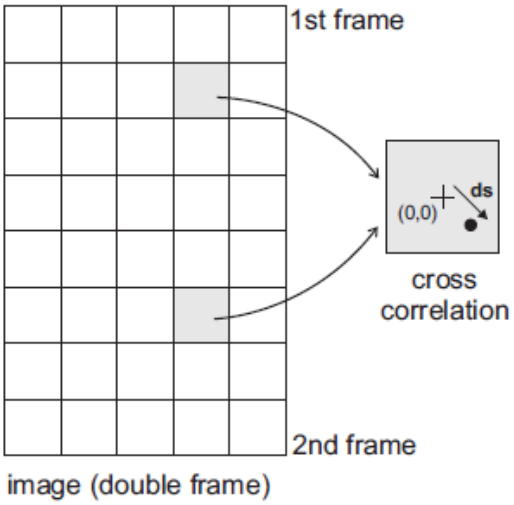

Figure 27: Cross correlation operation for double frame[21]

be too small, thus not having enough speckles in the window for proper cross correlation. Furthermore, having more windows increases software operation time, since more computations are required this way. The conditions for subdivision of frames thus becomes a combination of background pattern speckle density, image resolution, required local accuracy and software operation time.

Any disturbances due to lighting or objects in the test section will affect the results of the cross correlation operation. To prevent disturbances unrelated to the experiment from interfering, masks can be applied to the image. A mask is a shape applied over the image that can either include or exclude a part of the image from the cross correlation operation. Masks are applied as a predefined shape or as a polynomial function, after which the shape is attached over the image. For Hyperloop breach research, masks are used to cover image edges with insufficient light and Hyperloop pods placed inside the tube. Hyperloop pods are covered using a polynomial function that covers the outline of the visible pod section in the image, since the pod exterior does not contain a background speckle pattern as used for cross correlation operations. Without a mask applied over the pod, high pixel displacements over 10 times higher than the non pod covered area would appear after cross correlation operations as result of lack of background pattern on the pod.

Once the operations are performed, the results are exported from Davis and imported into Matlab. The data is stored in Matlab as matrices of displacements corresponding to each small section of the processed images. This way, the location in both horizontal and vertical direction is associated with a displacement and the time of the measurement. By combining the exported data with pressure meter measurements and their corresponding measurement time, a full timeline of all measurement can be made and used for further processing, as will be explained in more detail in section 5 by introducing the Snell's law model.

5 Optical Modelling of the Experiments

While in the previous chapter the working principle and requirements on the measurement techniques were explained, in this chapter the optical modelling of the experiments is described, which includes expected testing conditions and models to analyze test results with. A model based on Snell's law is introduced, including equations for determining the refractive index based on the air composition, which will be used evaluate test results. To understand why these equations and a model based on Snell's law are needed, a brief overview of the test setup will be given. In the test setup, the test section consists of a tube with a camera present on one side of the tube and a background pattern present on the other side of the tube. The overview of the test setup with a section of the tube is shown in figure 28. The full experimental setup will be explained in chapter 6.

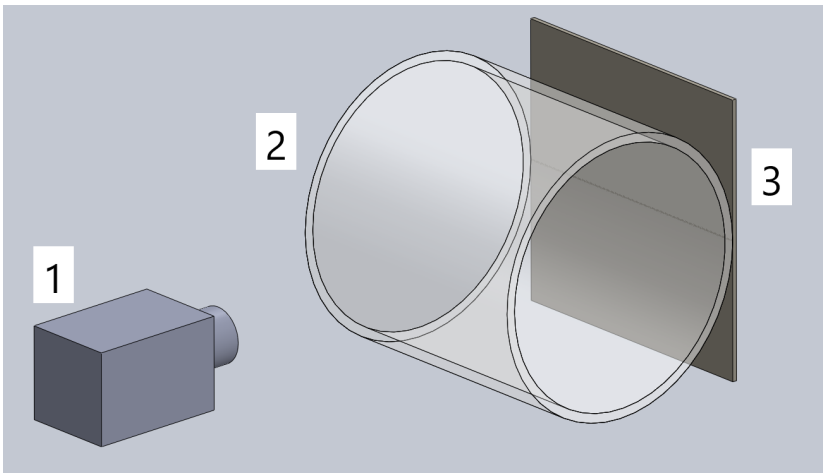

Figure 28: Overview of the test setup, including 1. Camera, 2. Tube segment, 3. Speckle pattern plate

5.1 Snell's law

From the description of BOS in the previous chapter, a camera is used to take pictures of the test section using a background pattern. Since for Hyperloop breach testing a tube is present in the test section, pictures taken by the camera are affected by this. The light beams captured by the camera do not travel along a straight path: due to the curvature of the PMMA tube, the light beams will be refracted in its path. Furthermore, a change in pressure of the air inside the tube changes the refractive index n. To predict this behaviour, a ray tracing Matlab model based on Snell's law is made. Snell's law,

$$\frac{sin\theta_2}{sin\theta_1} = \frac{n_1}{n_2} \tag{36}$$

is used to determine the change in light beam path when passing from one medium to another. A visualization of this is shown in figure 29.

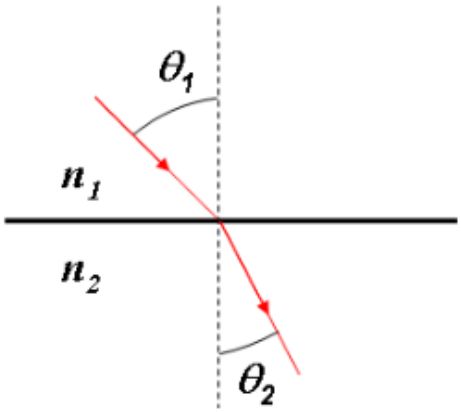

Figure 29: Effect of the refractive index on the light beam path passing through the PMMA tube [24]

During Hyperloop breach testing the inside pressure of the tube will be different compared to the outside ambient pressure. Due to this, the air inside the tube will have a different refractive index. The dependency of the refractive index on pressure was calculated and measured by B. Sang and T. Jeon [30], with the results for different gases shown in figure 30. An increase in pressure of the medium increases the refractive index. Combining this with Snell's law shown in equation 36, this means that when the pressure in the tube decreases, the refractive index decreases, and the angle θ_2 increases, which is the angle after passing through the interface from PMMA to air inside the tube.

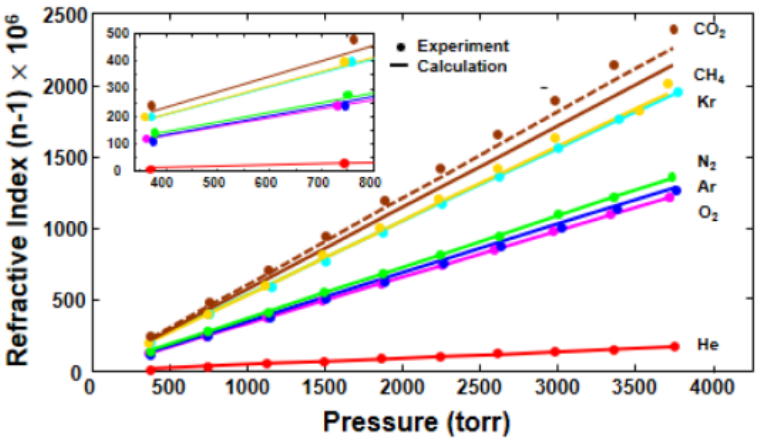

Figure 30: Dependency of the refractive index n on pressure for various gases[30]

To determine the exact refractive index, the air composition and humidity have to be determined.

For this experiment, the only variables for determining the refractive index are the measured temperature and the measured pressure. Standard air composition is assumed according to the molar percentages shown in table 1, in which gases with a very low percentage have been excluded.

Table 1: Standard air composition

Component	Percentage
N_2	78.09
O_2	20.95
Ar	0.93
CO_2	0.04

The refractive index is related to the air composition using the Lorentz-Lorenz equation:

$$\frac{n^2-1}{n^2+2} = \sum_i R_i \rho_i \tag{37}$$

in which R_i is the specific refraction and the "i" subscript is an air component. For low pressure regions however, determining the refractive index becomes difficult due to the lack of experimental evidence[31]. In order to determine a formula for the refractive index that is valid even for low pressure regions, Schödel performed experiments using a vacuum cell to determine whether existing expressions could be used to determine the refractive index in low pressures. To express the refractive index as a function of pressure, Bönsch's empirical equation is introduced and broken down in components[31].

First the dispersion equation for dry air,

$$\begin{aligned}(n-1)_{disp} = (8091.37 + 2333983/(130-(1/\lambda)^2) \\ +15518/(38.9-(1/\lambda)^2)) \cdot 10^{-8}\end{aligned} \tag{38}$$

is used to determine the effect of the wavelength λ for standard conditions using a temperature of $T = 20\,^{\circ}\mathrm{C}$, a pressure of $P = 100\,000\,\mathrm{Pa}$ and a CO_2 volume percentage of 0.04%[12].

To account for a different CO_2 volume percentage than 0.04%,

$$(n-1)_{CO_2} = (n-1)_{disp} \cdot (1 + 0.5327 \cdot (x_{CO2} - 0.0004)) \tag{39}$$

is used[12]. To account for a different temperature and pressure,

$$\begin{aligned}n_{TP} = (((n-1)_{CO_2} \cdot P)/93214.60) \cdot \\ (1 + 10^{-8} \cdot (0.5953 - 0.009876 \cdot T) \cdot P)/(1 + 0.0036610 \cdot T) + 1\end{aligned} \tag{40}$$

is used[12].

These equations hold for ideal gases, which are governed by the ideal equation of state[31]. It was found that the refractive index for the performed experiments in the 0 to 1300 Pascal pressure range were within 10^{-9} error compared to Bönsch's empirical equation for the wavelengths 532 *nm*, 633 *nm* and 780 *nm*. For the Hyperloop breach investigation, Bönsch's empirical equation will therefor be used in determining the refractive index[31].

With the equations using in the Snell's law model explained, the way the model operates and the parameters used will be explained in steps. The model uses the spatial variation in refractive index, due to the change in pressure and material, to predict the propagation of light beams.

The Snell's law model simulates a light beam starting at position x_1 and travels towards the tube. The point on the outer radius of the tube where this light beam enters the tube is point x_2. Subsequent points in which the light beam intersects the tube are defined as shown in figure 31.

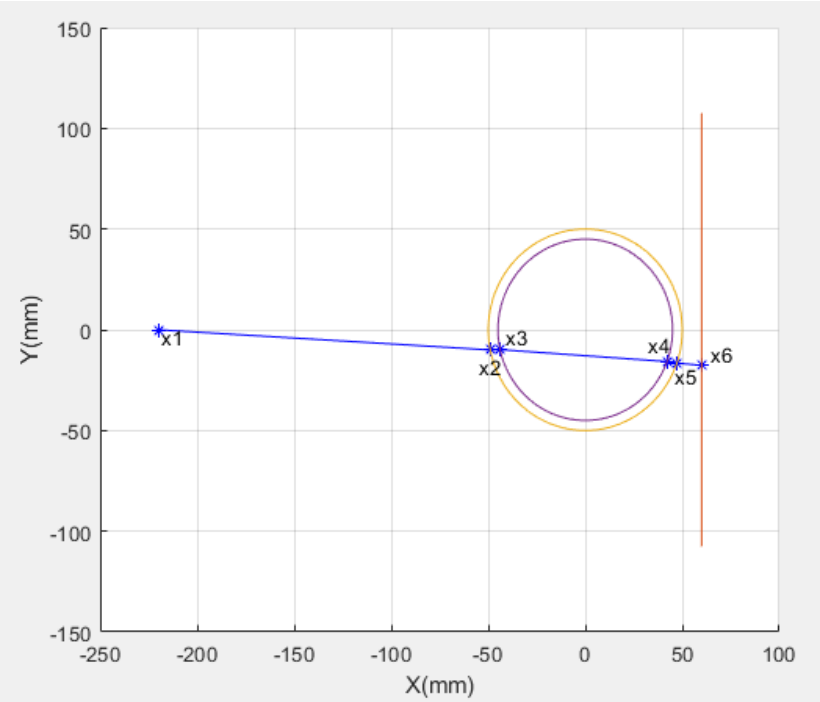

Figure 31: Definition of intersection points for light beam and tube intersections

The model has several purposes. Firstly it determines the angle at which the camera observes the light beams. Since the edges of the images taken by the camera will be distorted due to the tube curvature, the model can indicate the expected measurable zone of the tube. Secondly since the tube image is distorted at the edges regardless of the air pressure inside the tube, it has to be determined what the expected effect of the inside pressure change is: while computer software can correlate between the images of different inside pressures, a verification based on theory will strengthen its results.

To demonstrate the way the model works, an example will be shown in which the model is run using an inside pressure of 1 *bar* and 0.1 *bar*. While for the actual experiment the upper and lower bound of the inside pressure are 1 *bar* and 0.01 *bar*, these smaller values are used to demonstrate and visualize the sensitivity of light beam displacement to pressure changes. An ambient temperature of 288.15 K was assumed. The test dimensions of the tube of an inside radius of 45 mm and an outside

radius of 50 mm were used. The light beams of both cases were investigated at the center of the tube, indicated by $x = 0$ mm. An example of a two light beams originating from the same location and entering the outer radius of the tube at -40 mm from the center in Y-direction is shown in figure 32. In this figure, the light beams have a different path through the tube due the difference in pressure inside the tube and therefore a difference in refractive index. At the location of $x = 0$ mm, which is the center of the tube in X-direction and what is shown in figure 32, the distance between light beams is 0.0113 mm in Y-direction as a result of the different refractive indices. This example shows that the path a light beam takes is influenced by the angle it has going into the tube and the refractive index due to the pressure inside the tube.

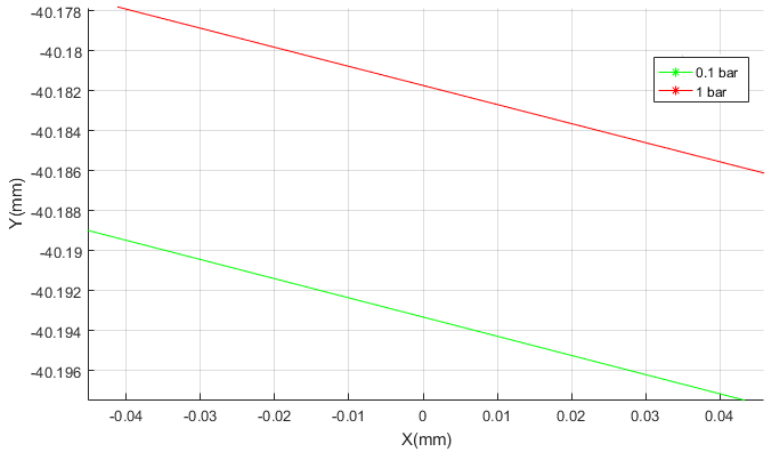

Figure 32: Light rays for the 1 bar inside pressure(red line) and the 0.1 bar inside pressure(green line) at the tube center

After providing the governing parameters for the Snell's law model in section 5.2, in section 5.3 an explanation on how the Snell's law model is applied to data obtained from Hyperloop breach experiments is given.

5.2 Governing parameters

While in the previous section the equations relevant for the Snell's law model are explained, in this section the important parameters that determine the effectiveness of the model are discussed. The parameters discussed in this section are used in the Snell's law model Matlab program and this section therefor provides an understanding of the underlying choices made in the creation of the Matlab program.

The initial parameters used for running the program relate to physical properties, sizes and distances of the test are shown as:

- Outer radius of the tube r_1

- Inner radius of the tube r_2
- Distance from the camera lens to the edge to the tube
- Ambient pressure at the testing facility p_1
- Temperature at the testing facility T

The values for these parameters are obtained from direct measurements at the facility. From these parameters values important to the Matlab script are calculated in steps. As described in section 5.1, the refractive index is used to determine the angles of the light rays passing through the Hyperloop breach tube. The angle of the light ray entering and exiting each station x as defined in figure 31 is calculated using the refractive index and the initial parameters listed. Using Snell's law and trigonometric equations and using the fact that stations two to five are located on a circle with a constant radius, the light ray angles are calculated at each station in ascending order, starting from x_1.

5.3 Application to test data

In the previous section the governing parameters of the Snell's law model were introduced. In this section it will be explained how this model is used in combination with data obtained from Hyperloop breach experiments.

The Snell's law model provides a theoretical basis to interpret data obtained from testing. In order to do this, the test data needs to be obtained in a format that supports this output. The Snell's law model uses displacements at a position from the center of the tube. In order to apply this to the test results as well, the tube center position should be clear from the obtained images. This is done by marking the tube center during the calibration of camera images using a background paper with a centimeter square grid. Furthermore, the camera was mounted and set up such that the lens looked straight through the center of the tube. Since very small displacements equate to significant pressure differences in the Snell's law model, small measurement errors from the tests can have large consequences when comparing test data to the Snell's law model.

The Snell's law model allows for assigning pressures to displacements obtained from the test data. To do this, several assumptions are made:

- *Measured displacements beyond correlation software error are purely from pressure changes inside the tube.* While factors that disturb the tube will occur, such as the manual opening of the breach hole and vibrations of the vacuum chamber, these cannot be quantified. These factors are therefor taken into account during the discussion of the results if the results show significant disturbances.
- *The tube material is assumed of constant thickness and light permeability.* While in reality this will not hold due to construction tolerances, as long as the images are taken from the same piece of tube every time, the imperfections will occur on all images. Therefore, the imperfections will not have a significant impact on the results of the correlation between these images.

- *The distance from the camera lens to the tube and the background pattern is measured from the test setup and assumed constant.* Since very small pixel displacements equate to significant pressure changes, differences in distances in the physical test setup compared to the refractive model cause inaccurate pressure results. While this can be mitigated by providing a sturdy experimental setup and clamping down individual elements, error sources due to this are expected.

Three parameters of the model can be identified: pressure inside the tube, position from the center of the tube and displacement of the light ray. The displacement is taken at the location of the background pattern, which is x_6 in figure 31, since correlation images obtained from BOS measurements provide pixel displacements based on speckles of the background pattern. The dependency is modelled in Matlab and show in figure 33, focused on the lower pressure range for visibility.

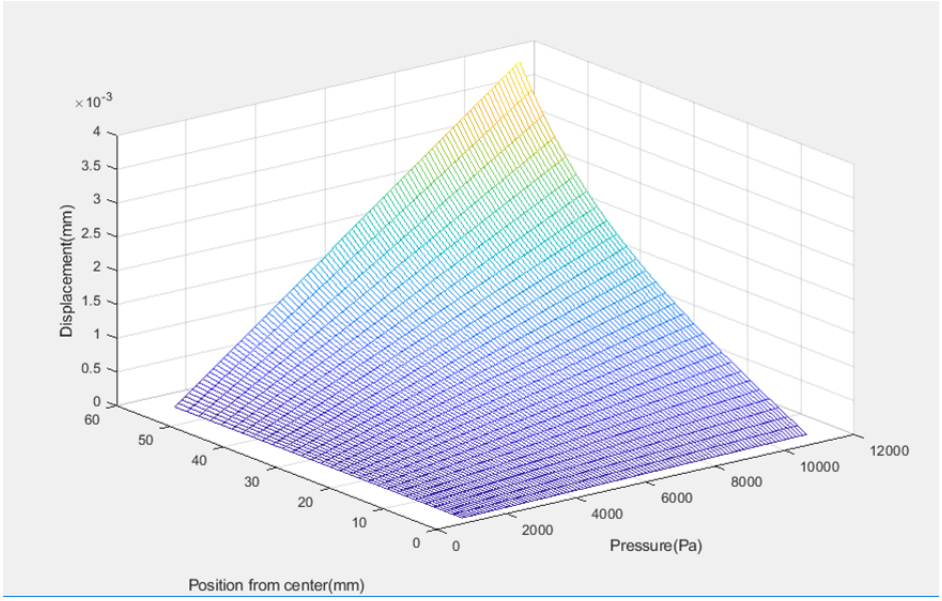

Figure 33: Refractive index model focused on the 1 to 10 kPa range. 1 kPa is the reference pressure from which displacements are calculated

Figure 33 also indicates the bounds on the expected size of displacements: since the physical experiments start at 1 kPa, which the model assumes as the reference in which no pixel displacements occur, all displacements are based on the reference position. Furthermore, since the pressure in the experiment increases until atmospheric pressure is reached, the pixel displacements are expected to be between 0 mm at 1 kPa and $4e^{-2}$ mm at 100 kPa.

To determine the local pressure of the test data, the displacements from the test images are first stored in a matrix. From the Snell's law model, for each pressure inside the tube its associated pixel displacement from light rays passing through the tube are known, as was shown in figure 33. To account for error sources and to determine the overall pressure at the image location, the mean displacement through the center of the pixel displacement images for each image correlation is calculated.

This way, a gradual increase of the mean displacement is expected when the pressure inside the tube gradually rises. The way the process of obtained mean displacements is done is explained in further detail in section 7.2.

5.4 Flow development through the Hyperloop tube

At the start of this chapter, an outline of the experimental setup is given. Before the experiment is started, the pressure inside the tube is lowered to 10 *mbar* using the vacuum tank connected to the tube. In the Hyperloop tube two breach holes are present, which are used to start the experiment. When the Hyperloop breach test is started by opening the breach hole, air will flow through the breach hole and into the tube due to the pressure difference between the inside and outside of the tube. The full experimental setup will be explained in chapter 6. The flow development through the Hyperloop tube is dependent on the breach hole and tube geometry, as well as the pressure difference between the ambient and the inside of the tube. In this section, a prediction will be made for this flow development with respect to mass flow rate and shockwaves.

5.4.1 Mass flow rate predictions

To provide a prediction on experiment time and breach hole quality, the mass flow rate through the breach hole and tube are calculated. Predictions for the mass flow through the tube and the breach hole can be made based on the tube geometry and the vacuum tank size. To do this, first the volume of the vacuum tank and the Hyperloop tube were calculated, resulting in a total value of 2.97 m^3. For the mass flow rate calculations, it is assumed that both the tube and the vacuum vessel fill up with air during the experiment, and the volume is the vacuum vessel is therefore taken into account. The tube dimensions are shown in appendix B. In section 2.4 the mass flow rate through an orifice was discussed focused on choked flow conditions, however to determine the mass flow rate throughout the experiment also the non-choked conditions should be taken into account. The mass flow for the choked condition,

$$\dot{m} = C_d A \sqrt{\gamma \rho_1 p_1 (\frac{2}{\gamma+1})^{\frac{\gamma+1}{\gamma-1}}} \quad ; \frac{p_2}{p_1} < (\frac{2}{\gamma+1})^{\frac{\gamma}{\gamma-1}} \tag{41}$$

depends on the breach hole area A and the discharge coefficient C_d, which is assumed at 1.0 for a smooth breach hole[15]. This assumption is supported by the fact that the breach hole material was of high quality and custom made for this experiment. In this equation p_1 is the pressure outside the tube and p_2 the pressure inside the tube. The mass flow for the non-choked conditions,

$$\dot{m} = C_d A \sqrt{2\rho_1 p_1 (\frac{\gamma}{\gamma-1}) \left[(\frac{p_2}{p_1})^{\frac{2}{\gamma}} - (\frac{p_2}{p_1})^{\frac{\gamma+1}{\gamma}} \right]} \quad ; \frac{p_2}{p_1} \geq (\frac{2}{\gamma+1})^{\frac{\gamma}{\gamma-1}} \tag{42}$$

contains terms that explain the mass flow dependency on pressure ratio between the inside and outside of the tube[15]. As was explained at the start of section 5.4, an experiment is started by opening one of the breach holes, after which air flows into the tube due to the pressure difference between the inside and outside of the tube. These equations are used to predict the experiment time, mass flow rate and pressure for those experiments. The equations are calculated for a time period of 600 second using 20000 time steps, providing mass flow rate and pressure values at each time step,

from which figures can be created. The calculated mass flow rate and the pressure for the small, 13.16 *mm* diameter breach hole are shown in figures 34 and 35 while the plots for the large, 20.96 *mm* diameter breach hole are shown in figures 36 and 37.

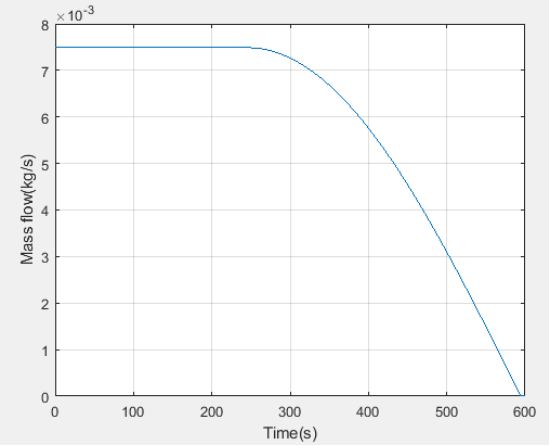

Figure 34: Mass flow ratio calculations for the small, 13.16 *mm* diameter breach hole

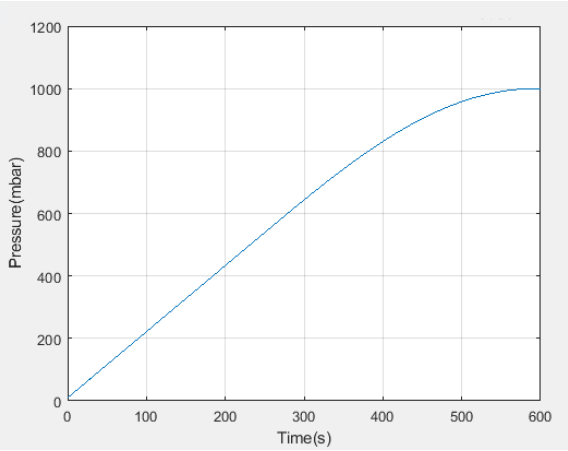

Figure 35: Pressure calculations for the small, 13.16 *mm* diameter breach hole

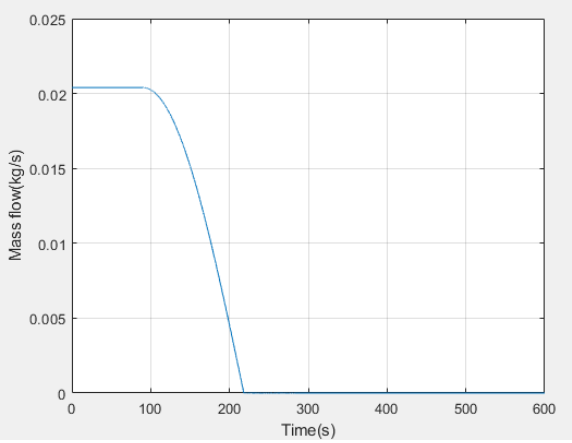

Figure 36: Mass flow ratio calculations for the large, 20.96 *mm* diameter breach hole

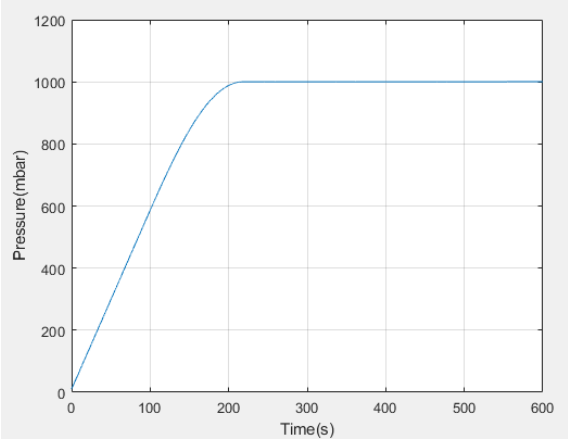

Figure 37: Pressure calculations for the large, 20.96 *mm* diameter breach hole

From the figures it can be observed that the large breach hole calculations have a higher mass flow rate compared to the small breach hole calculations, as is expected due to an increase in breach hole area. Due to this, the pressure inside the tube reaches 1 *bar* at 205 *s* for the large breach hole

calculations, while the same occurs at 560 s for the small breach hole calculations. Furthermore, the switch from choked to non-choked conditions is visible in figure 34 and figure 36 due to the mass flow rate decreasing from a constant value. In section 7.2.5 these calculations will be used and expanded by including the leak rate during the experiment. Furthermore, the pressure values and the experiment time will be compared to data obtained from measurements.

5.4.2 Shockwave prediction

In the previous section the predictions on the mass flow rate were discussed. In this section, predictions on the shockwave speed will be done. The shockwave speed is of importance, since it creates a requirement on the camera capture frequency, as will be explained in this section.

Before the tests are performed, predictions have to be made such that the test results can be analysed accordingly. In section 2.5.3 the equations and theory behind determining the pressure ratio over a shockwave were explained and these equations were used for this prediction. Based on the initial pressure difference of 100 kPa outside the tube and a 1.0 kPa pressure inside the tube, a pressure wave of 1.156 kPa reaches the pod as is calculated using equation 30[9]. Using the cross sectional area of the pod and the pressure wave, the force on the pod is $4N$, as was calculated using the following equation:

$$dF = dp \cdot A_{pod} = (1156 - 101.3) \cdot 38e^{-4} = 4.0N \tag{43}$$

To ensure the Hyperloop pod is not displaced by this force, the pod has to be mounted rigidly inside the tube. The method with which this is done is explained in further detail in section 6.3.3. The calculation of force on the pod was done for a breach hole diameter size of 13.16 mm, which is the smallest of the two breach holes. Furthermore, the pod position was assumed at 920 mm from the back side of the breach hole to the front of the scaled Hyperloop pod. These calculations are based on the test setup geometries. The area A_{pod} is the cross sectional area of the pod, which has an assumed blockage ratio of 60 %, resulting in $38e^{-4}$ m^2.

When the breach hole is opened, a shockwave is expected to occur, however in order to measure and determine the effects of the shockwave in the physical test, the speed at which it travels has to be determined. From this a suitable frames per second setting can be determined to be used for the camera. To determine the shockwave speed equation 24 is used, which was explained in section 2.5.3. For similar conditions as were used to determine the force on the pod and temperature of 288.15 K, a shockwave speed of 803 $\frac{m}{s}$ is expected. With a speed of sound of 343 $\frac{m}{s}$, this relates to a Mach number of 2.3. However, since this was estimated from a 1D approach of calculating shockwave properties, a shockwave speed of 803 $\frac{m}{s}$ is the theoretically highest possible value: due to 3D effects the actual shockwave speed will be lower, especially considering the shockwave originated in the breach hole and has to propagate through the tube to reach the pod. Furthermore, to capture a shockwave travelling at 803 $\frac{m}{s}$ on an image with a width of 100 mm, a minimum camera capture frequency of 8003 hz would be needed to ensure subsequent images not missing the shockwave. Such a high camera capture frequency which could require a small experiment duration, a large camera memory or a camera placed a significant distance from the tube, thus reducing image quality. For the sake of this research the goal is to get as close to these numbers as possible without negatively affecting the experimental setup in a practical sense.

6 Experimental Setup

In chapter 5 the optical modelling of the experiments was discussed based on the introduced Snell's law model, its application to Hyperloop breach testing and flow predictions. In this chapter, the focus is the test facility and the steps taken to prepare and execute the testing phase. First the initial BOS feasibility test will be discussed in section 6.1, in which the testing method itself is checked for feasibility. In section 6.2 the final test setup is discussed. The requirements on components, assembly and safety are discussed. Furthermore, settings used for the camera and pressure meter are provided. In section 6.3 the three final tests are explained. The camera settings and the reasoning for each test are detailed. Any changes between consecutive tests are explained.

Several testing phases were done, in which the earlier testing phases were used to determine the effectiveness of the techniques and procedures, while the last testing phase was used to obtain final data results. The PMMA tube was mounted to the vacuum chamber, after which the steel rings were clamped around the flange of the tube and bolts mounted to the vacuum chamber through the holes of the rings. The initial setup after the tube is mounted is shown in figure 38.

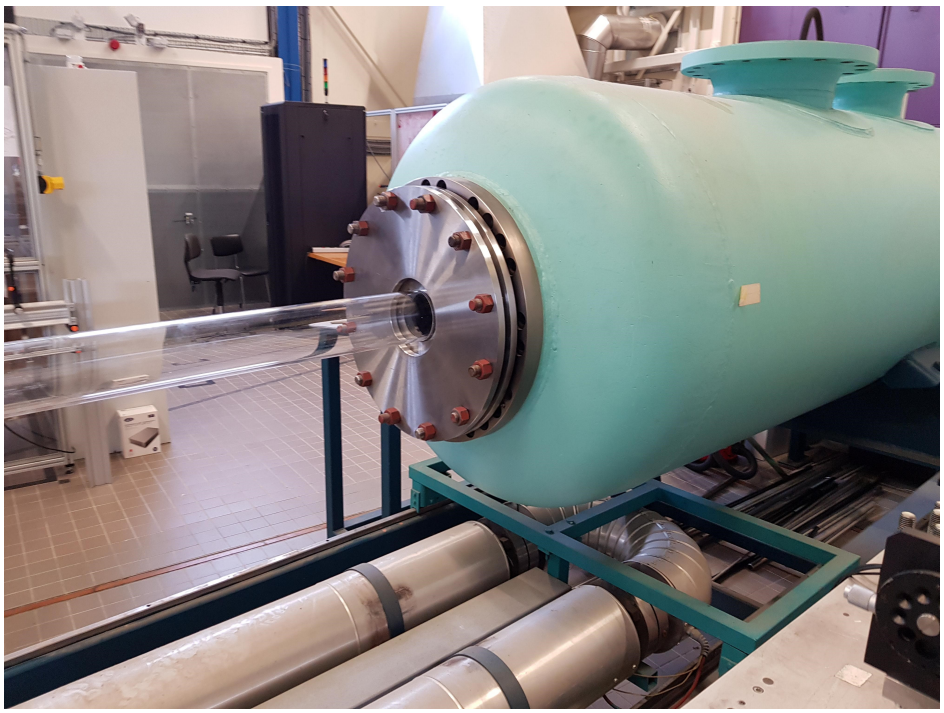

Figure 38: Initial Test Setup after tube was connected to the vacuum chamber

6.1 BOS feasibility test

Before measurement data can be obtained, first it has to be determined whether the testing method is suitable and effective for this research. To do this, initial tests were performed to confirm the

suitability of the testing location with respect to available time slots and personnel, the availability of measurement equipment, such as cameras and pressure meters, and the feasibility of PMMA as a tube material with respect to BOS measurements. Initial BOS tests were performed to determine the effect of circular tubes on light refraction and camera view from it. This way the full experiment, to be performed when connected to the vacuum chamber, can be emulated such that is determined if BOS is a sufficient way of measuring density changes in the tube. Firstly a list of used equipment and an image of the test setup will be shown. Secondly the tests will be described, such that the intend of the test equipment and the purpose of the tests are known. Lastly, each element of the test setup is described in detail, explaining design choices and initial parameter used.

A list of all used equipment is:

- Tube with 200 mm diameter and $4mm$ wall thickness
- Tube with 150 mm diameter and $5mm$ wall thickness
- Computer with correlation software installed
- Clamps, sliders and bolts used to assemble the test setup
- Scientific complementary metal–oxide–semiconductor(sCMOS) camera using a 60 mm f 1:2.8 D lens and a 35 mm f 1:2 D lens
- Variable intensity light source
- Speckle pattern sheet attached to cardboard frame
- Targeted heating device

An overview of the test setup is shown in figure 39.

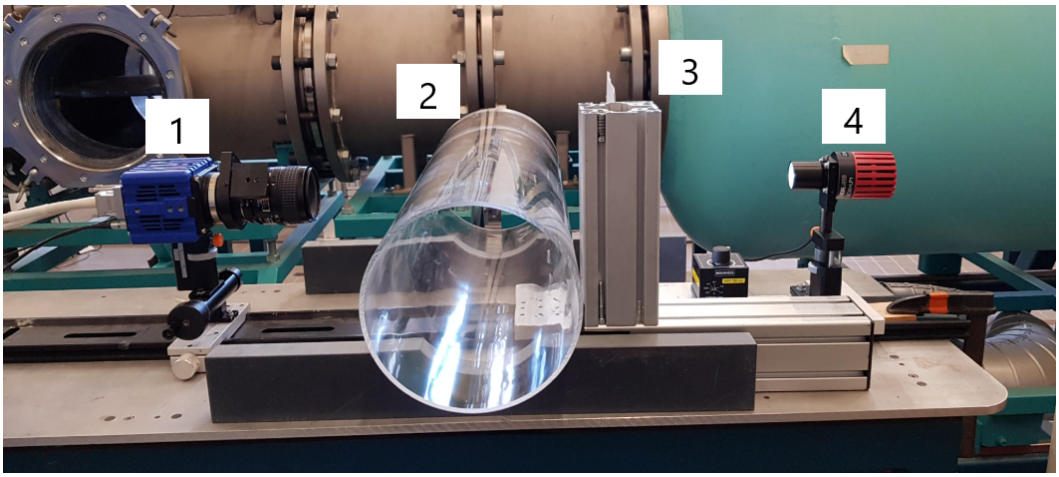

Figure 39: Test setup for background oriented schlieren test. 1. Camera, 2. Tube, 3. Speckle pattern, 4. Light source

With the test setup shown, the tests will be explained in order. First a measurement was done using only a camera and a background pattern. This is to test the resolution of the image. A reference image was created to be used by Davis, the software that translates background image distortion to pixel displacement. From this the software was tested by taking a second image while a targeted heating device is blowing between the camera and the background pattern. After these tests the tube was placed in the test setup as shown in figure 39. The same procedure as described before was used to obtain imagery, however the tube was placed between the camera and the background pattern. Not only will the reference image be different due to the refractive index of the tube material and the circular shape, but the targeted heating device also causes a change in refractive index due to a change in temperature and density. For these reasons the BOS setup can be tested to see the effect of both the distortion of air and the refraction due to tube material and geometry.

With the tests described, each element of the test setup will be described in detail. In the test an sCMOS camera is used. On this camera different lenses are able to be fitted and the Micro-Nikkor lens of 60 *mm* f 1:2.8 D and the Micro-Nikkor 35 *mm* f 1:2 D were used. For the camera several settings could be changed. The goal is to maximize the contrast of the image without over-saturating it. This is done by adjusting the diaphragm and the intensity of the light source. Furthermore the camera is focused to ensure sharp images are taken. The used camera is shown in figure 40. It was placed on rails such that it could be moved axially without severely interfering with the pointing angle of the camera.

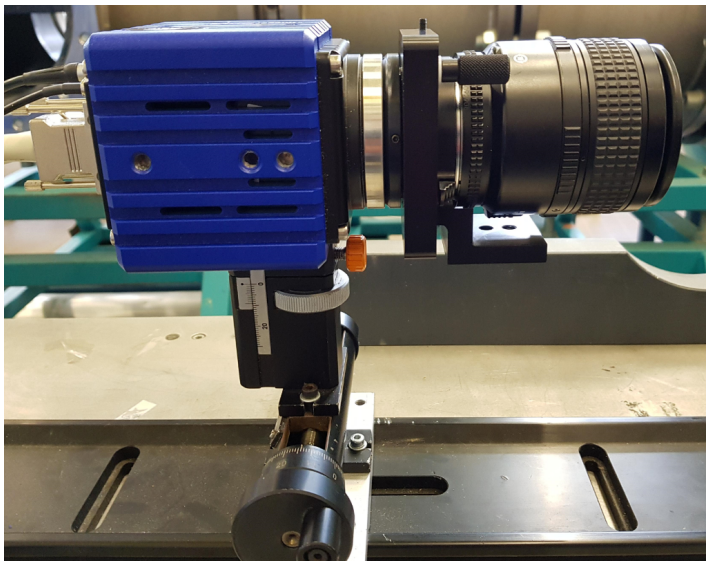

Figure 40: sCMOS camera used in background oriented schlieren test

The light source is shown in figure 41 and the light intensity of the source can be regulated. The light source has a white light spectrum. To determine the influence of the ambient light on the setup, a test was also done with the shutters down and the lights off. The difference between both cases was negligible due to the intensity of the light source being very high. Light spots were visible on

the tube, however upon inspection of the imaging on the computer no visible effects due to this were observed.

The 200 *mm* diameter and 4 *mm* wall thickness tube is shown in figure 42. Upon inspection the tubes showed significant imperfections and some scratches, which was remained after proper cleaning.

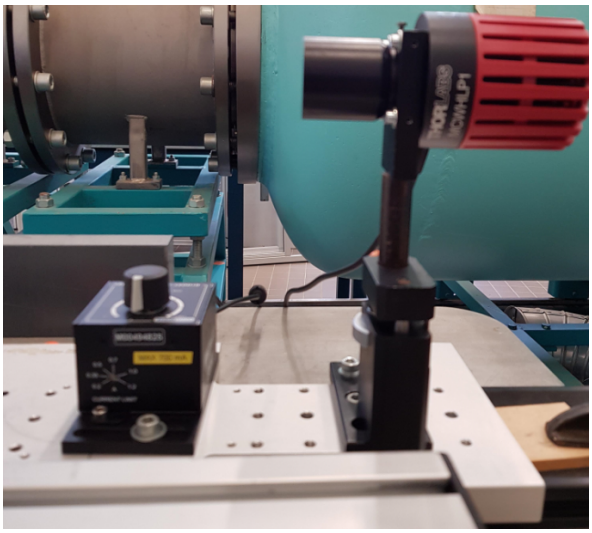

Figure 41: Light source used in background oriented schlieren test

Figure 42: Test tube used in background oriented schlieren test

The tubes were marked at the ends to ensure that for each image the same section of the tube was imaged. The reason for this is that the imperfections and scratches on the tube did affect the image quality: imperfections could be observed in the images, and when the tubes were turned the displacement of the imperfections was visible on the images.

To visualize any changes in density of the air inside the tube, a background pattern was used for BOS measurements as shown in figure 43. The background pattern was created using a MATLAB program to generate a suitable background pattern. In this program the resolution of the background pattern, the size of each speckle on the background pattern and the frequency of the speckles could be adjusted. The resolution of the pattern is important such that the image processing can detect accurate changes in speckle positions. Furthermore, the the frequency of speckles is important, since the image processing requires visible speckles in each are it is evaluation, the interrogation area. From experiments done by Raffel[27] and Cozzi[13] on background patterns in BOS a suitable particles per pixel value is 0.037 particles per pixel, which for the purpose of this research is viewed as the minimum required value for background patterns. In section 7.2 the final characteristics of the background pattern will be explained, along with the resulting images obtained from using the background pattern. The pattern is kept in place by a clamp attached to a pillar to ensure a sturdy setup that does not get moved by air blowing from the targeted heating device.

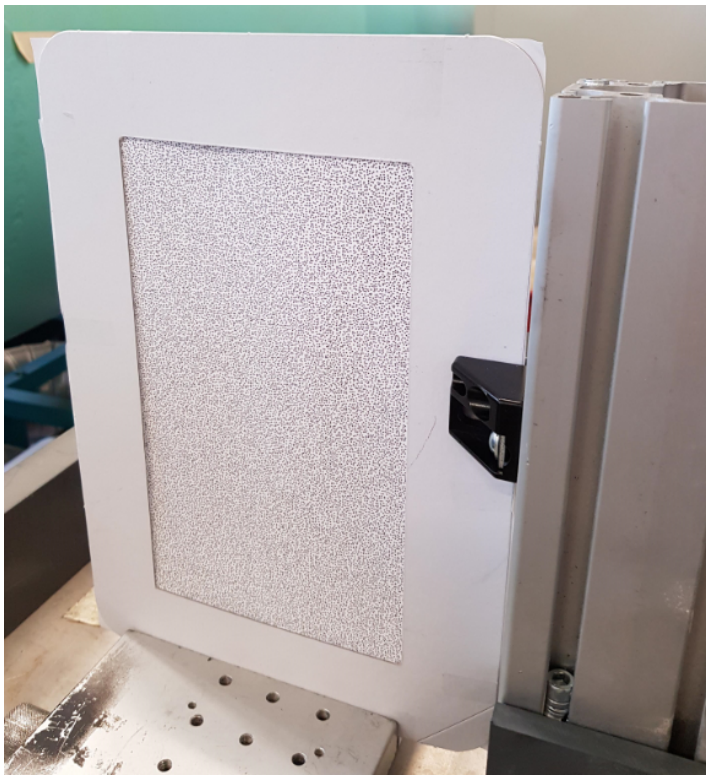

Figure 43: Background pattern used in background oriented schlieren test

The results from BOS feasiblity test are found in section 7.1, in which the feasibility of BOS, the conclusions on the background pattern and the test setup are discussed.

6.2 Final test setup

For the assembly of the final test setup, aluminum beams were used to create supports on which the tube's end was mounted. Without the support, the tube would freely hang from the vacuum chamber, creating a bending moment. The tube was clamped to the aluminum beam to restrict lateral movement of the tube, which could occur during testing. The support and tube end are shown in figure 44. Additionally, a metal tie wrap was wrapped around the tube and the beam support to prevent vertical movement of the tube.

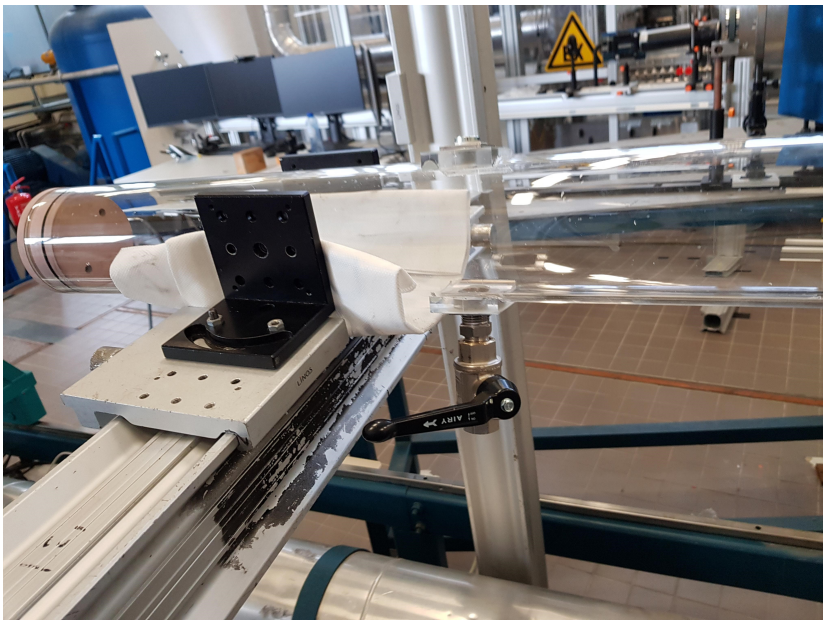

Figure 44: Supported tube end

An aluminum beam support was used to mount the camera, the light source and the background pattern, allowing for a rigid structure that is naturally aligned with. A LaVision 4MPix high speed camera is used for taking images of the background pattern. The camera can take pictures at 1102 frames per second at 4 MPix, however for this experiment the maximum resolution of the camera is not needed, allowing for an increased image frequency. This makes the camera ideal for the test setup, since images need to be taken in quick succession to record any changes in density and shockwave propagation inside the tube. The camera setup is shown in figure 45.

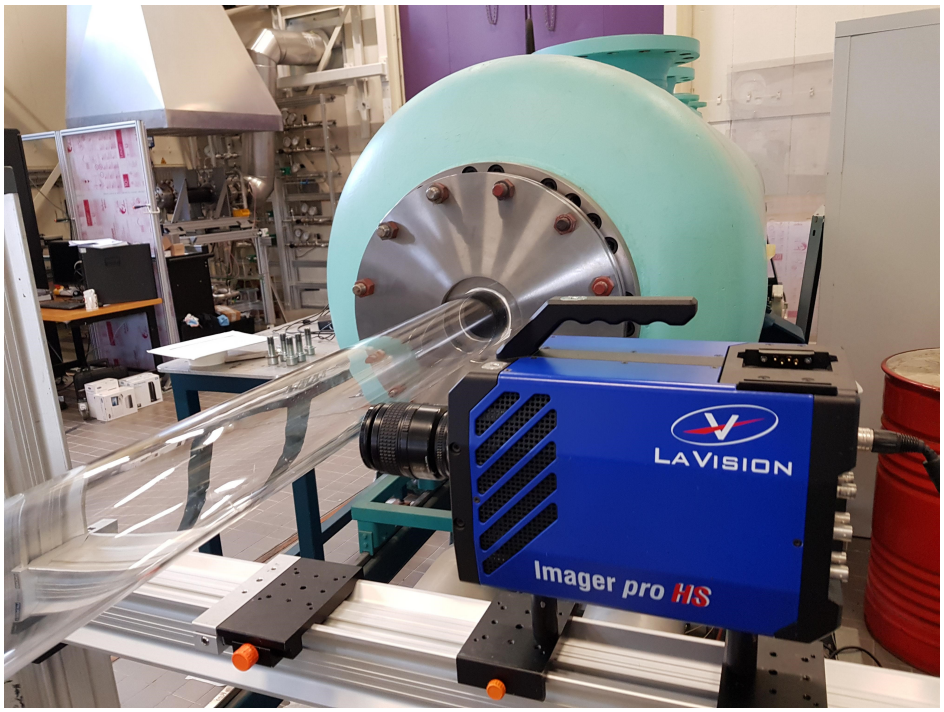

Figure 45: Camera position and support

On the opposite side of the tube with respect to the camera, the light source was mounted on the same support as the camera. A lens was mounted on the camera that would be suitable to small distances and focal length requirement for the measurements. After testing several options available at the HSL, the Micro-Nikkor 35f 1:2 D lens was chosen for the test setup. It has a minimal focusing distance of 25 cm, which is sufficient for the test setup used. The camera was aligned to the center of the tube, such that the center of images taken during the experiment is aligned with the center of the tube.

A pressure meter was installed into the tube. To provide a clear indication of the distances between each element of the test setup, the center of each breach hole is viewed as the origin from which each component is measured. The pressure meter is installed 600 mm from the center breach hole. This makes it far enough from the breach hole such that shockwaves originated from the breach hole have become perpendicular to the tube wall, as was explained on the design of the tube in section 3.1. The middle of the camera lens and the middle of the background pattern are both located 1060 mm from the breach hole, since these components are aligned with each other. An overview of the test setup is shown in figure 46.

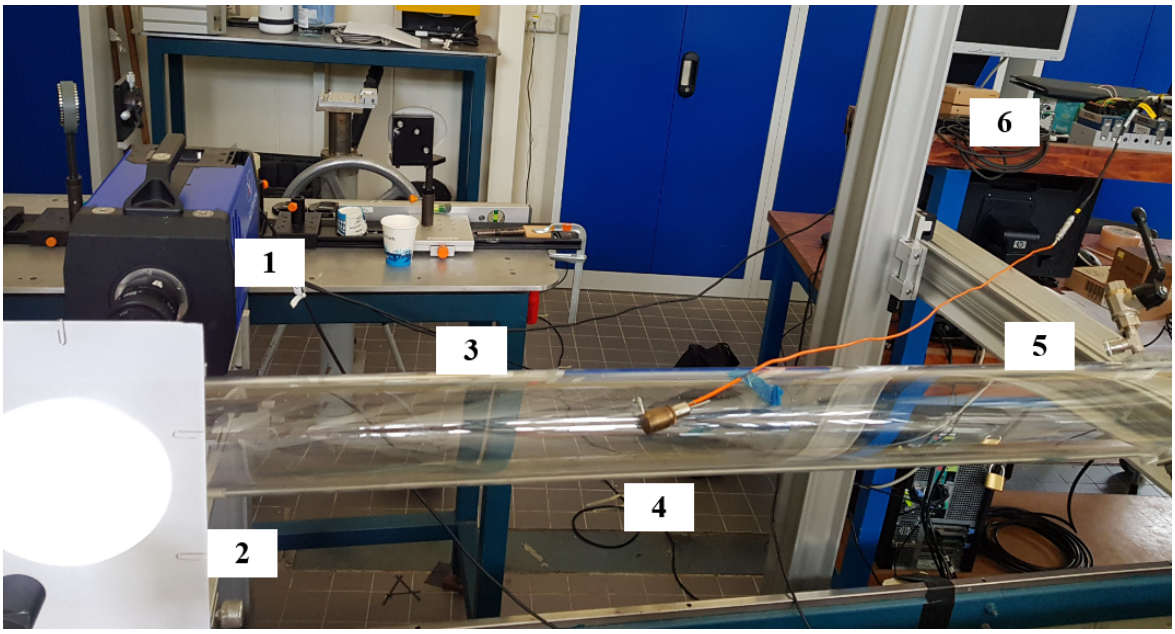

Figure 46: Test setup including 1. Camera, 2. Background pattern, 3. Hyperloop tube, 4. Pressure meter, 5. Breach hole opening device, 6. Measurement data signal collector

A tool was created using Labview in which the installed pressure meter, the pressure reading from the vacuum chamber and the camera are connected, as was discussed in section 4.2 regarding timing and synchronization of measurement techniques. In figure 46 the physical connection of these measurements is represented by number 6, the measurement data signal collector. The tube pressure meter uses a voltage level that is stored by the labview program. Initially a calibration file was obtained from other research projects using labview to transform the voltage level into pressures, however the results were inaccurate. Instead the calibration was done using ambient pressure, the 10 *mbar* starting test pressure and using the voltage change rate to determine the pressure value at any point in time. This method provided more accurate results and the voltage change rate was used through all experiments.

6.3 Tests and measurements

While in the previous section the final test setup was described, in this section the different tests are described, which will be explained in each respective section. Since the tube has two breach holes with different sizes, test can be performed for similar conditions while comparing the effect of the breach hole size. While under ideal circumstances the hole size is variable such that a larger sample data size can be obtained to find a correlation between hole size and flow propagation through the tube, doing so in a controlled physical test setup is beyond the scope of the research.
The procedure of performing each test is as follows:

1. The camera is installed and the background pattern is placed.

2. The image sharpness is checked on the computer connected to the camera.
3. The breach holes are closed and the vacuum chamber suction is started.
4. The vacuum chamber suction is stopped at the desired internal pressure of 10 *mbar*. The internal pressure is read off from the suction device and documented.
5. The labview program is started
6. The camera recording is started.
7. The breach hole required for the test is opened.
8. The test is stopped when the required camera capture time is passed or the inside pressure is equal to ambient pressure

The choice is made to perform three different tests to test each different aspect of the test procedure, the test equipment and the test conditions. The first test spans the full pressure range to provide the upper and lower limit on pixel displacements in the test. The data from this test is used in combination with the Snell's law model to provide a full range of pixel displacements across the full pressure range. The second test attempts to detect a shockwave in the test section. A high camera recording frequency will be required for this, since the shockwave is expected to move at high speed. The third test is used to study the interaction of the Hyperloop pod inside the tube due to Hyperloop breach.

6.3.1 Test 1: Full pressure range test

The first test is a low frames per second(fps) test in which the whole pressure range from a closed tube, to an opened breach hole tube, to ambient pressure is registered. To account for memory of the camera and limit on fps, the resolution is reduced to the center of the background pattern. Several different resolutions were manually tested to determine the associated file size, resulting in a final resolution of 624×1412 pixels for this test, since this resolution allows for an experiment time of at least 600 s, the maximum expected experiment time as determined in section 5.4.1. A frames per second value of 5 is chosen for this test, since it provides a sufficient test length to attain ambient pressure in the tube while ensuring the camera internal memory limit is not exceeded. The goal of this test is to determine the pixel displacements across the whole pressure range and comparing this to the ray tracing Snell's law model described in section 5.1.

6.3.2 Test 2: Shockwave detection test

The second test is a high frames per second test to visualise initial breach hole shockwave effects. In this test the camera is set to 7500 frames per second. While a higher frequency is preferred, doing so would decrease the image resolution due to the limit on the internal camera memory. Since the expected maximum shockwave speed is 803 $\frac{m}{s}$ as was determined in section 5.4.2, the width of the image has to be big enough to ensure at least one shockwave is captured. A resolution of 960×568 was used: the height of the image is reduced in favor of width. As was explained in section 4.3, the constraints of the camera have to managed: the limit on the camera internal memory poses a trade-off between image resolution, experiment time and camera distance. While moving the

camera backwards could increase the field of view, this also reduces the amount background pattern speckles per image pixel, thus impacting the performance of correlation operations. Since for this test an accurate detection of a shockwave is required, the image resolution was reduced. Since a new resolution is used, a new pixel distance measurement was performed, in which the distance between speckles is measured using a centimeter grid paper at the same location as the speckle pattern sheet. The test is performed for both the small and the large breach hole.

6.3.3 Test 3: Hyperloop pod test

The third test is a Hyperloop pod test: for this test a scaled Hyperloop pod is placed inside the tube. The pod is placed such that background pattern is visible around the front and top part of the Hyperloop pod. This way, the pixel displacements can be measured around the leading edge of a Hyperloop pod.

A cord is attached to the pod and connected to the tube near the closing handle. This way, the pod is not able to fly into the vacuum chamber as a safety measure and the pod could be taken out after the test by pulling on the cord. The test is done at 2000 frames per second. This is a lower frames per second compared to test 2, since a larger area is required for viewing the entire front end of the tube, resulting in a resolution of 1248×1252. A large part of this increase in resolution is due to an increase in width of the resolution, such that the image is sufficiently wide to detect the initial shockwave based on its speed. The other part of the resolution change is in the height however, as is necessary to view the full height of the pod.

Instead of the changing the resolution, the camera could be moved backwards or a different lens could be used, however the current lens used(35mm) was the smallest one available at the HSL that also can be mounted on the camera. Furthermore, the camera was already moved close to the edge of the aluminium beam support hosting both the camera and the light source, thus moving it further back would require either moving it from the support and losing the natural alignment with the light source, or a larger support, which was not available at the time. The pod itself was kept in place using magnets attached to both the underside of the pod and magnets outside the tube.

The settings used in each different test are shown in table 2.

	Resolution	Frames per second
Test 1	624×1412	5
Test 2	960×568	7500
Test 3	1248×1252	2000

Table 2: Settings specific to each test

7 Results

In chapter 6 the test setup and the different tests were described. In this chapter the results from those tests will be discussed. The BOS feasibility test results are discussed in section 7.1. Results for this test will show the feasibility of BOS for Hyperloop breach research and whether it can be used for further testing. In section 7.2 the results of the first test are described using correlation images at different time points during the test. From these correlation images pixel displacements will be determined. The Snell's law model as described in section 5.1 is used to translate pixel displacements from measurements to pressures. In section 7.3 the results of test 2 are discussed using the same method as used for the first test. The focus of this test is determining the impact, location and consequences of a shockwave caused by Hyperloop breach. In section 7.4 the results of test 3 are discussed. The focus of this test is a scaled Hyperloop pod placed inside the tube. The results will focus on the interaction of possible shockwaves and air flow as a results of Hyperloop breach with the Hyperloop pod.

7.1 BOS feasibility test results

The results of the BOS feasibility test were analyzed to determine if the method of using pixel displacements from images using the BOS feasibility test setup proved sufficient measurement sensitivity in order to obtain meaningful results. To determine the effect of the presence of a tube, which is expected to affect the path of light rays as observed by the camera, its images are shown in figures 47 and 48. The image in which a tube is present is distorted and the correlation image displacements in the distorted areas of the image are larger then 1 *mm*. The large distortion is a result of the imperfections in the tube structure: upon inspection scratches and roughness were present in the tube wall.

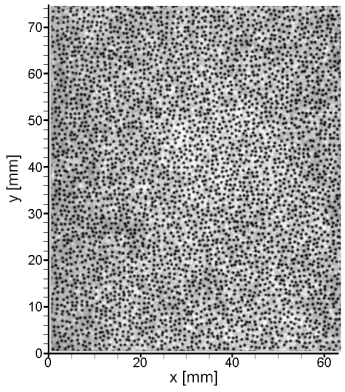

Figure 47: Background pattern of the image without a tube present

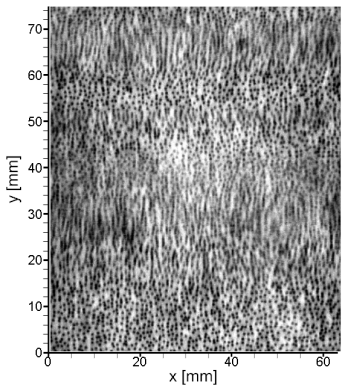

Figure 48: Background pattern of the image with a tube present

The images of a test in which a targeted heating device is blowing through the tube compared to a picture in which only a tube is present are shown in figures 49 and 50. The camera taking the images is aligned with the center of the tube and the background pattern. The correlation image of these images is shown in figure 51.

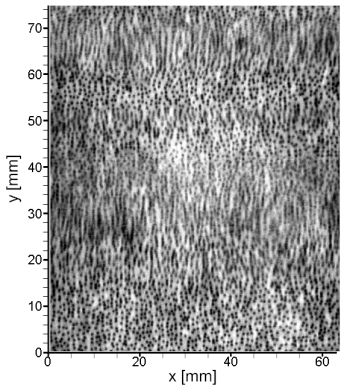

Figure 49: Background pattern of the image without a targeted heating device blowing

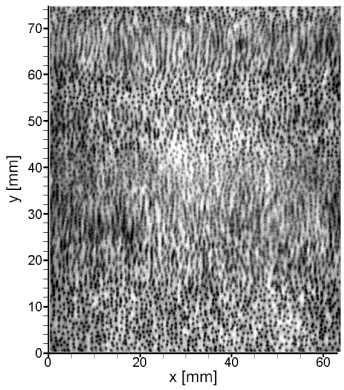

Figure 50: Background pattern of the image with a targeted heating device blowing

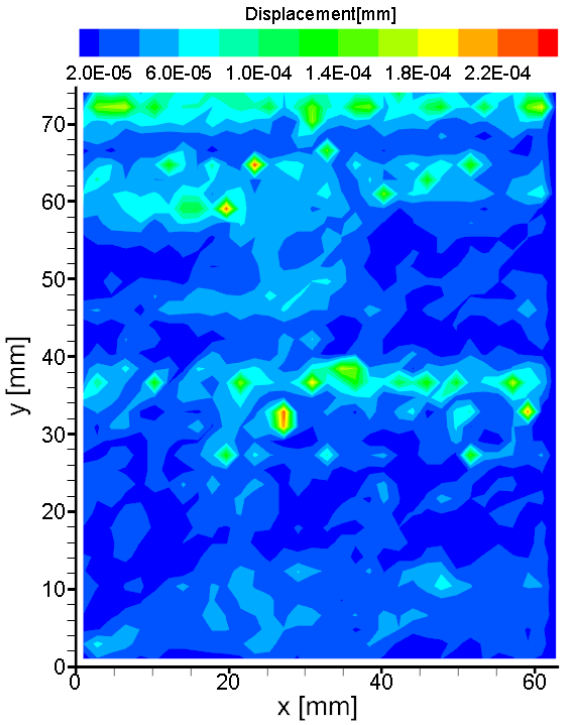

Figure 51: Correlation image of the test in which a targeted heating device is blowing through the tube

The correlation image shows increased pixel displacements in the center horizontal area of the image. This is the region in which the targeted heating device was blowing. However, due to the

imperfections in the tube several other increased pixel displacements areas in the image are also visible. Thus for the vacuum chamber test the tube has to be of higher quality to be able to draw clear conclusions from the pixel displacements in the images. While these results are not conclusive to the sensitivity of BOS for Hyperloop breach test setup, it was sufficient to continue improving the testing method and continue using BOS.

Further conclusions could be drawn from this test with respect to camera, hardware and software settings:

- Several different lenses and cameras were tested as was mentioned in section 6.2, of which the Micro-Nikkor 35f 1:2 D was found sufficient for this application and will be used further in the Hyperloop breach tests. It allows for camera movement away from the tube if needed while still providing sharp images.
- Precise alignment of the background pattern and the camera is vital, since initial testing showed that movement of the background pattern results in large displacements in the correlation images. Mounting both the background pattern and the camera on the same rigid aluminium beam ensures proper alignment.
- In this research multiple different settings were experimented with to determine the most effective in terms of accuracy and time investment with respect to the correlation operations. Single-pass and multi-pass settings were tested, to determine whether an expansive single-pass method or multiple coarse pass are more beneficial, of which the theory was discussed in section 4.3. For Hyperloop breach testing a single pass vector calculation is used, in which a pass window size of 64×64 is used. A larger window size made it difficult to distinguish local displacements, while course multi-pass operations did not improve the ability to distinguish local displacements. For the main tests, of which the results will be described starting from section 7.2, the pass window size is decreased to 32×32 to ensure the ability to record accurate local displacements. Furthermore, the pass window overlap was set to 0%, which means there is no overlap between each window. The reason for this is that due to the great amount of images taken during the tests, the time required for the operations is large and using a pass window overlap would increase the operations time further.
- The requirements on the background pattern, as were described in section 6.1 in which a minimum particles per pixel value of 0.037 was outlined, were tested to check if enough speckles were visible in the images and if the correlation operation could use the speckles to properly detect pixel displacements. The used background pattern has a particles per pixel value of 0.072, thus this is sufficient. Pixel displacements could be detected, however the distortion caused by the imperfections of the test tube influenced the results.

7.2 Test 1: Full pressure range test results

While in the previous section the feasibility of BOS was discussed for Hyperloop breach testing, in this section the results of the first test as described in section 6.3.1 are discussed. Before focusing on the image results, the method of obtaining results is outlined.

1. Images are taken during the entire length of the experiment, for this test at a frequency of 5 frames per second.

2. The first image of the set is used as a reference image, for which the correlation software will correlate all other image of the set with. The first image was taken before the breach hole was opened.

3. Each window size of the correlation operation will calculate the displacement between its current image and the reference image, saving its displacement value as well as its location. This process was explained in detail in section 4.3, in which the guidelines for determining the window size were given and the cross correlation process was explained. The window size is supplied by the user, which for this test is 32×32 pixels, resulting in 18 windows in the x-direction and 43 windows in the y-direction for a total of 774 windows of displacement values given the image resolution of 624×1412 pixels. A visualisation of image subdivision into windows was shown in figure 27 in section 4.3.

4. From the Snell's law model a data set was created of three values: location, displacement and pressure inside the tube. By using the displacement value and the location obtained from the correlation operation of the background images taken during the experiment, the Snell's law model provides the corresponding pressure inside the tube corresponding to the window. To provide a value to the pressure for the entire image, the mean of the displacements at the center of the image is taken, which for this test is the mean of the values of the 43 windows in y-direction at the at the 10th window in x-direction. A graphical indication of this will be discussed and shown in figure 56.

5. Each image now has a corresponding pressure inside the tube from its displacements and the pressures are plotted over the entire experiment time.

6. Additional operations are performed to improve the data set results using smoothing operations and error source elimination and mitigation.

With the method of obtaining results outlined, the described steps will be performed in sequence, starting with results from the larger breach hole with a diameter of 20.96 *mm*.

The first and last background pattern images of the larger breach hole test are shown in figures 52 and 53. The images were taken 5 minutes and 43 seconds apart. The first image was taken before the breach hole was opened at a pressure of 10.3 *mbar* and the second image at the end of the experiment at an ambient pressure of 1025 *mbar*.

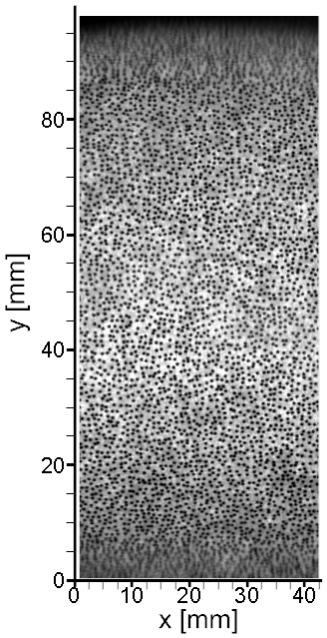

Figure 52: Background pattern of the first image using the larger, 20.96 *mm* diameter breach hole

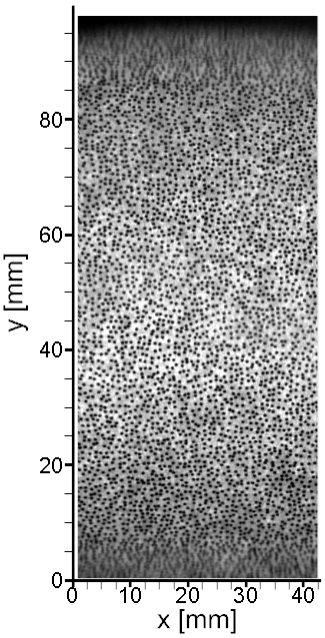

Figure 53: Background pattern of the last image using the larger, 20.96 *mm* diameter breach hole

A visual inspection of the images gives little information on the local displacements. To properly determine the difference, a correlation is performed using Davis software. The correlation shows the displacement of pixels between the images. The magnitude of the displacement at each window will be used, such that the orientation of the displacement does not determine its size and the values will always be positive, as given by:

$$d_t = \sqrt{dx^2 + dy^2} \tag{44}$$

In this equation d_t is the total displacements, dx the displacement in x-direction and dy the displacement in y-direction. The color scheme represents the displacement values shown in figure 54. The result shows a greater displacement in the north and south region of the image. The displacement decreases towards a location of $y = 70$ *mm*, which is above the center of the image. The Snell's law model expects the lowest displacement in the center of the image, since the curvature of the tube causes increased displacements away from the center. As seen in this image, the total displacements of windows to the left and right of the center of the image also increase away from the center. The reason for this is that light rays pass through the tube at an angle, even though this is not caused by the tube curvature, which the Snell's law model does not account for.

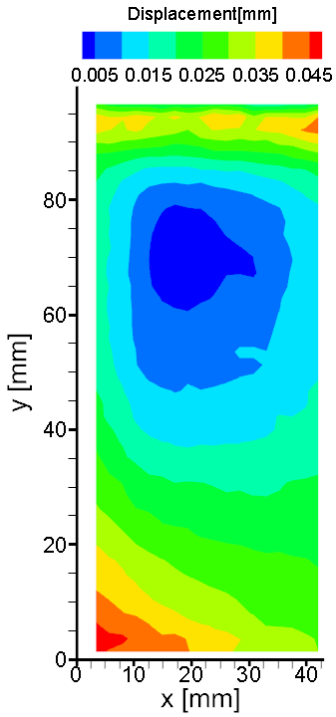

Figure 54: Correlation of the first and last background pattern images of the larger, 20.96 *mm* diameter breach hole test

Before determining the pressure value associated with each displacement image, first the pressures measured during the experiment from the tube pressure meter and the tank pressure meter are plotted. These pressures measured from the pressure meters during the experiment are shown in figure 55.

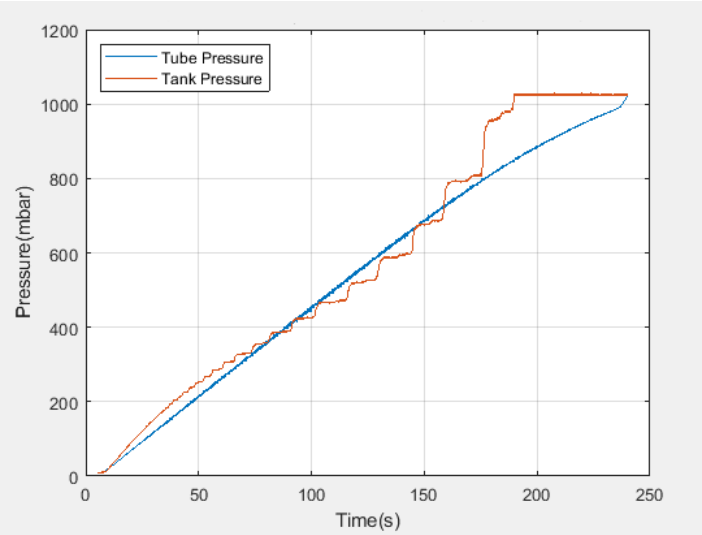

Figure 55: Pressures as measured by the pressure meter in the tube and in the vacuum tank for the larger, 20.96 *mm* diameter breach hole test

While the tube pressure shows a gradual increase with time, the tank pressure shows jumps in pressures. After running multiple similar tests, the tank pressure readings showed similar trends, therefore the jumps are a result of the tank pressure measuring equipment and the way in which it transfers its readings to the computer.

By correlating the images of the background pattern, pixel displacement plots are made like the image shown in figure 54. The settings for the correlation analysis are a single pass vector calculation with a pass window size of 32×32. Furthermore, the pass window overlap is set to 0%. This way the resulting correlation images show local displacements while the total operation time is limited to several hours. To determine what pressure each correlation image equates to, the mean displacement of the middle vertical windows are calculated. An image what is meant by this is shown in figure 56, in which the red column represent the 43 windows used to calculate the mean displacement.

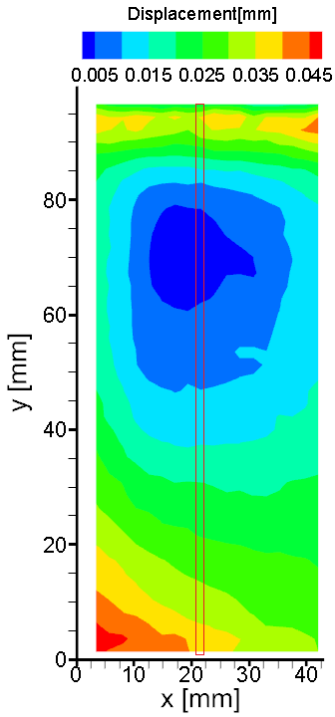

Figure 56: The red column corresponds to the set of 43 windows used to determine the mean displacement for the larger, 20.96 *mm* diameter breach hole test

By taking the mean of a set of displacements, images that have a minimum displacement that is not perfectly in the center have this offset mitigated. The mean displacements for each correlation image in the experiment are shown in figure 57.

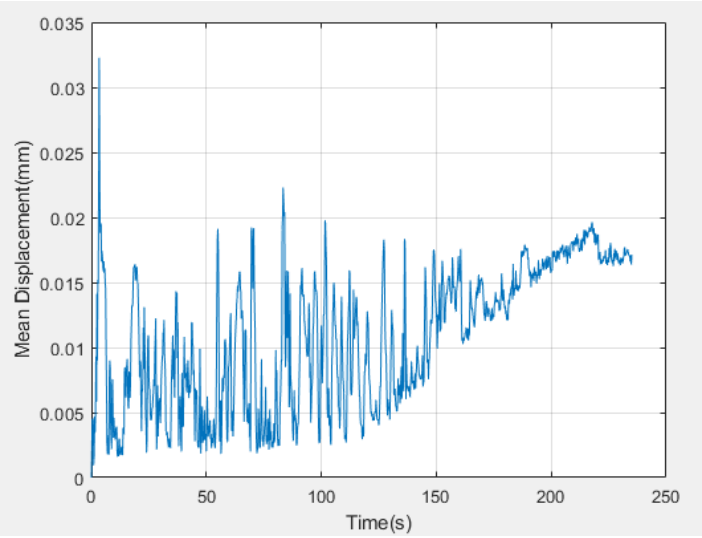

Figure 57: Mean displacements of the correlation windows for the larger, 20.96 *mm* diameter breach hole test

The Snell's law model is used to find the corresponding pressure values for the mean displacements. The pressures values as obtained from the Snell's law model are plotted in figure 58.

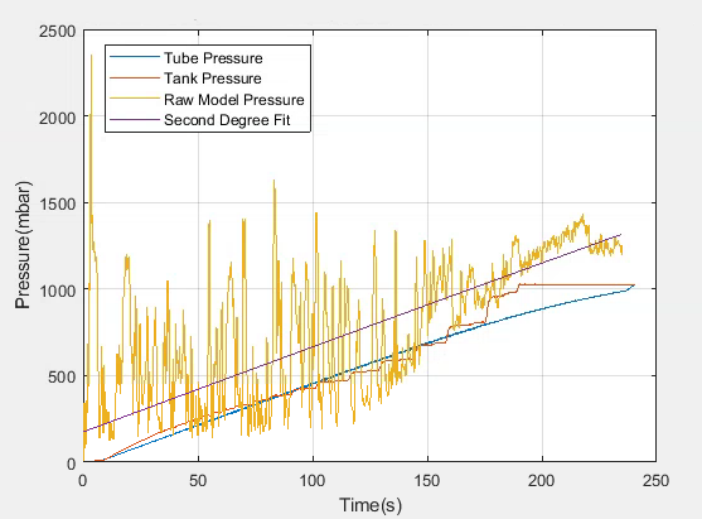

Figure 58: Pressures as measured by the pressure meter in the tube and in the vacuum tank for the larger, 20.96 *mm* diameter breach hole test combined with mean displacement correlation using the Snell's law model and a second degree fit of the Snell's law model data

Since the plot has several jumps across the entire time span, a second degree fit is made with the

limiting factor that it passes through the first pressure value at a time of 0.2 s. While the second degree fit shows a similar pressure increase compared to the measured pressure values, an offset still exists. This offset and the jumps in the pressure plot are investigated in the next section.

7.2.1 Identifying pressure plot jumps

To determine the cause of the jumps in the displacement and pressure plots, the individual images are investigated. The highest jump occurs at 3.4 s at a pressure value of 2353 $mbar$. Its corresponding correlation image is shown in figure 59.

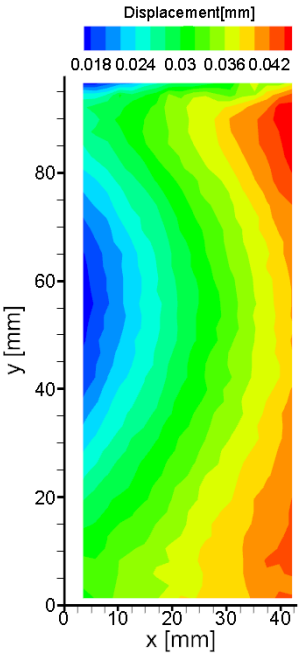

Figure 59: Correlation image taken at 3.4 seconds for the larger, 20.96 mm diameter breach hole test

The image shows the lowest displacement is not in the center: for this reason, the mean displacement through the center is much higher compared to images that do have the lowest displacement in the center. Since the Snell's law model relies on the expectation of a zero displacement through the center and increasing when moving away from the center, this could be the cause of the pressure jumps. To obtain the cause of the displacement distribution shown in figure 59, the same image is plotted using only the displacement in the y-direction in figure 60. The displacement distribution in strictly the y-direction does follow the expected pattern of highest displacements furthest from the center of the images, therefore the disturbance originates from displacements in the x-direction. This makes it likely for the disturbance to be caused not by the change in pressure inside the tube, but instead by an outside interference, such as vibrations caused by the manual opening of the breach hole or the are rushing into the tube.

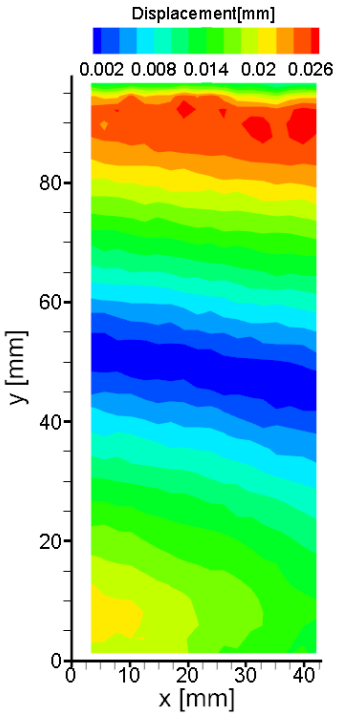

Figure 60: Correlation image taken at 3.4 seconds for the larger, 20.96 *mm* diameter breach hole test for only the displacement in y-direction

To determine the cause of the second degree fit pressure difference compared to the measured pressure in the tube and the tank, images before the breach hole is opened are analyzed. In figure 61 an image is shown at a time of 1.4 *s*. While the centering is much better compared to figure 59, this image has a non zero displacement in the center, while the Snell's law predicts a displacement of zero at that location. The cause for this displacement could be an outside interference, for example vibrations in the test setup. Using the Snell's law model to determine the pressure from this image results in a pressure of 352.1 *mbar*. Since the expected pressure at this time is approximately 10 *mbar*, this increase in pressure compared to the measured tube and tank pressure explains the offset of the second degree fit plot.

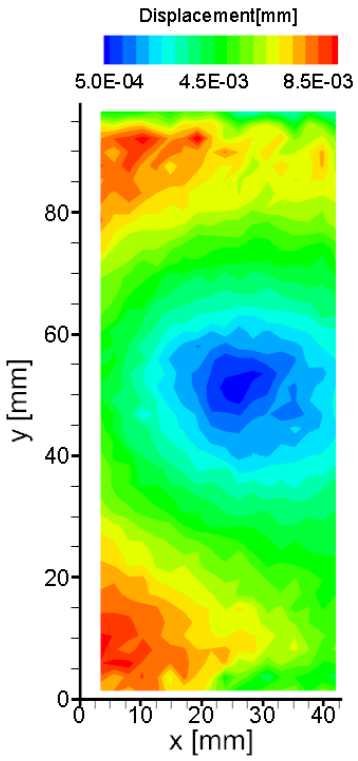

Figure 61: Correlation image taken at 1.4 seconds for the larger breach hole test

To account for this difference in pressure, the mean displacement of the second correlation image is subtracted from all mean displacements of subsequent images. The subtracted value is 0.0023 *mm*, which is the image displacement error. This error will be discussed in further detail in section 7.2.4. The resulting corrected data points and corrected second degree fit are shown in figure 62.

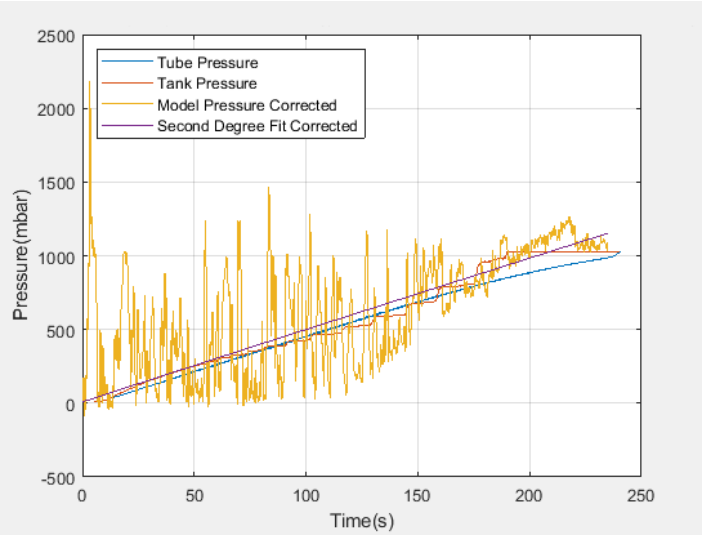

Figure 62: Pressures as measured by the pressure meter in the tube and in the vacuum tank for the larger breach hole test combined with corrected mean displacement correlation using the Snell's law model and a corrected second degree fit of the Snell's law model data

While there are several pressure jumps in the corrected model pressure data, the fit shows an upward trending line ending at a pressure higher than ambient pressure. The data points have a final point at 1089 *mbar*, thus also slightly higher than ambient pressure.

7.2.2 Analysis of displacements in y-direction

As was shown in equation 44, the total displacement is used to determine the associated pressures from the Snell's law model. To determine the effect of only using the displacements in y-direction for this analysis, its result are plotted against the results using displacements in all directions in figure 63

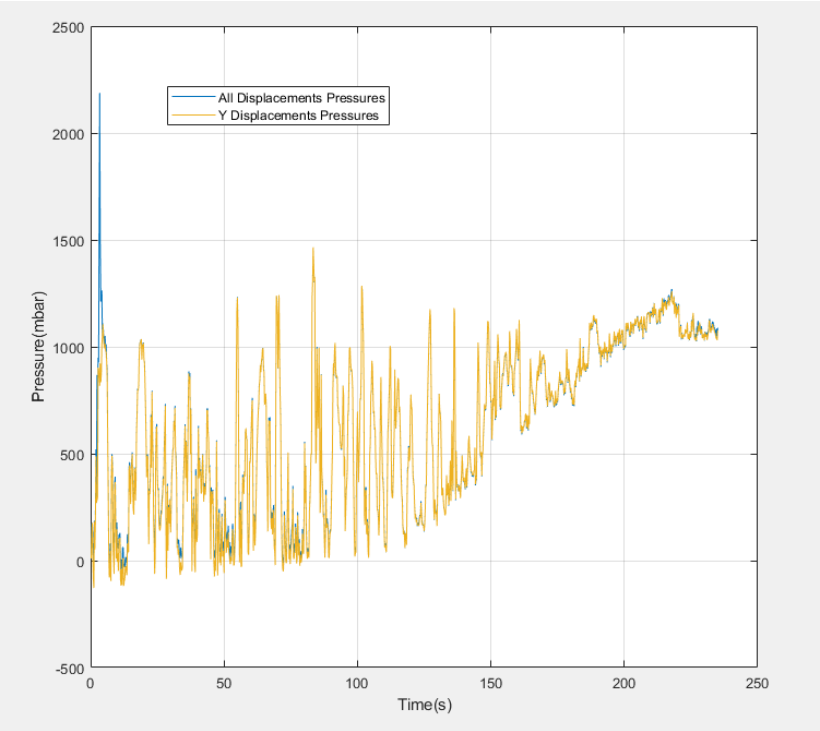

Figure 63: Pressure values for using displacements in y-direction versus pressure values for using displacements in all directions

The large jump in pressure at the start of the experiment is not present when using only displacements in y-direction. This indicates that the pressure jump is a result of a displacement in x-direction, caused by an outside source not related to the pressure inside the tube. The pressures during the rest of the experiment are near equal for plots in figure 63 however, thus the other jumps in pressure cannot be explained by unexpected displacements in x-direction.

7.2.3 Averaging displacements over x

To further investigate a method of obtaining results that have reduced jumps of pressure, averaging the displacements in y-direction over the x-axis could provide a solution. From figure 60 it was found that displacement in only the y-direction are as expected from the Snell's law model: the lowest displacements are in the middle of the image in y-direction and the displacement increase moving away from the middle in y-direction. Therefore taking the mean displacement of all displacements in y-direction across the whole image width makes it so the lowest displacements does not need to be in the center of the image: as was discussed in section 5.1, the Snell's law ray tracing model expects the lowest displacement to be in the center of the image, since light rays going through the center do not enter the tube under an angle, their path is not influenced by pressure differences inside the tube. By making it so the lowest displacement is not required to be in the center for the correlation images, the averaging over x makes it so any disturbances causing the lowest displacement position

to be off center have their influence on the pressure jumps less severe. For this analysis corrections or second degree fits are not used, in an attempt to purely focus on the effect of the averaging over x operation. In figure 64 both the pressure values with and without averaging over the entire range of x are plotted against each other.

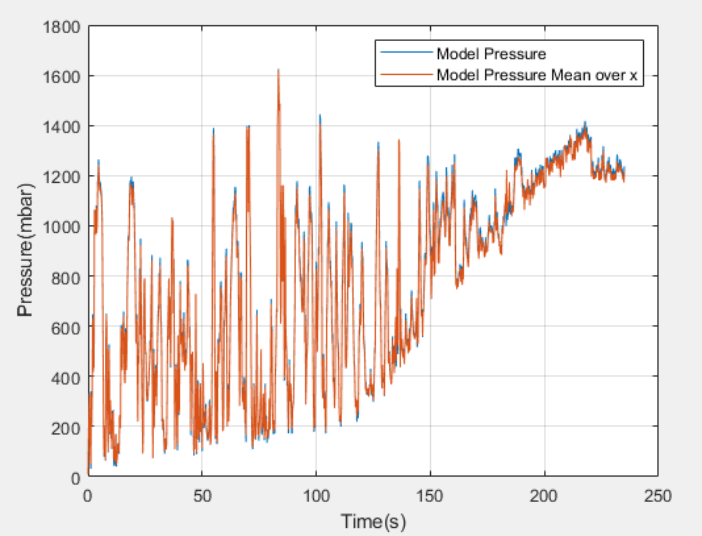

Figure 64: Pressure values using average y-displacements across the entire x-direction versus pressure values using y-displacement only in the center of the image

From figure 64 it becomes clear that the averaging over x only has a small effect: it shifts the graph downward slightly. To provide a clear view of this, a zoomed in part of the figure of the end of the experiment time is shown in figure 65.

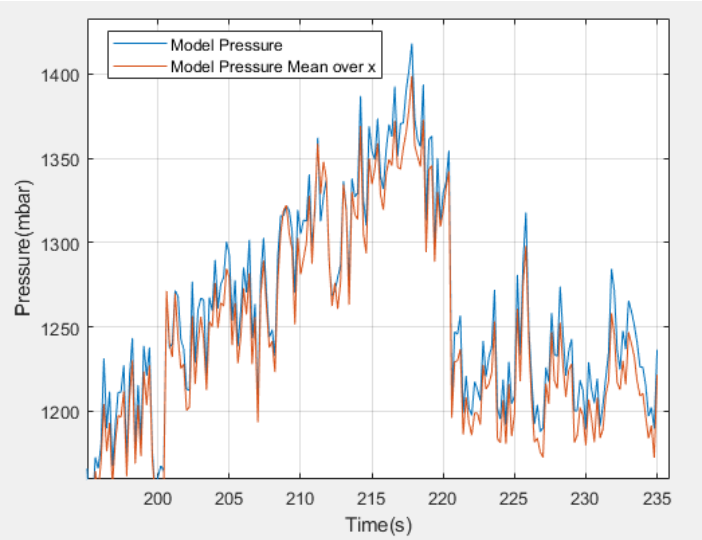

Figure 65: Pressure values using average y-displacements across the entire x-direction versus pressure values using y-displacement only in the center of the image, zoomed in on the end of the experiment time

It can be concluded that averaging the y-displacements across the entire x-direction does not improve the pressure jumps across the experiment time, but only reduces the pressure values by on average 20 *mbar* compared to only using y-displacements.

7.2.4 Standard deviation and error sources

To determine the variation and validity of the data and results, the standard deviation and error sources are analyzed. The standard deviation is a measure of the spread of data points and is determined by using the mean displacements from the last ten correlation images from the performed test. In these images, the pressure inside the tube has reached ambient pressure, therefore air has stopped flowing into the tube, thus the pressure and mean displacements are expected to remain constant. First the mean of the data points μ_m is calculated by using the mean displacement of each correlation image as the data points, resulting in a value of 0.0170 *mm*. The deviation is obtained by subtracting μ_m from the data points, with the results shown in table 3. The variance σ^2 is obtained by taking the mean of the squared deviations, resulting in a value of $1.03e^{-7}$ mm^2. Finally, the standard deviation σ is obtained by taking the square root of the variance, resulting in a value of $3.21e^{-4}$ *mm*.

Image number	Mean displacement	Deviation
1167	0.0175 mm	$4.95e^{-4}$ mm
1168	0.0173 mm	$3.12e^{-4}$ mm
1169	0.0172 mm	$1.63e^{-4}$ mm
1170	0.0171 mm	$6.38e^{-5}$ mm
1171	0.0170 mm	$-1.32e^{-5}$ mm
1172	0.0170 mm	$-6.86e^{-5}$ mm
1173	0.0166 mm	$-4.34e^{-4}$ mm
1174	0.0171 mm	$4.76e^{-5}$ mm
1175	0.0164 mm	$-6.72e^{-4}$ mm
1176	0.0171 mm	$1.06e^{-4}$ mm

Table 3: Standard deviation for the last ten correlation images of the full pressure range test. The mean μ_m of the data points is 0.0170 mm, the variance σ^2 is $1.03e^{-7}$ mm^2 and the standard deviation σ is $3.21e^{-4}$ mm

To determine the measurement accuracy of the measurements, the standard deviation can be used as an indicator. The data points of the ten correlation images all fall within two standard deviations of the mean of the data points, showing a low data spread. While for these data points this is true, it was observed that significant pressure jumps occur across the experiment. Thus, while the data point spread is low for the end of the experiment in which the pressure is expected to be constant and ambient, other error sources could have caused the pressure jumps as observed.

The accuracy of the correlation software itself can be determined by using the first correlation image. The first correlation image is a correlation with itself, which therefore can be used to check the software error related to correlation. The first correlation image is shown in figure 66 and its error is $2e^{-8}$ mm. Since this error is much lower than the measured displacements, the effect of this error will be irrelevant to the measured results.

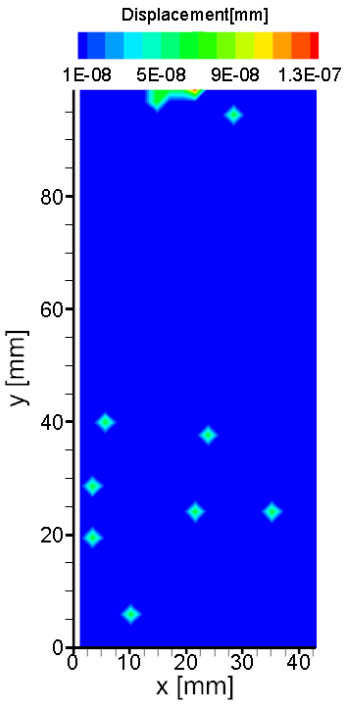

Figure 66: First Correlation image for the larger breach hole test

As was discussed in section 7.2.1, a minimal measurable displacement appears to exist. Whereas low pixel displacements are expected near the start of the experiment in which a 10 *mbar* pressure inside the tube exists, a mean displacement of 0.0023 *mm* was measured, which is substantial: a subtraction of 0.0023 *mm* from the mean displacements equals to 200 *mbar* when converted to pressure values. Since that equals 20% of the total pressure range of the test, this is a large error value. While correcting for this shows results that are in line with pressure meter measurements, mitigating errors in the test setup itself would provide more confident results.

Due to the operations aimed at mitigating the pressure jumps, the jumps are likely caused by errors related to the way the experiment is performed. A cause of the jumps in pressure could be vibrations in the tube. Since the tests are started by manually opening a pneumatic handle connected to the tube, movement of the tube is possible due to its length, even though it was clamped on both edges. Furthermore, the air rushing into the tube could lead to small vibrations in the tube. The vacuum tank itself could also be a cause of vibrations, since the tube is clamped to the vacuum tank using bolts. The fact that very small displacements the size of $2.3e^{-3}$ *mm* have large effects on the expected pressure inside the tube underlines the sensitivity of measurements in this experiment. Further steps to mitigate these errors using data operations are discussed in chapter 9, however ultimately these errors should be mitigated in the test setup.

7.2.5 Mass flow rate and leak rate

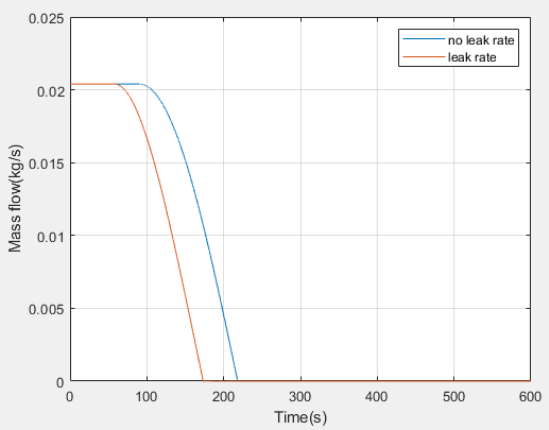

Figure 67: Mass flow ratio calculations for the large breach hole

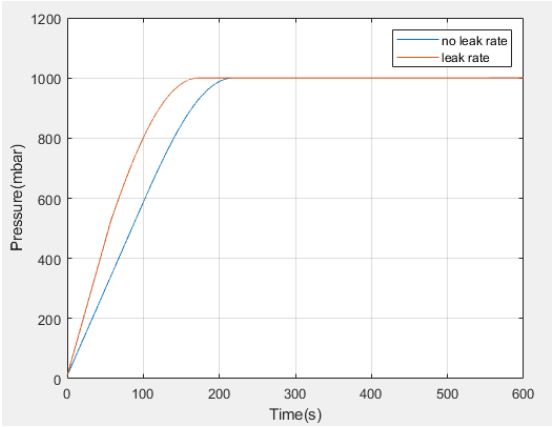

Figure 68: Pressure calculations for the large breach hole

To determine the accuracy of the experiment time estimates and the assumed discharge coefficient of 1.0, the mass flow rate calculations as explained in section 5.4.1 are expanded and evaluated in this section. In figures 67 and 68 the expected mass flow rate and pressure from section 5.4.1 are plotted including the measured leak rate for the large, 20.96 mm diameter breach hole. The leak rate was obtained from the test result by measuring the pressure difference over a period of time before the breach hole was opened, in which the pressures are obtained from the pressure meters linked to the labview program. The pressure difference measured for the large breach hole is $1052 - 1028 = 24Pa$ and the time between the measurements is 2.5 s, resulting in a pressure change due to leakage of 9.6 Pa/s. It is implemented in the plots by assuming the leak rate constant when choked flow conditions were met, however the leak rate is assumed to scale with the outside to inside pressure ratio when the flow is not choked:

$$L_i = L_{i-1} \text{ (if choked)} \tag{45}$$

$$L_i = L_{i-1}(1 - \frac{p_2}{p_1}) \text{ (if not choked)} \tag{46}$$

The mass flow rate and pressure are calculated using equations 41 and 42 from section 5.4.1 in a loop in which 20000 time steps are taken and the leak rate L_i is added in each time step. This way dependency of the leak rate on the pressure ratio is taken into account on each step and the leak rate is recalculated in the loop. The leak rate is assumed to include other components than the breach hole itself: if only the breach hole was assumed to contribute to the leak rate, the leak rate would be included in the choked mass flow rate through the breach hole. The leak sources are thus assumed to include the other(closed) breach hole, the covered tube end and the connection with the vacuum tank. While this will in practice not be completely accurate, measuring the leak rate through the

active breach hole itself was not feasible. The leak rate has a significant effect on the experiment time.

The calculated pressures values are plotted against the values of figure 62 in figure 69. The calculated pressure values reach the ambient pressure outside the tube slightly faster compared to the measured pressure values. This could indicate the airflow through the breach hole did not obtain the theoretical mass flow associated with the breach hole size. Furthermore, the airflow could be disturbed by the breach hole opening mechanism, the pneumatic handle, thus not allowing the theoretical mass flow rate. Assuming a coefficient of discharge of 1.0, as used in equation 42, can also be questioned based on this data, since this assumes no disturbance to the mass flow rate from breach hole shape and quality.

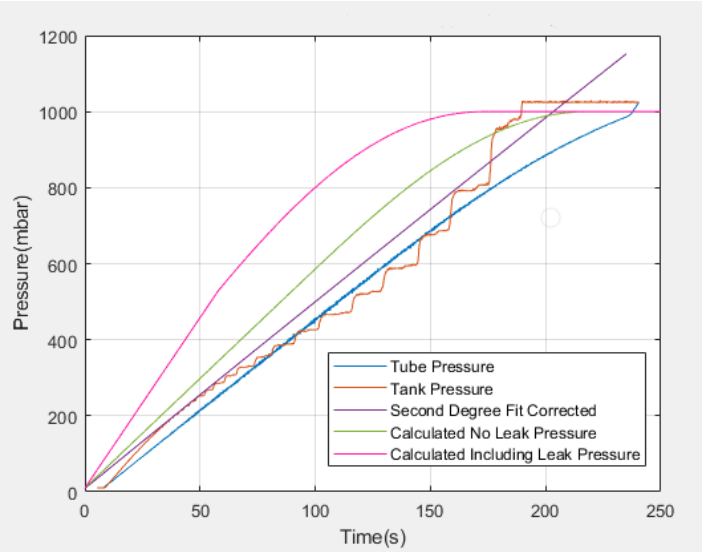

Figure 69: Calculated, measured and correlation pressures for the larger, 20.96 *mm* diameter breach hole test

To determine if a lower coefficient of discharge would be provide a result better matching the measured pressure data, calculations were performed using a coefficient of discharge of 0.7, with the results shown in figure 70. As was explained in section 2.4, the coefficient of discharge is related to the roughness of the breach hole and the Reynolds number through the breach hole. A lower value of the coefficient of discharge would therefore be caused by these factors, which for the test setup could be caused by the interference of the pneumatic handle used to open the breach hole.

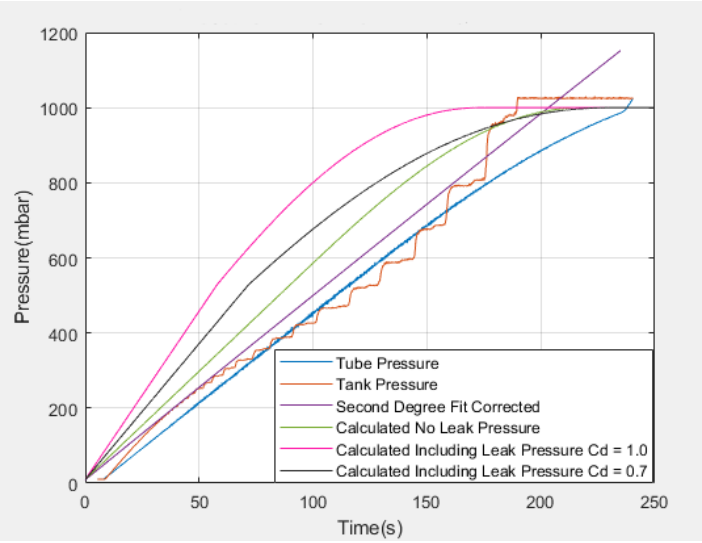

Figure 70: Calculated, measured and correlation pressures for the larger, 20.96 *mm* diameter breach hole test, including calculations for a coefficient of discharge of 0.7

While the lower value for the coefficient of discharge accurately predicts the total experiment time duration as performed during the tests, it overestimates the pressure rise during the first half of the experiment. This could indicate that in the experiments the mass flow rate was not as high as expected from the breach hole size, which can be explained by the presence of the pneumatic handle used to start the experiment. The effective breach hole size for the sake of mass flow rate prediction is therefore most likely less than 20.96 *mm* diameter. The coefficient of discharge of 0.7 nevertheless provides a better estimate while also being within literature values of $0.6 - 1.0$ [2].

7.2.6 Breach hole size analysis

To determine the effects of the breach hole size, the results for the smaller breach hole with a diameter size of 13.16 *mm* are discussed in this section. The first and last background pattern images of the smaller breach hole test are shown in figures 71 and 72. The images were taken 5 minutes and 43 seconds apart. The first image was taken before the breach hole was opened at a pressure of 9.5 *mbar* and the second image at the end of the experiment at an ambient pressure of 1025 *mbar*.

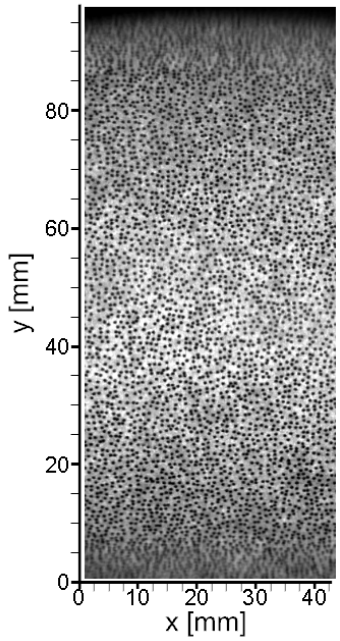

Figure 71: Background pattern of the first image using the smaller, 13.16 *mm* diameter breach hole

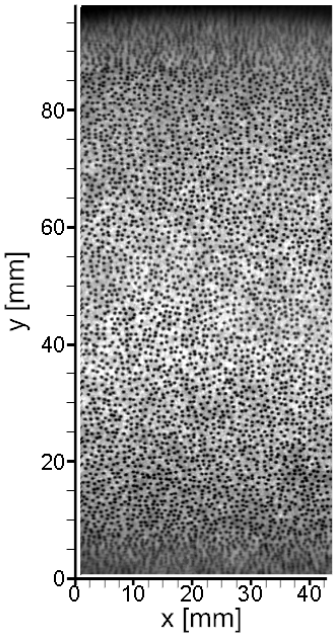

Figure 72: Background pattern of the last image using the smaller, 13.16 *mm* diameter breach hole

Similar to the results for the larger breach hole, the total displacement values of the correlation between the first and last image are shown in figure 73.

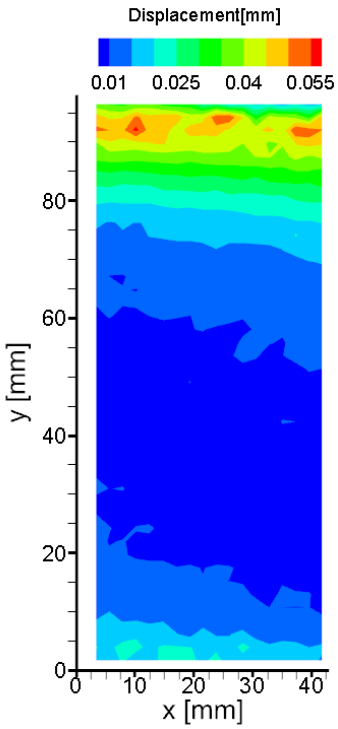

Figure 73: Correlation of the first and last background pattern images of the smaller, 13.16 *mm* diameter breach hole test

The pressures during the experiment were measured and are shown in figure 74.

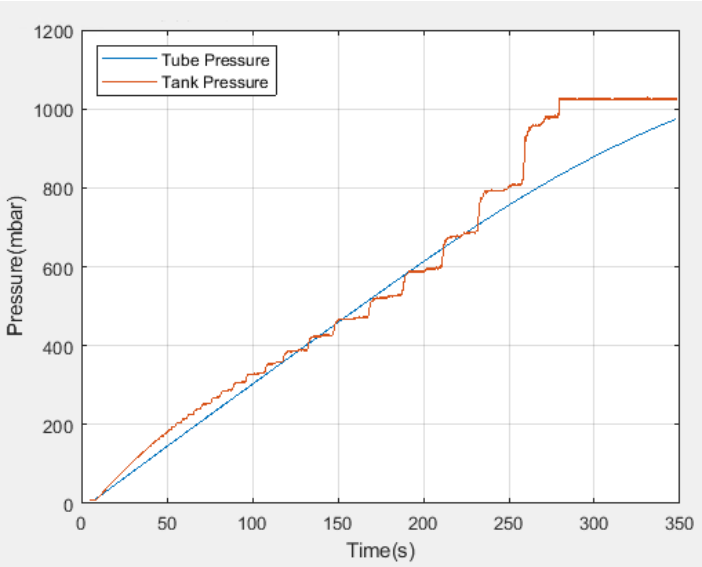

Figure 74: Pressures as measured by the pressure meter in the tube and in the vacuum tank for the smaller, 13.16 *mm* diameter breach hole test

The tube pressure in figure 74 at the end of the experiment does not equal the tank pressure. This is due to the way the test was stopped: the tank pressure was used as an indicator to check if the ambient pressure was reached. Furthermore, the air flowing into the tube makes a high pitched noise. The test was stopped when both the noise had subsided and the tank pressure meter showed ambient pressure. Despite these measures taken, the test was stopped just before the pressure meter in the tube reached ambient pressure. This could indicate that a delay exists between the tube pressure and the pressure meter registering the corresponding tube pressure: while the audible sound of air flowing into the tube was subsided, the pressure meter in the tube did not relay ambient pressure.

Similarly to the method applied for larger breach hole test, the pressures obtained from the mean displacements as a result of image correlations are plotted in figure 75.

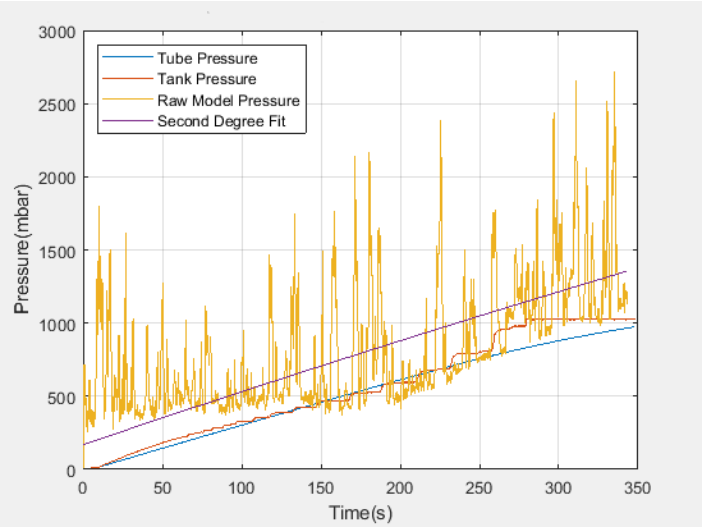

Figure 75: Pressures as measured by the pressure meter in the tube and in the vacuum tank for the smaller, 13.16 *mm* diameter breach hole test combined with mean displacement correlation using the Snell's law model and a second degree fit of the Snell's law model data

The pressure jumps are present for the smaller breach hole test as well, although more prevalent near the end of the test compared to the larger breach hole test. The pressure before the breach hole is opened is expected to be similar to the tank and tube pressure at 10 *mbar*, but instead the pressure values remain between 150 *mbar* and 800 *mbar*.

Similarly to the larger breach hole test, the pressures obtained from subtracting the displacements of the second image correlation from displacement of subsequent images are plotted in figure 76.

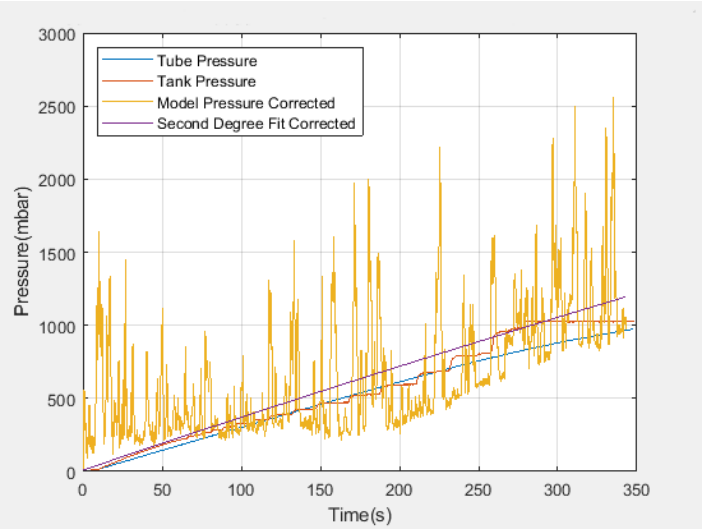

Figure 76: Pressures as measured by the pressure meter in the tube and in the vacuum tank for the smaller, 13.16 *mm* diameter breach hole test combined with corrected mean displacement correlation using the Snell's law model and a corrected second degree fit of the Snell's law model data

The corrected second degree fit has a slightly higher slope compared to the tank and tube pressure and ends higher at a value of 1194 *mbar*.

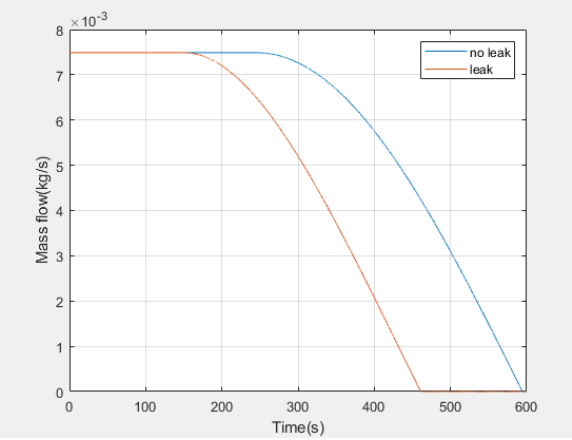

Figure 77: Mass flow ratio calculations for the smaller, 13.16 *mm* diameter breach hole

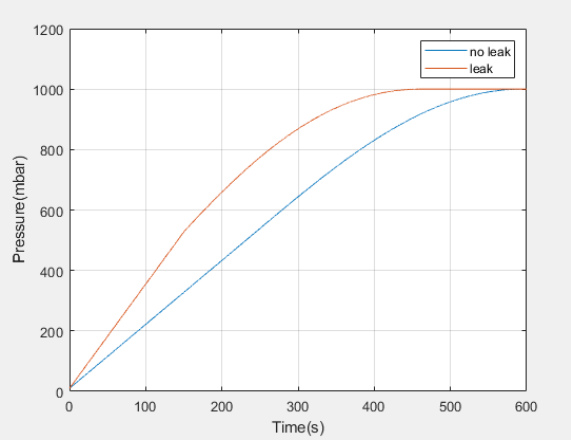

Figure 78: Pressure calculations for the smaller, 13.16 *mm* diameter breach hole

In figures 77 and 78 the expected mass flow rate and pressure from section 5.4.1 are plotted including the measured leak rate. The leak rate has a significant effect on the experiment time, however

similar assumptions as stated for the large breach hole calculations are used. The pressure difference measured for the small breach hole is $978 - 968 = 10\ Pa$ and the time between the measurements is 2.5 s, resulting in a leakage of 4.0 Pa/s. This is a much lower leak rate compared to the leak rate of the large breach hole, which has a leak rate of 9.6 Pa/s. Therefor, it is likely that the leak rate is dictated by the opening device and its connection to the breach hole: during the experiment, the other breach hole is sealed off using a plug while the breach hole relevant for the performed experiment has the opening device attached to it.

The calculated pressures values are plotted against the values of figure 76 in figure 79. The calculated pressures containing the leak correction are a better fit to the pressure measurements from the test than the calculated pressures without the leak correction. Furthermore, while the calculated values overestimate the experiment time, it does accurately predict the pressure rise during the first half of the experiment. Similarly to the larger breach hole mass flow rate analysis, the pressures from the measurement in the experiments rise at a rate that does not decrease as much over time as the calculated values do. For this breach hole size however, the coefficient of discharge of 1.0 does seem to be the best value, since decreasing this value would increase the calculated experiment time.

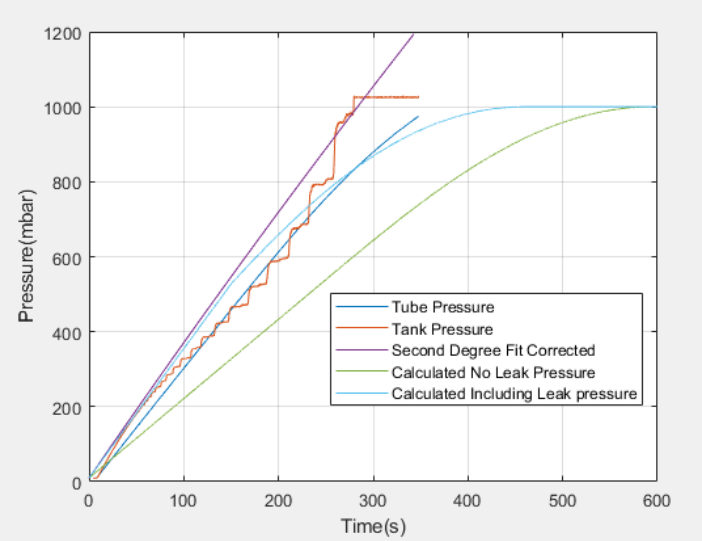

Figure 79: Calculated, measured and correlation pressures for the smaller, 13.16 mm diameter breach hole test

From both the larger and smaller breach hole tests several observations can be made:

- The pressures corresponding to the displacements obtained from correlating background oriented schlieren images have many jumps over time. One reason for this could be the position of the lowest displacement in the images, as was determined from figure 59. Since the Snell's law model expects displacements to increase the further the position is away from the center of the image, any images that do not adhere to this condition will correspond to pressure values that are different compared to images that do adhere to the condition. An attempt to mitigate this

by averaging displacements in y-direction over the image width did not remove then jumps, but did lower the pressure values by 20 $mbar$ on average.

- Both tests appear to have a displacement floor that can be measured: a minimum correlation displacement exists below which no exact values are measured. The pressures corresponding to the displacement before the breach holes are opened are higher than the expected value of $10mbar$. The corrections as performed and shown in figures 62 and 76 are attempts to determine this, however the final pressure value of both second degree fits are still higher compared to the tube and tank pressure values. Furthermore, due to the amount of pressure jumps across the full time span of both tests, the error between specific pressure point and the second degree fit for both tests is significant.

- The pressure rise over time is higher for the larger breach hole test compared to the smaller breach hole test. This is expected due to the increase in area in which air can flow into the tube. Both test results contain the pressure jumps across the entire experiment time, thus this present regardless of breach hole size.

- The background pattern has a speckle density of one speckle every 1.05 mm, as is determined from the calibration images taken using measurement paper. The speckle density is required to be high enough such that local pixel displacements can be registered based on the software correlation window size. For the image resolutions as outlined in section 6.3, this results in 0.072 speckles per pixel. A single pass correlation with a window size of 32×32 is used, thus each window is expected to contain approximately 5 speckles. Since correlation images are able to distinguish local displacements and the speckle density is higher than the required 0.037 speckles per pixel, this speckle density is deemed satisfactory. Furthermore, for this experiment each millimeter equals 14.2 pixels in the images, thus the window size is $2.25mm \times 2.25mm$.

7.3 Test 2: Shockwave detection test results

In this section the results of the shockwave detection test as described in section 6.3.2 are discussed. The shockwave detection test focuses on finding the exact moment and effect of the presumed shockwave in the tube. To find the moment at which the shockwave passes the camera, the image acquisition speed was set to 7500 hz to capture a shockwave passing through the tube, as explained in section 5.4.2.

The pressures during the larger breach hole experiment were measured and are shown in figure 80.

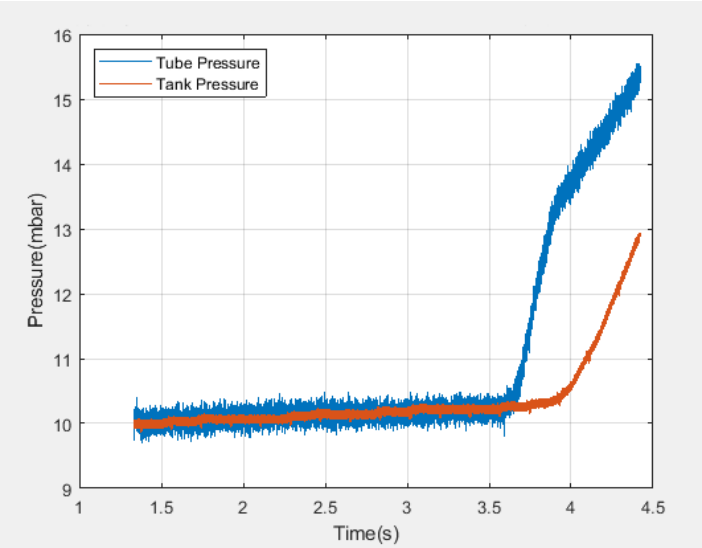

Figure 80: Pressures as measured by the pressure meter in the tube and in the vacuum tank for the larger, 20.96 *mm* diameter breach hole shockwave detection test

The initial pressure is 10.0 *mbar* before the breach hole is opened. The tube pressure rises quickly at 3.6 *s* to a value of 13.4 *mbar*, after which the pressure rise slows down. While the pressure rise indicates the opening of the breach hole and air flowing into the tube, it does not directly indicate the properties and presence of a shockwave. For a shockwave, a sharp instantaneous increase in pressure is expected before reaching an equilibrium state. For air flowing into a tube, this state means a gradual increase in pressure.

To determine the exact location of a possible shockwave, a correlation between each subsequent image is performed. This way, a sudden change in pixel displacement could indicate a change in pressures resulting from a shockwave. Since the location of the shockwave in the image itself is unknown, the average displacement is used while neglecting zero values on the image boundaries. The zero values occur on the border of the image, which is the result of the correlation method. This results of the image correlation is shown in figure 81.

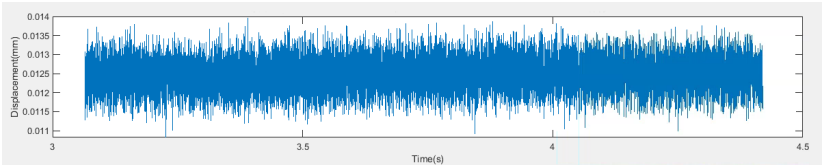

Figure 81: Pixel displacement correlation between subsequent images for the larger, 20.96 *mm* diameter breach hole shockwave detection test

The subsequent image correlation shows no significant increase in average pixel displacement at 3.6*s*, the time of initial pressure increase. After identifying the images at this timestamp individually,

no significant change in pixel displacements was observed. Thus from this analysis the presence and location of a shockwave cannot be determined.

The measured pressures from the pressure meters during the smaller breach hole experiment are shown in figure 82.

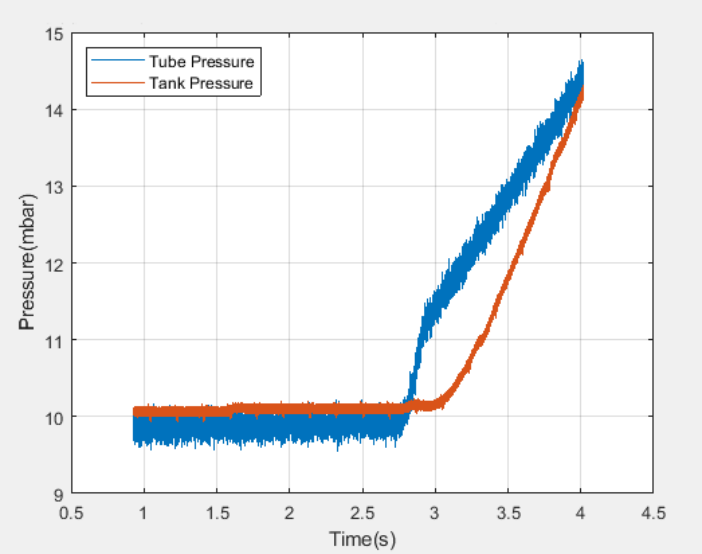

Figure 82: Pressures as measured by the pressure meter in the tube and in the vacuum tank for the smaller, 13.16 *mm* diameter breach hole shockwave detection test

The initial pressure is 10 *mbar* before the breach hole is opened. The tube pressure rises quickly at 2.8 *s* to a value of 11.4 *mbar*, after which the pressure rise slows down. Similarly to the large breach hole experiment, the opening of the breach hole and the subsequent air flowing into the tube is observed from the pressure meters, however a clear indication of shockwaves is not found after performing a pixel displacement correlation from subsequent images as was done for the large breach hole experiment.

A significant difference exists for the start of pressure increasing between the pressure meters in the tube and the tank. The tube pressure rises before the tank pressure does. This is consistent for both breach hole sizes. Due to the consistency across breach hole sizes and it appearing within the first three seconds of test one, the reason for the difference in pressure meters appears to be a structural one: the tube pressure meter is closer to the breach hole then the tank pressure meter, thus the pressure rise would have been picked up by the tube pressure meter earlier. Due to the jumps in the tank pressure meter as mentioned in the full pressure range test results however, the expected delay between the pressure meters is difficult to determine.

To summarize, from both the larger and smaller breach hole tests several observations can be made for the shockwave detection test:

- The tube and tank pressure meters do not increase in pressure at the same time. While this can

be explained by their location in the test setup, the tank pressure meter appears to have a delay between the pressure indicated on the display of the vacuum tank and the value transmitted to the labview program.

- By using a correlation of subsequent images and using the average displacement across images an attempt was made to identify the presence and location of a shockwave originating from the breach hole. The results from the experiment could not confirm the presence and location of a shockwave and it could not be determined whether this is due to no shockwave existing in the test section or the BOS images not being able to detect shockwaves responses.

7.4 Test 3: Hyperloop pod test results

In this section the results of the Hyperloop pod test as described in section 6.3.3 are discussed. The test includes a scaled Hyperloop pod attached to the end of the tube by a cord. After the test was started, the cord moved around in the tube. The cord moved up and down about 2 *cm* from the bottom of the tube. While the cord was attached as tightly as possible, this still occured. While this could have an effect on the results, the cord itself is not visible on the images and the consequence of the cord moving around is difficult to accurately determine, thus this is viewed as a possible error source.

The pressures during the larger breach hole experiment were measured and are shown in figure 83.

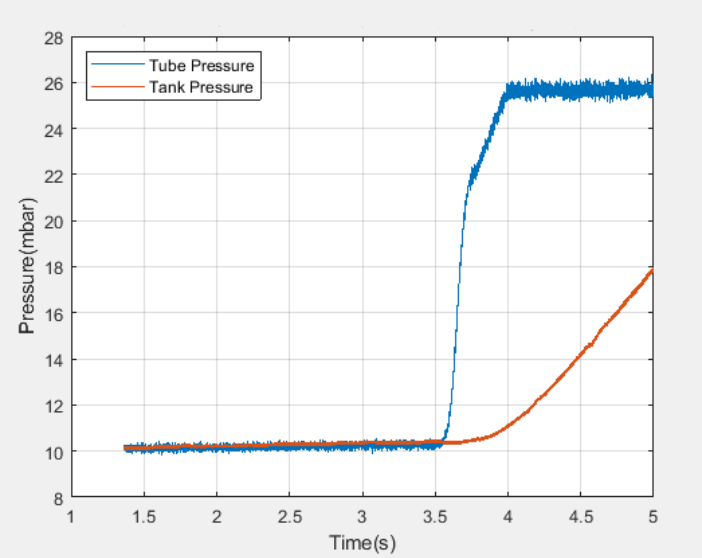

Figure 83: Pressures as measured by the pressure meter in the tube and in the vacuum tank for the larger, 20.96 *mm* diameter breach hole pod test

The initial pressure is 10.2 *mbar* before the breach hole is opened. The tube pressure rises quickly at 3.6 *s* to a value of 22 *mbar*, after which the pressure continues to rise to a value of 25.8 *mbar* before slowly rising until the end of the test. When comparing this result to the experiment of the

shockwave detection test, the initial pressure rise of the tube pressure meter is much higher. The tank pressure however shows similar values between bots test results. The sudden change in slope of the tube pressure at a time of 4 s was not present in the shockwave detection test. A possible reason for this is that the Hyperloop pod test continued longer after the breach hole was opened compared to the shockwave detection test. Another possibility is the presence of the Hyperloop pod in the tube causing the increase in pressure. The tube pressure meter however was placed upstream of the Hyperloop pod, thus the effect is not likely to be a result of air passing over the pod.

The pressures during the smaller breach hole experiment were measured and are shown in figure 84.

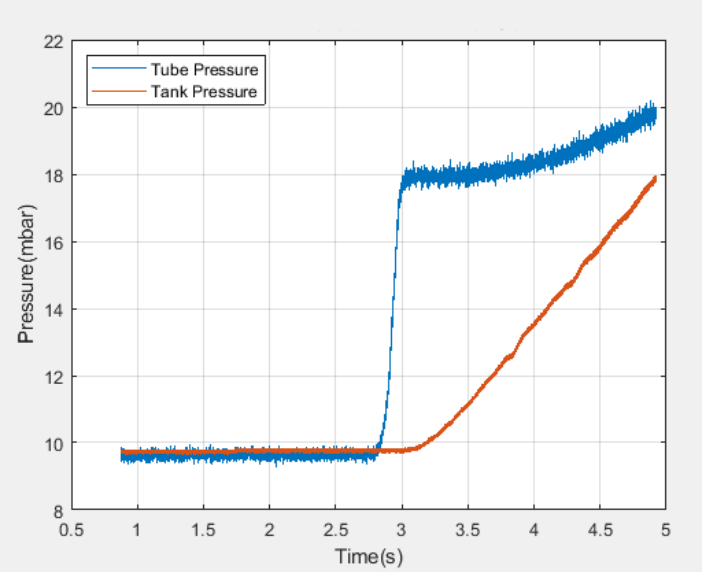

Figure 84: Pressures as measured by the pressure meter in the tube and in the vacuum tank for the smaller, 13.16 mm diameter breach hole pod test

The results show similar tendencies to the larger breach hole test. The values of the tube pressure are higher compared to the shockwave detection test, while the tank pressure shows similar values. Compared to the larger breach hole pod test however, the tube pressure does start increasing more towards the end of the test. While not conclusive, this could indicate the presence of a shockwave due to the discontinuity of the breach hole opening. Similar to the shockwave detection test however, the presence of a shockwave could not be found on the pixel displacement correlation images. To demonstrate this while showing the pixel displacements around the pod, a pixel displacement image is shown in figure 85 just after the breach hole is opened. The lowest pixel displacement are at the leading edge of the Hyperloop pod while the highest pixel displacement are at the very top of the image. The correlation was done using a mask due to the presence of the pod, shown by the grey area in the image: without the masking function applied on the pod area, very high displacements were found on the pod itself. The reason for this is that the pod itself was not covered in the background pattern, thus the correlation software did not have clear references to process pixel displacement.

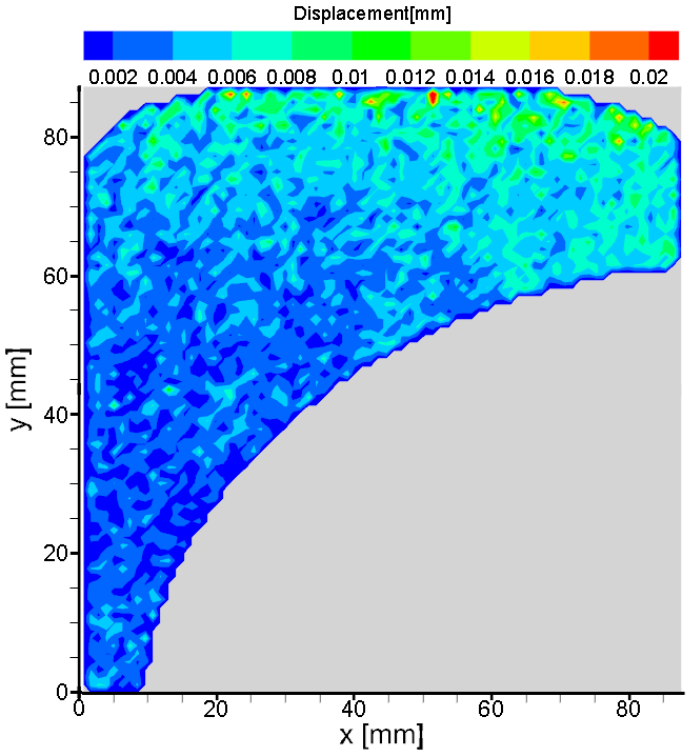

Figure 85: Displacements around the Hyperloop pod after the breach hole is opened for the smaller, 13.16 *mm* diameter breach hole pod test

The pixel displacements shown in figure 85 follow the expected pattern: the highest displacements are the furthest away from the center and the lowest displacements are the closest to the center of the image. This pattern was established from the Snell's law model as described in section 5.1, where due to the curvature of the tube the light rays passing through the tube will displace depending on their incidence angle into the tube.

However, since the presence and location of shockwaves could not be confirmed in this test, determining the way the Hyperloop pod interacts with shockwaves through the tube is not possible from this data.

To summarize, several observations can be made for the Hyperloop pod test:

- By applying a masking function over the Hyperloop pod, cross correlation was performed providing images in which the pixel displacements around a Hyperloop pod are visualized.
- By using a correlation of subsequent images and using the average displacement across images an attempt was made to identify the presence and location of a shockwave originating from the breach hole. The results from the experiment could not confirm the presence and location of a

shockwave and it could not be determined whether this is due to no shockwave existing in the test section or the BOS images not being able to detect shockwaves responses.

- Since the presence of a shockwave could not be confirmed, the interactions between Hyperloop pod and shockwave could not be investigated.

8 Conclusions

With Hyperloop research developing and interest increasing, the Hyperloop breach failure scenario is investigated in this research. Hyperloop operates in a high speed, low density environment, but remains in continuum flow conditions with an expected Knudsen number of $1.33 \cdot 10^{-4}$. For Hyperloop operation the Kantrowitz limit, the limit on blockage ratio in a Hyperloop, plays an important role in preventing a drag increase due to the presence of a Hyperloop pod. Based on an investigation by Wong[34], a blockage ratio for the scaled Hyperloop pod in this research is chosen to be 0.625.

The research objective is to analyse the aerodynamic response of Hyperloop breach. The research objective is realized by using a scaled physical test setup. The test setup consists of a PMMA tube connected to a vacuum tank. Two breach holes with a diameter of 13.16 *mm* and 20.96 *mm* were installed in the tube, such that the tests could be performed for different breach hole sizes. Pneumatic handles are fitted to the breach holes, ensuring a tight connection and a method of opening and closing the breach holes. An sCMOS camera and a background speckle pattern are placed on opposite sides of the tube at the test section, allowing Background oriented schlieren to be used as a non intrusive method of measuring pressure changes inside the test setup. A pressure meter is installed in the tube, to allow for reference pressure measurements. The pressure meter, the camera and the pressure meter of the vacuum tank are connected to a computer with correlation software, allowing for data storage in a similar timeline for all connected devices. Furthermore, a ray tracing model based on Snell's law is developed to relate physical test results to pressure values. In this model light beams are simulated that move from the background pattern through the test section and the Hyperloop tube for different pressures inside the tube. This results in a relation between location of the light beam, displacement due to a change in refractive index, as a result of a change of inside pressure with respect to the reference pressure, and the pressure inside the tube.

Testing was done at the high speed lab of the Delft university of Technology. An initial BOS feasibility test was performed to determine the effectiveness of the test setup and BOS as a measurement technique. For this test only the tube, camera and background pattern were used and density changes in the tube were emulated using a targeted heating device. The BOS feasibility test found the effectiveness of background oriented schlieren as a measurement technique to be sufficient to perform further testing, since pixel displacements could be observed from correlation images. From experiments done by Raffel[27] and Cozzi[13] on background patterns in BOS a suitable particles per pixel value was found to be 0.037 particles per pixel, which for the purpose of this research is viewed as the minimum required value for background patterns. The background pattern used in testing has a particles per pixel value of 0.072, thus it exceeds the minimum required value. The correlation software settings for this test include a single pass vector calculation, while a pass window size of 64×64 is used. A larger window size made it difficult to distinguish local displacements, while course multi-pass operations did not improve the ability to distinguish local displacements. For following main tests the pass window size is decreased to 32×32 to ensure the ability to record accurate local displacements. Furthermore, the pass window overlap was set to 0%, which means there is no overlap between each window. These conclusions from this initial feasibility test are used to perform the three main tests, in which the Hyperloop tube is connected to the vacuum tank.

The three main tests were performed using the full test setup. Each test is performed using the two different sizes for the breach hole mentioned.

The first test is a 5 frames per second test in which the whole pressure range from a closed tube, to an opened breach hole tube, to ambient pressure is registered. An image resolution of 624×1412 pixels is used, which allows for an experiment duration of at least 600 s.
The second test is a 7500 frames per second test to visualise and detect shockwave effects as a result of the pressure difference. The expected maximum shockwave speed was calculated to be 803 $\frac{m}{s}$ from quasi-1D calculations, therefore the width of the image has to be big enough to ensure at least one shockwave is captured. A resolution of 960×568 was used: the height of the image is reduced in favor of width to increase the likeliness of capturing a shockwave on an image, while being restricted by the internal camera memory.
The third test is a Hyperloop pod test in which the presence of a scaled Hyperloop pod in the tube is investigated. The pod is placed such that background pattern is visible around the front and top part of the Hyperloop pod. The pod was kept in place using magnets attached to both the underside of the pod and magnets outside the tube. The test is done at 2000 frames per second. This is a lower frames per second value compared to the second test, since a larger area is required for viewing the entire front end of the tube, resulting in a resolution of 1248×1252.

The test results were documented, stored and processed by having all measurements adjusted to the same timeline of the experiment. The test results were analysed using the Snell's law ray tracing model, in which pixel displacements were correlated to pressure values.

To analyze the results of the first test, correlation operations were performed on the images using Davis. By taking the mean value of center correlation windows, a pressure value inside the tube was assigned based on the Snell's law model. From this pressure graphs were created spanning the entire experiment time. The pressure graphs showed many pressure jumps across the test time. This is most likely attributed to error sources related to vibrations caused by the vacuum tank and air flowing into the tube through the breach hole. Error sources cause a pixel displacement that can be higher then the smallest displacement measured in the test, thus the conversion from pixel displacement to its associated pressure is affected by these error sources. Furthermore, several images did not have the lowest displacement position in the center, which is the position where it is expected. Since the Snell's Law model expects displacements to increase the further the position is away from the center of the image, any images that do not adhere to this condition will correspond to pressure values that are different compared to images that do adhere to the condition. The larger breach hole reaches ambient pressure faster than the smaller breach hole due to a higher mass flow rate of air entering the tube. While several data processing operations were performed to produce results that have the pressure jumps mitigated, such as averaging the image displacements over the width of the image and taken the displacement in only the y-direction, it only reduced the amplitude of the jumps rather than provide smooth pressure data graphs.
To obtain a smooth pressure distribution across the entire test duration, converted pressure values require a second degree fit while also applying a correction, shifting the graph downward to account for the minimal measurable displacement. The downward shift is obtained by subtracting the mean displacement in the second cross correlation image from each subsequent cross correlation image in the test data set, which is equal to 0.0023 mm for test with breach hole diameter of 20.96 mm. This way, the converted pressure of the second cross correlation image is equal to the expected inside pressure of 10 $mbar$. By performing this operation, a graph is made that corresponds well to pressure readings from the pressure meters of the performed test. While the second degree fit corresponds well to measurements from the pressure meter, the jumps in the pressure graphs remain an error source.

From the second test the presence of shockwaves could not be confirmed from the test results. A correlation operation was performed between subsequent image frames in an attempt to find pixel displacements indicating shockwave effects, however no clear pixel displacement indicating such effects were obtained from this correlation. While the image capturing frequency and image width are theoretically sufficient to capture a shockwave scenario based on the calculated maximum shockwave speed of 803 $\frac{m}{s}$, which assumes quasi-1D conditions, no clear indications of shockwaves were found in the cross correlation images.

For the third test the presence of shockwaves could not be confirmed from the test results, however the pressure distribution around the Hyperloop pod could be investigated by applying a masking function. Since the presence of a shockwave could not be confirmed, the interactions between Hyperloop pod and shockwave could not be investigated further.

From the experiments performed the use of BOS for Hyperloop breach research seems feasible, however the results are sensitive to error sources. To determine accurate values for the coefficient of discharge and breach hole effects, accurate values of the leak rate and breach hole roughness are required. By comparing mass flow rate and leak rate estimations with pressure measurements done during the experiment, a coefficient of discharge of 0.7 was found for the 20.96 mm diameter breach hole, while a coefficient of discharge of 1.0 was found for the 13.16 mm diameter breach hole. While these values are influenced by error sources, they lie within the $0.6 - 1.0$ literature estimations for these type of holes[2]. While this research provides an overview of the use of BOS for Hyperloop breach, drawing conclusions from the scaled test for full scale Hyperloop breach scenarios is difficult due to the error sources. Furthermore, since shockwaves were not detected on correlation images, its impact on full scale Hyperloop operations can not be concluded from the test results.

9 Discussion and recommendations for future research

While using background oriented schlieren in Hyperloop breach research shows promising signs of predicting the aerodynamic response to the occurrence of a breach, clear limitations to the method have appeared. One of the limitations is that results are influenced by errors, such as measurement uncertainty and imperfections in the test setup. The tank pressure read offs showed jumps rather than a gradual pressure increase and a conclusive reason for this was not found after discussing with faculty personnel and inspection of the vacuum tank display. Furthermore, the jumps were present on all tests, which could indicate a structural issue with the vacuum tank itself or the pressure meter in the vacuum tank. For future research, it is suggested to inspect the vacuum tank for these issues mentioned or use a different pressure meter for vacuum tank.

The minimal measurable displacement for using BOS in the performed experiments is significant: a subtraction of 0.0023 mm from the mean displacements is used, which equals to 200 $mbar$ when converted to pressure values. Since that equals 20% of the total pressure range of the test, this is a large error value. While correcting for this shows results that are in line with pressure meter measurements, mitigating errors in the test setup would provide more confident results. To do this, the error sources have to be individually identified and quantified, which proved difficult in this research. The main error sources are assumed to be vibrations from the vacuum tank, air rushing into the tube and the manual breach hole opening handle, as observed from equipment inspection and experiment observations.

From the experiment the presence of shockwaves could not be confirmed. This could be because either the test setup did not experience any shockwaves or the measurement method was not able to capture the presence of shockwaves. While from a theoretical basis the occurrence of a shockwave in the test section was expected, this is based on assumptions made in the calculations. One of the main reasons the assumptions might not hold can be from the method of starting the experiment: the opening of the breach hole using a pneumatic handle. The predictions for shockwave characteristics assume an instantaneous occurrence of breach, in which the inside and outside pressure calculate the pressure difference over the shockwave. Using a pneumatic handle to manually open the breach hole takes less then a second, however this is far from instantaneous. Furthermore, the pneumatic handle increases the length of the breach hole while maintaining the diameter of the original breach hole. All these factors influence the presence of a shockwave in the physical test setup and are not taken into account in the shockwave prediction model. While different options of opening the breach hole were investigated such as membranes and electronic switches, the use of pneumatic handles allowed for the use of standard sizing already present at the faculty. Furthermore, the testing of different breach starting options was severely limited by COVID-19 quarantine measures across the country, thus the choice was made to continue with readily available options.

To continue research on Hyperloop breach, several improvements to both the test setup and data processing are advised. The current experiments could be performed using either a camera with a higher memory limit or placing the camera further from the tube to have a wider view of the test section. This way the likelihood of capturing a shockwave increases as well as being able to capture the development of the shockwave through the tube. Furthermore, in the current setup one camera is used to record images, thus limiting the images to a 2D plane. If more cameras were used to record multiple angles of the test setup, the 3D density field could be recorded and processed. If done this

way, the local pressures could be obtained without using the Snell's law model, since a 3D density field is available.

To improve the data processing, the Snell's law model used in this research can be expanded by including off center light rays: the current model uses a center set of correlation windows to convert pixel displacements to local pressures. Performing an analysis that has a variable minimal displacement center in the Snell's law model could mitigate errors related to vibrations. This way the model does not require that the lowest pixel displacement is assumed in the center of the image.

It is difficult to determine how well the results of this scaled physical breach test translate to the full size Hyperloop breach failure case, since shockwave effects could not be identified and confirmed from the test results. It is therefore advised to use existing full scale test equipment, such as the Hardt Hyperloop test facility at the green village in Delft, to obtain a better understanding of aerodynamic effects on a full scaled Hyperloop tube.

Finally, while this project has demonstrated a method of analysing the Hyperloop breach scenario in a scaled setup, other options of analysing Hyperloop breach are possible. For future research on this topic, it is advised to use a more controlled testing environment in which error mitigation is less of a concern. A breach hole opening method with more precision and less obstruction, as is the case with a pneumatic handle, is advised. Furthermore, the material aspect of Hyperloop breach can be investigated, in which the breach hole itself can be analysed and a correct value for the coefficient of discharge can be found.

References

[1] Atmospheric Railways. *Journal of the Franklin Institute*, pages 293–295, November 1864. doi: 10.1016/0016-0032(64)90506-X.

[2] Technical Committee ISO/TC 30. *Measurement of fluid flow by means of pressure differential devices inserted in circular cross-section conduits running full - Part 1: General principles and requirements*. British Standards Institution, March 2003.

[3] A. Aerts, C. Chen, D. Nijhof, G. Blokland, H. van Loveren, M. Miedema, and S. Bergkamp. *Hypertube Feasibility Study*. Tata Steel, 2018.

[4] John B. Anders, W. Kyle Anderson, and A. R. Vasudeva Murthy. The use of heavy gas for increased reynolds numbers in transonic wind tunnels. 1998. 20th AIAA Advanced Measurement and Ground Testing Technology Conference; June. 1998; Albuquerque, New Mexico; United States. doi: 10.2514/6.1998-2882.

[5] J. D. Anderson. *Fundamentals of Aerodynamics*. McGraw-Hill Education - Asia, 5th SI edition, 2011.

[6] J. D. Anderson. *Modern Compressible Flow*. McGraw-Hill, 3rd SI edition, 2017.

[7] J.D. Anderson. *Hypersonic and High Temperature Gas Dynamics, Second Edition*. 2006. doi: 10.2514/4.861956.

[8] P. Bakker and B. van Leer. *Lecture notes on Gasdynamics, AE4-140*. TU Delft, 2019.

[9] Yorrick Bauer. Hyperloop tube breach, 2019.

[10] Adel M. Benselama, Mame J.-P. William-Louis, Francois Monnoyer, and Christophe Proust. A numerical study of the evolution of the blast wave shape in tunnels. *Journal of Hazardous Materials*, 181:609–616, 2010.

[11] T. Benson. Mass flow rate, 2014. Accessed 20-06-2019, Available at https://www.grc.nasa.gov/WWW/K-12/rocket/mflchk.html.

[12] G Bönsch and E Potulski. Measurement of the refractive index of air and comparison with modified edlén's formulae. *Metrologia*, 35(2):133–139, April 1998. doi: 10.1088/0026-1394/35/2/8.

[13] F. Cozzi and E. Gottlich. Enhanced background oriented schlieren. *Journal of Physics: Conference Series 1249 012017*, page 23, March 2019. doi: 10.1088/1742-6596/1249/1/012017.

[14] Hassan A. Ghazwani. Preliminary study of optical-flow based background-oriented schlieren measurements, 2016.

[15] T. Gélain, A. Rondeau, S. Peillon, J.C. Sabroux, and F. Gensdarmes. Cfd modelling of the wall friction velocity field in the iter tokamak resulting from airflow during a loss of vacuum accident-consequences for particle resuspension. *Fusion Engineering and Design*, 100:87–99, 2015. doi: 10.1016/j.fusengdes.2015.04.043.

[16] Hardt. Hardt meeting on pod dimensions, 2019. High speed lab, TU Delft.

[17] Hardt. *Hyperloop concept Hardt Hyperloop*. Hardt, 2020. Delft.

[18] Delft Hyperloop. Delft hyperloop i. Accessed 25-06-2019, Available at https://delfthyperloop.nl/en/hyperloop.

[19] Evonik Industries. *Rods and Tubes, Plexiglas GS/XT technical information*. Evonik Performance Materials GmbH, 2015.

[20] A. Kantrowitz and C. Donaldson. *Preliminary Investigation of Supersonic Diffusers*. NASA, 1945.

[21] LaVision. *DaVis 8.1 Software*. LaVision GmbH, 2013.

[22] E. Musk. *Hyperloop Alpha*. SpaceX, 2013.

[23] Jae-Sung Oh, Taehak Kang, Seokgyun Ham, Kwan-Sup Lee, Yong-Jun Jang, Hong-Sun Ryou, and Jaiyoung Ryu. Numerical analysis of aerodynamic characteristics of hyperloop system. *Energies*, 12:518, February 2019. doi: 10.3390/en12030518.

[24] C. Olson, J. Nichols, C. Villarruel, and F. Bucholtz. On the potential use of evolutionary algorithms for electro-optic system design. page 23, March 2011.

[25] Max M.J. Opgenoord and Philip C. Caplan. On the Aerodynamic Design of the Hyperloop Concept. 2017. 35th AIAA Applied Aerodynamics Conference; 5-9 June 2017; Denver, Colorado; United States.

[26] Alan Pope and L. Kennith Goin. *High-Speed Wind Tunnel Testing*. John Wiley and Sons, Inc., 1965.

[27] M. Raffel. Background-oriented schlieren techniques. *Experiments in Fluids*, 56(3):60, March 2015. doi: 10.1007/s00348-015-1927-5.

[28] Bastian E. Rapp. Chapter 9 - fluids. In Bastian E. Rapp, editor, *Microfluidics: Modelling, Mechanics and Mathematics*, Micro and Nano Technologies, pages 243 – 263. Elsevier, Oxford, 2017. doi: 10.1016/B978-1-4557-3141-1.50009-5.

[29] R. Reddy. Flow measuring devices: Types of flow meters and their applications. June 2018. Accessed 02-07-2019, Available at http://www.engineeringenotes.com/fluids/flow-measuring-devices/flow-measuring-devices-types-of-flow-meters-and-their-applications-fluid-mechanics/47247.

[30] B. Sang and T Jeon. Pressure-dependent refractive indices of gases by thz time-domain spectroscopy. *Optical Express*, 24(25):29040–29047, March 2015. doi: 10.1364/OE.24.029040.

[31] René Schödel, Alexander Walkov, Michael Voigt, and Guido Bartl. Measurement of the refractive index of air in a low-pressure regime and the applicability of traditional empirical formulae. *Measurement Science and Technology*, 29(6):064002, April 2018. doi: 10.1088/1361-6501/aab31a.

[32] R. Shankar Subramanian. Reynolds Number, 2014. Available at https://web2.clarkson.edu/projects/subramanian/ch330/notes/Reynolds%20Number.pdf.

[33] J. C.J.H. van den Bosch and R.A.P.M. Weterings. *Methods for the calculation of physical effect due to releases of hazardous materials (liquid and gases) - "Yellow Book"*. The commitee for the prevention of disasters by hazardous materials, 3rd edition 2nd print edition, 2005.

[34] F. T. H. Wong. Aerodynamic Design and Optimization of a Hyperloop Vehicle. Master's thesis, TU Delft, 2018.

[35] Y.P. Zhang, S.S. Li, and M.X. Wang. Main vacuum technical issues of evacuated tube transportation. *Physics Procedia*, 32:743 – 747, 2012. The 18th International Vacuum Congress (IVC-18). doi: 10.1016/j.phpro.2012.03.628.

A Finite Element Analysis

The tube used for testing has to be able to withstand all loads applied. A simple straight tube was used to approximate the physical tube. To be sure the tube holds a pressure difference of approximately 1 bar, a linear buckling analysis was performed in finite element modelling software Abaqus. The results for a 2 m length, 10 cm diameter and 5 mm thick Plexiglas(PMMA) tube are shown in figure 86. The maximum displacement is 0.02 mm and no failure has occurred. The first failure mode is shown in figure 87 with an amplification factor of 20. The failure pressure is indicated by the eigenvalue, which is 10.517 bar for the first mode of failure, thus it will be able to withstand the 1 bar overpressure. This is however a simplified model: no holes have been drilled in the FEM model tube and the end has not been sealed. Furthermore, no reinforcements on the tube are present and the boundary conditions is clamped at one side of the tube.

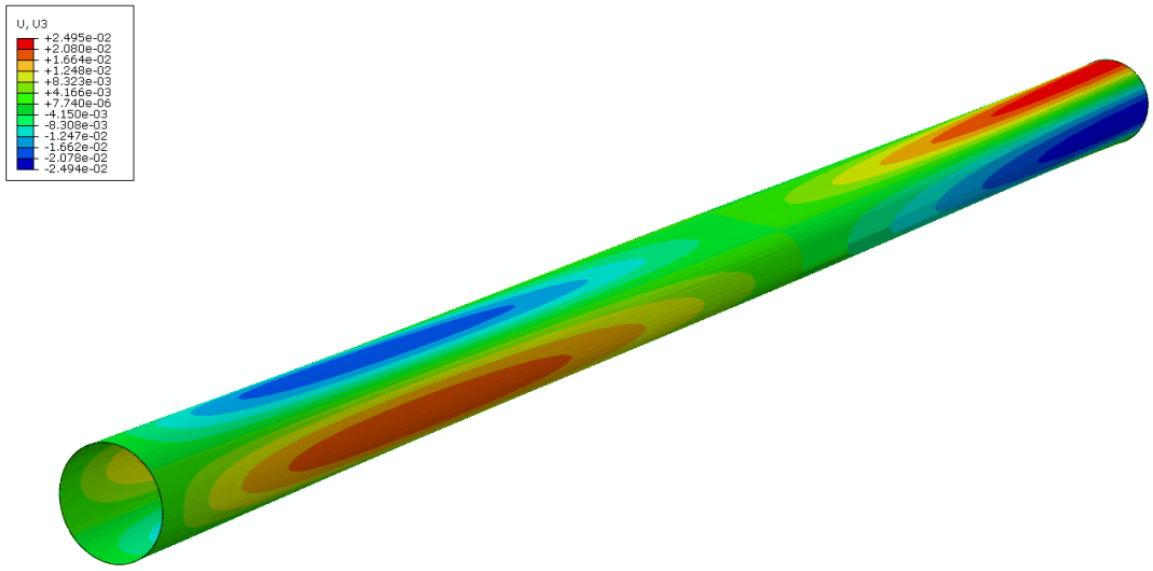

Figure 86: Finite element analysis on a 5 millimeter thick PMMA tube

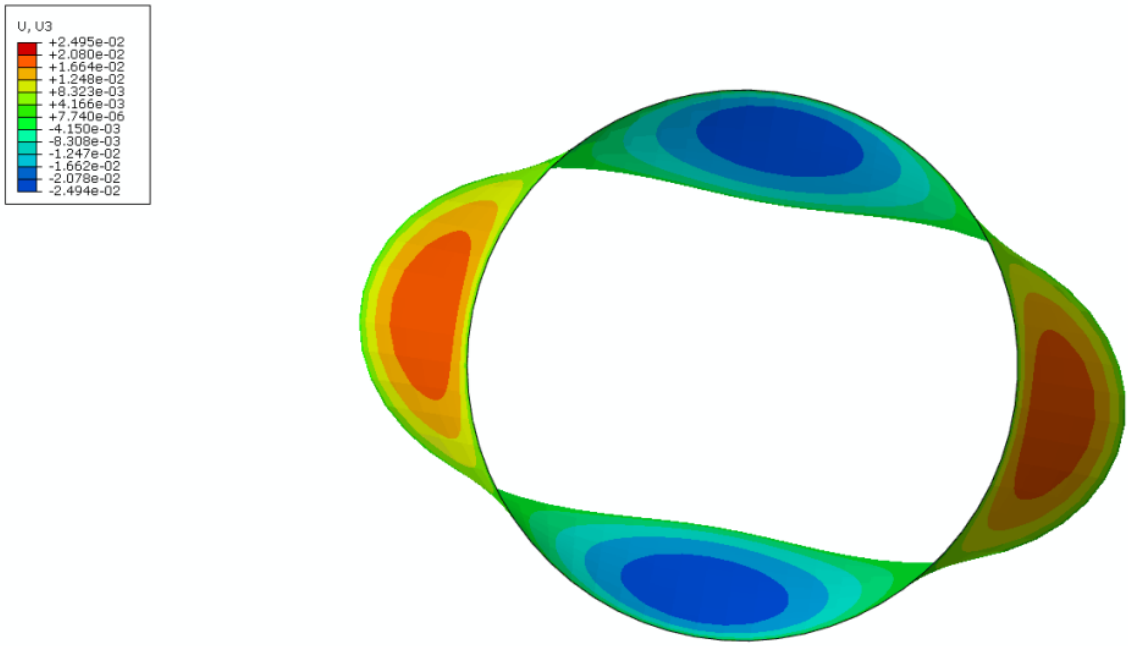

Figure 87: Failure mode of the finite element analysis on a 5 millimeter thick PMMA tube

B Tube Dimensions

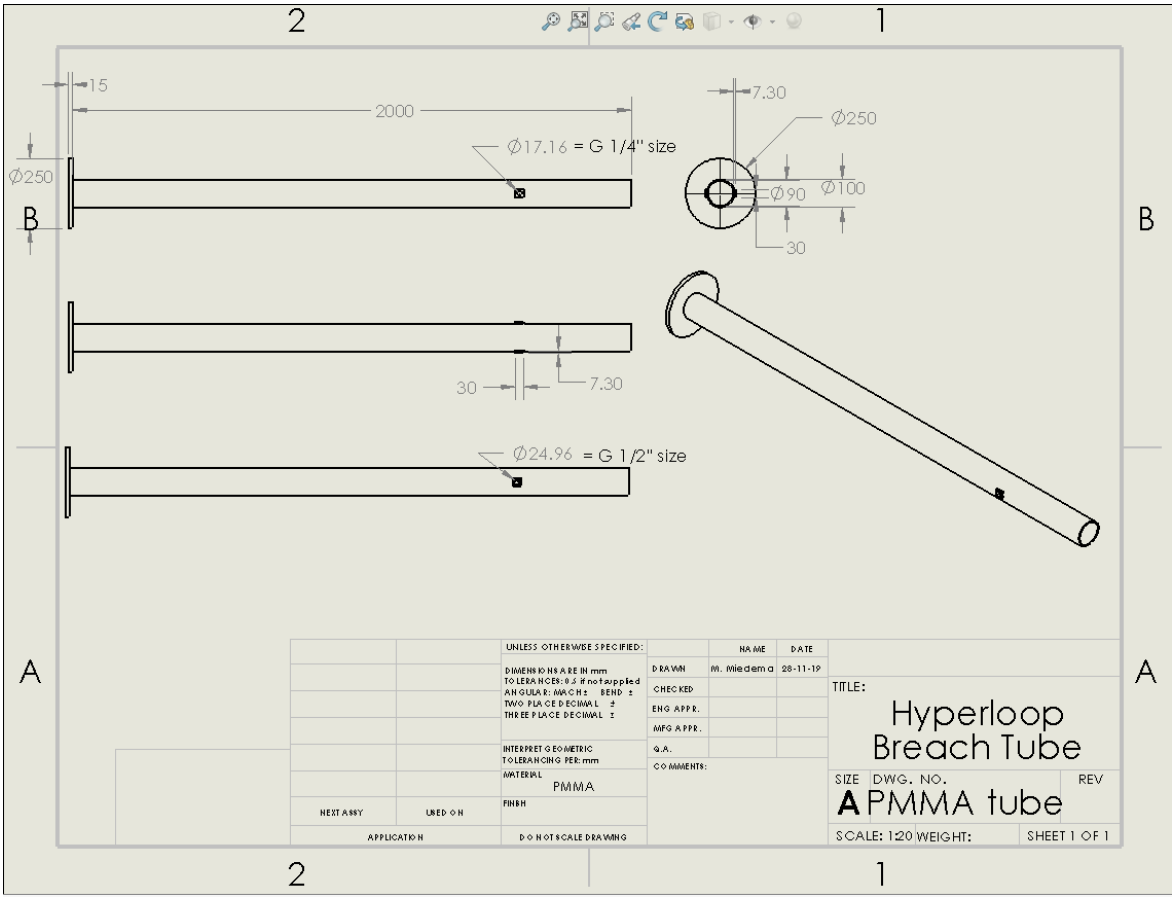

Figure 88: Detailed drawing of the Plexiglas tube used in Hyperloop Breach testing

C Ring Dimensions

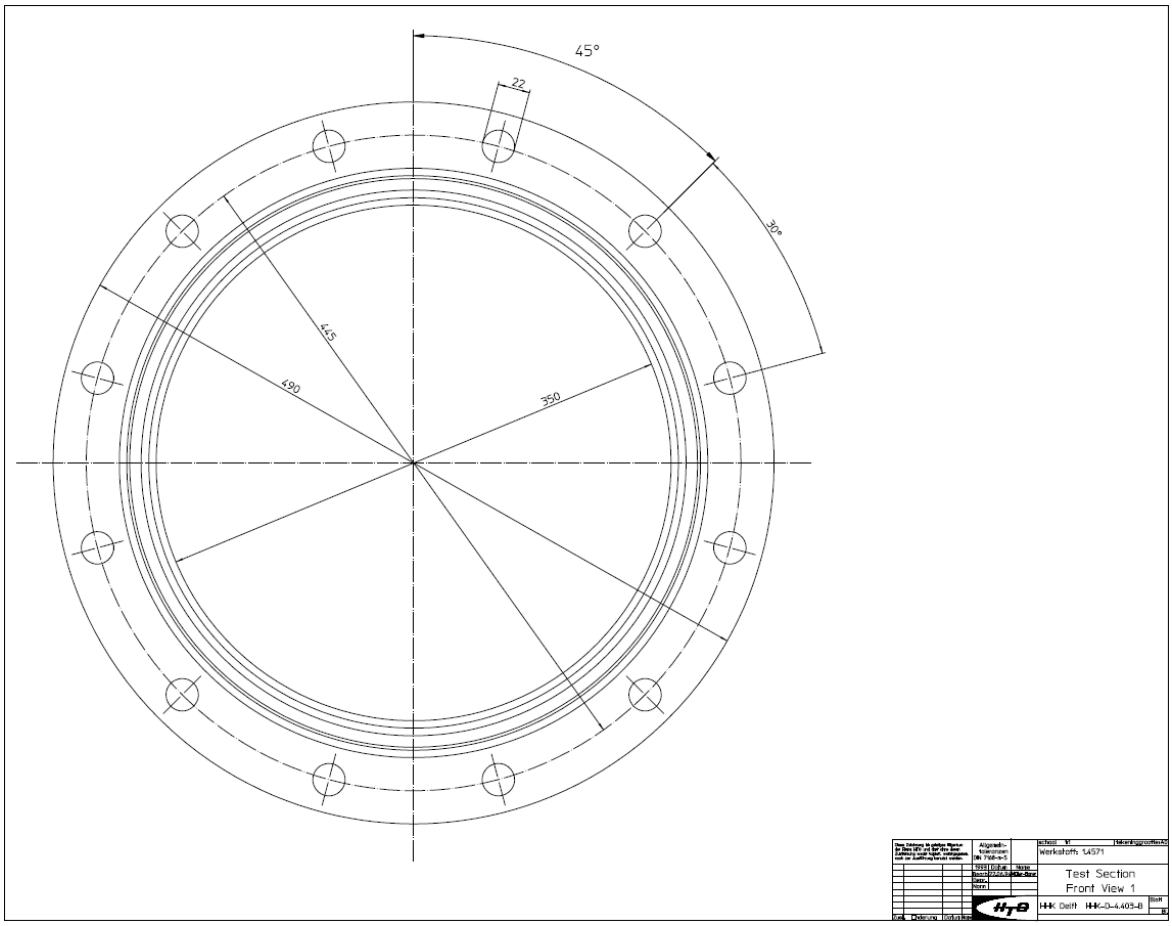

Figure 89: Detailed drawing of the HTFD vacuum chamber ring connection

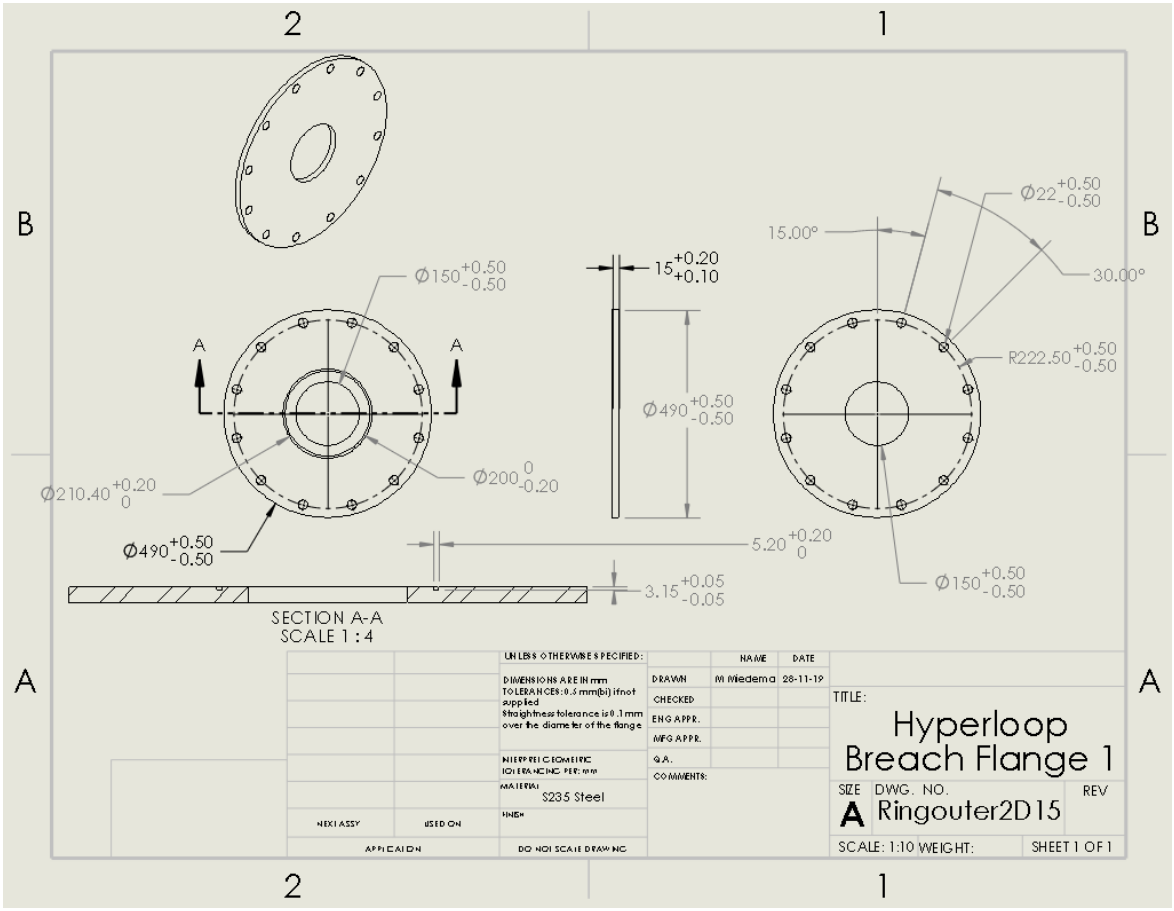

Figure 90: Detailed drawing of the outer connection ring used in Hyperloop Breach testing

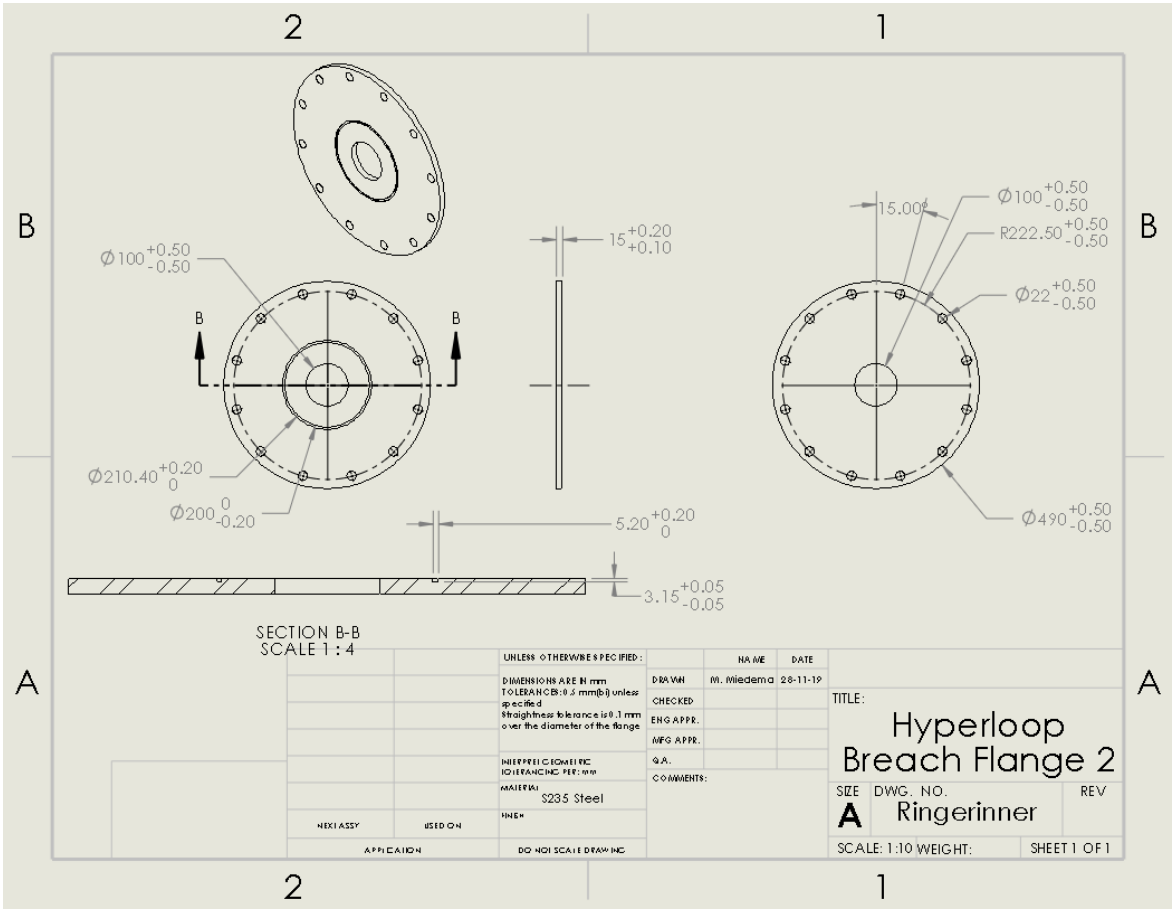

Figure 91: Detailed drawing of the inner connection ring used in Hyperloop Breach testing